THE EXAMINATION OF ASPHALT BINDER MICRORHEOLOGY USING ATOMIC FORCE MICROSCOPY AND THE FINITE ELEMENT METHOD

A Dissertation

by

REZWAN JAHANGIR

Submitted to the Office of Graduate and Professional Studies of
Texas A&M University
in partial fulfillment of the requirements for the degree of

DOCTOR OF PHILOSOPHY

Chair of Committee,	Dallas Little
Committee Members,	Amit Bhasin
	Robert Lytton
	Charles Glover
	Zachary Grasley
Head of Department,	Robin Autenrieth

December 2015

Major Subject: Civil Engineering

ABSTRACT

In order to obtain a better understanding the complex mechanical behavior of asphalt binder, its microstructure must be examined. In addition, the interrelationship between asphalt binder microstructure, damage, and mechanical properties must also be determined. In this work the unique relationship between asphalt binder microstructure and damaging mechanisms is established. Here, the AFM is used to image the microstructure of two different types of asphalt binders. A micrometer driven mechanical device named a "Micro-Loading Frame" is used to obtain AFM images of bitumen surface after subjecting it to high levels of tensile strain. Using image analysis techniques the microstructural changes due to the applied tensile strain is established. Furthermore, using a specific AFM creep indentation protocol the viscoelastic properties of asphalt binder are extracted for each microstructural phase observed. In addition, this concept was applied to rolling thin film oven test (RTFOT) aged and pressure aging vessel (PAV) aged binders. The geometry obtained from AFM imaging combined with the microrheology obtained from AFM creep indentation experiments were used to construct finite element simulations examining local stress distributions. The numerical solutions were compared to experimental observations.

Using AFM imaging technique three unique phases were found within the asphalt binder at the micron length scale i.e. bee, bee casing, and interstitial. All three phases were found to have uniquely different viscoelastic properties. Finite element analysis results showed that heterogeneity within the asphalt binder led to localized stress amplification. Application of high levels of tensile loads resulted in phase separation and cracking referred to as load induced phase separation (LIPS) zones. The occurrence of the LIPS zones were primarily found to be within interstitial regions. Application of tensile strains also resulted in the reduction of the number of bee structures, and also the area occupied by the bee structures. The location of LIPS zones coincided with the location high stress zones determined using the finite ele-

ment simulations suggesting the possibility of phase separation and cracking occurring due to localized high stresses. Application of tensile strains to RTFOT, and RTFOT+PAV aged samples also resulted in the formation of LIPS zones within the interstitial regions. However, an increase in the level of aging the led to a reduction of LIPS zone formations for the same level of applied tensile displacements.

The effect of geometry of asphalt binder microstructure on the mechanical response was determined. An increase in the area fraction of the bee/bee casing phase, a reduction in the distance between adjacent bee/bee casing features led to an increase in the maximum stress magnitudes. An increase in the number of bee/bee casing features led to a reduction in the maximum stress magnitude when the area fraction was kept constant.

DEDICATION

I would like to dedicate this dissertatoin to my wife, Syeda. You have always encouraged me and without your positivity I would have never been able to get this far. I am thankful to you for everthing you have done for me. I also want to dedicate this dissertation to my parents and my sisters who have helped me in every way they could throughout my journey at Texas A&M University.

ACKNOWLEDGEMENTS

I want to thank Dr. Little for giving me the opportunity to work with him and to pull me out of a bad situation during a time of crisis. I will be forever indebted to Dr. Bhasin for guiding me through my PhD and helping me overcome every roadblock that was in the way. If it weren't for you I would still be sitting in the laboratory pondering what I should do next. Thank you for your innovative ideas and helping me find ways to solve problems that weren't readily available. I am especially thankful to Grover Allen for teaching me how to operate the Atomic Force Microscope without destroying it. I want to also thank Dr. Serem at the Materials Characterization Facility for being so selfless with the amount of time he spent to help me understand the AFM.

I want to finish by saying that I am very grateful that I have a wife like Syeda. She helped me get through my PhD and provided me with emotional support whenever I needed it. She took care of me whenever I was ill and always made sure that I stay focused. She always made me look at the positive side of every situation and helped me overcome any negativity. Syeda, thank you for being here and thank you for being my best friend.

I would also like to thank the Federal Highway Administration for funding this research. The National Science Foundation [grant number CMMI-1053925] is also partially responsible for funding this research.

TABLE OF CONTENTS

Page

LIST OF FIGURES

FIGURE Page

LIST OF TABLES

TABLE Page

1. INTRODUCTION

1.1 Overview

The United States relies more heavily on roadways for both commercial and private transportation compared to other parts of the western world. The construction, maintenance and rehabilitation of pavements is a billion dollar industry. According to the National Asphalt of Pavement Association, approximately 83% of paved roads are asphalt. Asphalt pavement although a general term is specifically used to refer to hot mix asphalt type of pavements. Hot mix asphalt is a combination of both aggregate and asphalt binder. Typically 95% of the hot mix asphalt is composed of the aggregate or stones, and only 5% of the hot mix asphalt is composed of bitumen or asphalt binder. Although asphalt binder contributes little to the makeup of hot mix asphalt, its contribution towards its performance is significant. The viscous and adhesive nature of asphalt binder dictates how well an asphalt pavement performs over time, and how well it responds to the traffic loads the pavement is being subjected to. The adhesive properties of asphalt binder dictate the strength of the bond between the aggregate the binder and the aggregate. The quality of asphalt binder can be the primary difference between a prematurely failing pavement and a long lasting one. Hence, the understanding of the asphalt binder mechanical and chemical properties and its contribution to pavement performance is of utmost importance to asphalt researchers. In addition the cost of asphalt binder prices have risen significantly over the last few decades. This has led to the necessity of developing modified binders with enhanced mechanical and chemical properties. Therefore, in order to develop modified binders, research leading to improved understanding of damaging mechanisms within asphalt binder has become one of the primary focuses of the asphalt industry.

The Micellar Model of bitumen defines asphalt to be a combination of different chemical

groups based on polarity that are named saturatues, asphaltenes, resins, and polar aromatics. The saturate fractions were found to be the least polar while the resins and asphaltenes are the most polar. Roberts et al. [50] discuss the contribution of the individual fractions towards the overall performance of the asphalt binder. They state that the asphaltenes contribute to the viscosity or the stiffness of the binder, the polar aromatics provide with ductility, the naphthene aromatics lead to softening of the asphalt binder, and the saturates are liquids that change little with age.

The physical properties and mechanisms that drive asphalt binder behavior are complex in nature. In order to meet the demand of improved field performance with longer durability, a better understanding of the complex mechanisms leading to the degradation of performance and material properties has become necessary. Technological advancement in the field of microscopy has greatly impacted this aspect of asphalt research. The development of experimental techniques such as atomic force microscopy (AFM), scanning electron microscopy (SEM), and X-ray tomography has allowed researchers to examine asphalt binder and asphalt-aggregate mixtures at a much smaller scale compared to traditional testing [21, 4, 2, 28, 44, 20, 33, 34, 42, 44]. These techniques have led to an improved understanding of the chemical and physical natures of the asphalt binder.

The examination of asphalt binder microstructure using the AFM has made considerable progress in the last few decades. Loeber et al. [28, 27] were among the first researchers to report the existence of so called "bee" structures with oblong shaped outline and rippled topography (see figure 1.1). Their work reported an increase in these "bee" structures with an increase in asphaltene content. Jager et al. [20] and Tarefder et al. [54] were able to use AFM indentation and nanoindentation to measure the difference in stiffness amongst the different phases found in asphalt binder. Following the work of Loeber et al. [28, 27] Pauli and Grimes [43] also examined the correlation of asphaltene content with the formation of the bee structures. Their work was found to be in good agreement with Loeber's work and discovered

that the laser used during the AFM process seemed to dissolve the bee structures as the surface was scanned. A more recent work of Allen at el. [4] also examined these bee structures. They reported an increase in the bee structure content with aging and with increasing saturate content within the asphalt binder. They were also able to use AFM indentation to measure viscoelastic creep properties of the different identifiable phases within the asphalt binder. Allen et al. [3] further developed this work and studied chemically doped asphalt binders and used chemical force microscopy using the AFM to study the bee structure formation with respect to the different asphalt fractions ie. saturates, asphaltenes, resins, aromatics. The work of Allen further reinforced the idea that an increase in saturate content led to an increase in the size and concentration of bee structuring at the asphalt binder surface. Allen et al. [3] and Pauli et al. [44] both discussed that the formation of bee structures may not be attributed to just one factor, but a combination of factors and quite possibly may be a result of the incompatibility of different phases interacting with each other resulting in the rippled patterns forming on the surface.

Although there is extensive literature on the formation of structuring at the surface of the bitumen, little research regarding the failure mechanisms in the binder at the micro scale has been completed. Kringos et al. [24] discussed the possibility of the existence of a weak interstitial zone between the bee phase and the surrounding phases. Kringos and co-authors mentioned that the composite response of the material due to loading would result in high stress regions at the boundaries of the bee structures which could result in cracking and damage. Another possible theory for such phenomenon was proposed by Allen [2] which discussed that instead of the cracks propagating in the boundary regions, the bee structures themselves were responsible for the initiation and eventual propagation of cracks. Allen used fracture mechanics to describe the fracture mechanism resulting from high tensile strains induced to the material. In another work, Das et al. [9] examined similar phenomenon by applying thermal cycling to various bitumen samples with different chemical constituents. Their work

discussed that an increase in wax content resulted from higher amount of cracks forming. In order to verify the hypthesis of Kringos et al. [24] further work had become necessary to clearly determine if the microstructuring within asphalt binder had any relationship with the nucleation and propagation of damage at a small scale.

Microscale tensile testing has proved to be an effective method for extracting mechanical properties of thin films. Marek and Herrin [30] were among the first to use tensile testing to examine the relationship between film thikcness and tensile strength. The determined that film thickness and tensile strength were inversely related when the film thickness exceeded 100 μm. Poulikakos and Partl [47] performed uniaxial tensile tests on thin films of asphalt binder at multiple temperatures in order to investigate failure mechanisms. More recently, Sultana et al [53] demonstrated that the tensile strength of bitumen films are independent of film thickness. In this work, the concept of microscale tensile testing is combined with the capabilities of the AFM in order to study the microstructural changes experienced by asphalt binder once subjected to finite amounts of tensile strain.

1.2 Problem Statement

Despite the contribution of numerous studies towards the discovery and understanding of the microstructure of asphalt binder, there is still limited understanding of how this microstructure of asphalt binder is affected by tensile loading and other complex chemical processes such as aging. Allen et al. [4] use AFM imaging and indentation experiments to determine a correlation between the chemical composition of the aged asphalt binder and resulting microstructure and mechanical properties. They determined that an increase in aging led to an increase in the stiffness of different phases present within the asphalt binder.

In this dissertation, the microstructure of asphalt binder is further examined by combining AFM imaging and indentation with numerical methods. The relationship between the microstructure of the asphalt binder and damage resulting from tensile loading determined using AFM techniques is examined. Furthermore the effect of aging on the microstructure,

damaging processes and mechanical properties is also examined. The motivation of this work is to understand how the microstructure is affected by tensile displacements through image analysis techniques under unaged and aged conditions.

1.3 Research Objectives

The focus of this work is to first understand the effect of tip geometry and mechanical properties of the substrate (asphalt binder) on the indentation response. The purpose of this objective is to gain a better understanding of the creep indentation process and how various assumptions made during experimentation affect numerical accuracy of the properties determined. Second, the microstructure of the asphalt binder is analyzed using the atomic force microscope, and its relation to damage is examined using a custom experimental testing protocol. Here the main focus lies on binders that have already exhibited heterogeneity within its microstructure previously determined by Allen et al. [4]. Next, the effect of aging along with tensile loading on the microstructure is also established. The following tasks have been completed in order to meet the objectives of this work:

- The AFM indentation of a asphalt binder treated as a viscoelastic material was examined using the finite element method. The effect of tip geometry and material model parameters on the indentation response was determined.
- The effect of tensile loading on the microstructure of asphalt binder was studied using AFM imaging and the finite element element method. The nanorheology of the different phases were obtained using AFM indentation experiments.
- The microstructure combined with the nanorheology obtained through AFM indentation experiments were used to analyze the stress distribution within the asphalt binder using finite element simulations.

- The effect of aging on the damage evolution of asphalt binder was examined using a combination of numerical techniques and experimental procedures described in detail in latter sections.

- The effect of geometry of asphalt binder microstructure on the resulting stresses were examined using image creation techniques, and virtual experiments performed using the finite element method.

1.4 Dissertation Outline

This dissertation is written according to the guidelines provided by Texas A&M University. The dissertation is organized into five sections as follows:

- Section 1 presents an introduction of the problem at hand including an overview, a problem statement, research objectives, and an outline of the dissertation.

- Section 2 presents the finite element analysis of AFM indentation of asphalt binder.

- Section 3 details the examination the evolution of asphalt binder microstructure due to tensile loading determined using the Atomic Force Microscope and image analysis techniques.

- Section 4 presents the study of the evolution of asphalt binder microstructure due to aging and tensile loading examined using AFM imaging and the finite element analysis.

- Section 5 presents the effect of geometry of microstructure on the mechanical response of asphalt binder treated as a composite.

- Section 6 presents the conclusions reached from this dissertation. In addition section 6 presents detailed recommendations for future work to improve upon and further develop the work completed in this study.

Figure 1.1: AFM phase image exhibiting the formation of oval shaped bee structures with rippled topography

2. FINITE ELEMENT MODELING OF ATOMIC FORCE MICROSCOPE INDENTATION OF ASPHALT THIN FILM

2.1 Introduction

The study of physical properties of asphalt has been the focus of researchers for at least the last half of a century [23, 45]. The cost of asphalt binder has risen significantly over the last few decades. This has prompted research related to binder modification with the goal of engineering modified binders that are inherently more durable. The advancement of technology has enabled the use of devices such as the Atomic Force Microscope (AFM) to image and analyze the properties of asphalt binders at micrometer to sub-micron length scale. Various works in the literature present evidence for the presence of multiple phases in asphalt using AFM imaging [4, 20, 28, 33, 34, 42]. Jager et al. [20] and Tarefder et al. [54] measured differences in stiffness values amongst asphalt phases by using AFM indentation, and nanoindentation. Since asphalt binder is soft, AFM with an appropriate choice of tips, can be used for both imaging and indentation purposes. This allows the users to recognize different micro domains in the asphalt binder in order to assign mechanical properties to these domains. In the context of this study, the term microrheology is defined as the rheology of the micro domains observed during AFM imaging of asphalt binder surfaces. Allen et al. [4] used this approach to semi-quantitatively compare the rheological properties of the different micro domains. Their analysis was semi-quantitive because the cono-spherical nature of the tip shape was not accounted for in the analytical expressions used to quantify the viscoelastic material properties of asphalt binder. The first part of this paper presents the findings from a study conducted to develop an analytical solution appropriate to model nanoindentation of asphalt using an AFM conospherical tip. The second part of this paper demonstrates the use of this analytical solution to back calculate the microrheology of two different asphalt

binders. The analytical expression develoed in this paper provides with a practical methodology for accurately back-calculating viscoelastic properties of asphaltic materials, by taking into account the effects of finite tip radius. The availability of a modified analytical solution that can extract material properties of asphalt accurately provides with simple, time efficient solution to solving a complex problem. Using the analytical solution developed in this work, an AFM can be used to effectively calculate properties of other soft viscoelastic materials in addition to asphalt with high degree of accuracy.

2.2 Overview

The first AFM was developed by Binnig, Quate and Gerber in 1986. Their intent was to overcome the deficiencies of the Scanning Tunneling Microscope (STM). The STM had the capability of imaging only semi-conductive surfaces. However, the AFM was able to image any type of surface making it the superior choice. In addition to imaging, the AFM has also been used to measure properties such as elasticity, plasticity, and hardness of soft materials using indentation. AFM indentation involves applying a specified load to the specimen surface using an indenter with an arbitrary geometry. The resulting indentation depth is measured and analytical techniques are used to back-calculate the modulus and other material properties.

AFM indentation has been studied in detail by researchers from different fields, e.g. cementitious materials, biological science, and polymer science. In most cases AFM indentation has been used to study the elastic properties of materials. Reynaud et al. [49] experimentally determined Young's modulus of individual bi-phase polymer systems, and computed composite values that were found to be in close agreement with nominal bulk values. Du et al. [11] determined nanometer-scale elastic moduli and yield strengths of polycarbonate and polystyrene thin films using AFM nanoindentation techniques. Burnham et al. [5, 6] used the AFM to study nanomechanical properties of graphite and gold. Burnham also studied the effect of van der Waals forces, and plasticity. Oliver and Pharr studied the indentation of

elasto-plastic materials using a Berkovich indenter. Their work proposed a methodology to yield the stiffness of a material using the unloading portion of a stress-strain indentation curve [38, 39]. More recently, the AFM has also been used to quantify the viscoelastic properties of materials. For example, Jones and Grasley [22] developed solutions to determine the time dependent uniaxial compliance of Calcium Silicate Hydrate (C-S-H) based on nanoindentation creep tests on cement paste.

Although there have been many attempts to quantify material properties using AFM and nanoindentation in other fields, the extent to which AFM has been used to quantify the properties of asphalt binders has been limited. Jager et al. [20] used AFM indentation and reported relative differences in stiffness values amongst asphalt phases. Jager et al. also stated that in order to establish a chemo-mechanical link between various phases within an asphalt binder it would first be important to determine the micro-mechanical properties of these constituent phases. In fact, one of the key objectives of this paper is to present the development and illustrate the use of an analytical solution that can be used to obtain the microrheology of the different phases in an asphalt binder using AFM. Tarefder et al. [54] performed nanoindentation on various binders, along with mixes. They reported hardness and Young's moduli of the test materials. The mastic material (materials Passing No. 200 Sieve) was reported to be 2 to 15 times softer than the matrix materials (materials Passing No. 4 Sieve), and the matrix was found to be 10 times softer than the aggregate materials.

The creep response of the AFM tip indenting into a soft time depenedent material is a function of material properties, geometry of the indenting tip and extraneous factors such as temperature. The works of Galin and Sneddon [14, 51] relates the applied load to the depth of indentation for an elastic material indented using different tip geometries. Hertz also provides a solution for the indentation of elastic bodies using a spherical indenter [18, 17]. Both solutions are based on the assumption of infinitesimal strains, and a semi-infinite half space. More recent work involving nanoindentation was carried out by Fischer-Cripps [13], and

Vandamme et al. [57] who provide viscoelastic solutions for creep indentation of materials exhibiting time dependent behavior. Fischer-Cripps uses the work of Radok and Lee [26] and Hertz to construct viscoelastic solutions for the spherical and conical indenters. The solutions are based on mechanical analog models that utilize springs and dashpots to represent viscoelastic behavior. Van Damme used Laplace transforms in order to obtain the time dependent solutions from Radok and Lee's linear solutions. Van Damme derived solutions for viscoelastic materials that can be represented by a 3-parameter Maxwell model, 4-parameter Kelvin-Voigt model, and 5-parameter Kelvin-Voigt-Maxwell model. In another work Jones [22] derived a viscoelastic solution using similar method as Vandamme but was not restricted to mechanical analog models and could be used with any creep compliance function. Jones assumed a constant Poisson's ratio and a conical indenter for his solution. Grasley et al. [16] used a numerical scheme to account for the effect of a conospherical tip geometry for the extraction of viscoelastic properties of soft materials using AFM indentation.

Finite Element Method (FEM) is a common tool to obtain numerical solutions for problems that are difficult to analyze analytically. Various researchers have used this method to study indentation at small scales. Cho and Park performed finite element studies to study the effect of adhesion on contact [7]. Their work uses the Maugis-Dugdale model to analyze the interactive forces between the indenter and the contact surface of the target specimen. The results show good agreement between the numerical values and theory. In another work Zhang et al. use the finite element method to study nano-scale adhesive contact of elastic bodies [60]. Zhang compared the conventional Hertz, JKR, and DMT models. Their work shows that tip geometry plays a dominant role on the pull-off strength. Zhang also found that the cup shaped tip has the highest adhesion efficiency followed by the flat punch tip, sphere tip, and the mushroom tip, respectively. Poon et al. [46] also studied the AFM indentation using the finite element method, and derived a correction to the Sneddon solution to account for the finite tip radius effect. They concluded that the error due to the finite tip radius can be

significant especially at lower depths of indentation, and developed an algebraic expression to account for it.

In summary, previous studies have shown that the AFM can be used to obtain mechanical properties of a material by using it as a nanoindenter. However, other researchers have also demonstrated that the analytical methods to obtain material properties from such nanoindentation tests must be carefully considered for a given material and indenting tip configuration. In this paper we use the finite element method to study the effect of the finite tip radius on the viscoelastic indentation of a thin film of asphalt binder using a conospherical AFM tip. Results from the finite element simulations were compared to different analytical solutions. These comparisons were then used to develop a modified analytical solution for the viscoelastic indentation using conospherical tips. Finally, the modified solution was used to backcalculate the micro-rheological properties (creep compliance parameters) of two different binders.

2.3 Theoretical Background

2.3.1 Elastic and Viscoelastic Solutions

A typical AFM based indentation test consists of applying a constant load P through an indenter with a predefined shape (four-sided, spherical, conospherical) and measuring the penetration depth h as a function of time. Figure 2.1 illustrates the schematic of an ideal conical and a realistic conospherical indenter that is typically used for AFM imaging and indentation of soft materials.

The resulting creep data from the AFM indentation experiment can be used with the solution for a conical or spherical tip to obtain the microrheology of the binder. Note that the time versus indentation depth (creep) data obtained directly from the AFM is not creep in the conventional sense because the contact area between the tip and the substrate and corresponding stress may change with time even though the applied load is constant.

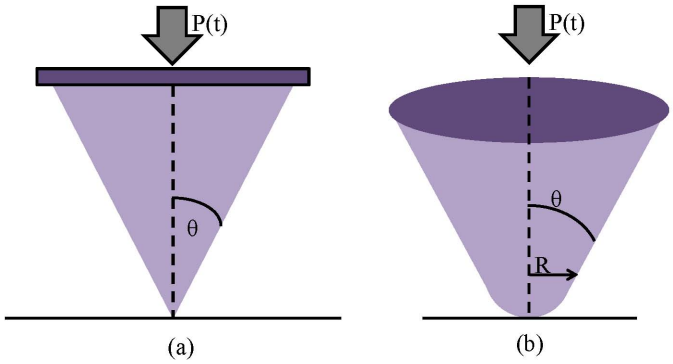

Figure 2.1: (a) Conical indenter geometry: θ is the cone angle (b) Conospherical indenter geometry with cone angle of θ, radius R, and contact area of, and $P(t)$ is the load applied

Various solutions for static indentation are available in the literature. These solutions are based on the tip geometry, and material properties. The spherical tip is ideal for AFM indentation, because from an analysis point of view, well established analytical solutions are readily available in the literature for a linear elastic material. The conical sharp tip is ideal for imaging due to its ability to provide with high resolution images. In a typical AFM test to obtain the microrheology of asphalt binders, it is important to use the same tip for both imaging and nano-indentation. This allows the user to precisely associate measured properties to specific phases obtained from the image. For this reason, the conical tip is more suitable to image and perform indentation as illustrated in the work of Allen et al. However in practice, the conical tips are not perfect cones with a zero radius of curvature at the tip. In fact, the tips are conospherical (as shown in Figure 2.1) (b). Therefore a solution that describes the indentation response under the loading from such tips is better suited for determining the microrheology of asphalt binders. The following paragraphs describe the development of this solution for a conospherical tip.

The two extreme approximations for a conospherical tip are the hemisphere and the perfect cone. Solutions for these two cases are discussed below. The Hertzian solution for the

indentation of an elastic material using a hemispherical indenter can be given by [18]:

$$P = \frac{4}{3} E^c R^{1/2} h_t^{3/2} \tag{2.1}$$

where P is the load applied, E^c is the combined modulus, R is the radius of the rigid spherical indenter, and h_t is the depth of the indentation. The combined modulus E^c is given by:

$$\frac{1}{E^c} = \frac{(1-\mu^2)}{E} + \frac{(1-\mu'^2)}{E'} \tag{2.2}$$

where E is the modulus of the substrate material, and E' is the modulus of the indenter. μ, and μ' here are the Poisson's ratio of the specimen and the indenter respectively. In the case of an indenter that has much higher stiffness compared to the substrate material being indented (which is typically the case with silica indenters on asphalt binder samples) the relation reduces to:

$$E^c = \frac{E}{1-\mu^2} \tag{2.3}$$

While the Hertzian solution is applicable for hemispherical tips, the Sneddon solution [51] is applicable for the indentation of an elastic material using a conical tip. The solution is given as:

$$h^2 = \frac{\pi}{2tan\theta} \frac{P}{E^c} \tag{2.4}$$

where E^c is the combined or indentation modulus given in Eq. 2.3, θ is the cone half angle of a conical indenter, and h is the depth of the indentation. It is important to note that both the Sneddon and the Hertzian contact solutions are based on a few assumptions:

- a defined geometry (spherical or conical and not a combination),
- an infinitely large incompressible specimen,
- a homogeneous, isotropic, linear elastic material, and
- Infinitesimal deformations.

Sneddon's solution for a conical indenter and Hertz solution for a spherical indenter have been extended by other researchers for time dependent materials. Vandamme and Ulm [57] provide a set of solutions for a conical indentation of viscoelastic material that can be represented using mechanical analog models with spring and dashpots. Vandamme et al. used the method of function formulations of viscoelasticity to derive viscoelastic solutions by performing Laplace transforms on Sneddon elastic solution. Fischer-Cripps followed the work of Lee and Radok [26] and used a correspondence principle to convert an elastic solution to a time dependent solution by using Laplace transform. In another work Jones et al. [22] used a similar technique to develop a viscoelastic indentation solution for a conical indenter with the assumption of a constant Poisson's ratio. Note that the above extensions of elastic solutions to time dependent materials were based on Laplace Transformation, which is not generally valid for problems with arbitrarily growing or reducing contact area. However, Lee and Radok [26] demonstrated that the correspondence principle may be used for contact problems provided that the contact area is increasing. Therefore, it is important to note that a solution obtained using the correspondence principle is only valid for the loading portion of the experiment.

The aforementioned extensions of the Hertzian and Sneddon solutions for a hemispherical and conical indenter for a time dependent material are summarized below. Assuming a linear

elastic material which experiences small levels of deformation we can express Eq. 2.1 as follows:

$$h_t^{3/2} = \frac{3}{4}\frac{P(1-\mu^2)D}{R^{1/2}} \tag{2.5}$$

where D is the elastic compliance of the given material. Assuming a linear viscoelastic material, and linearity of response due to superposition we can now transform the elastic solution into a time dependent solution as [58]:

$$h_t^{3/2}(t) = \frac{3}{4}\frac{(1-\mu^2)}{R^{1/2}}\left[P_0 D(t) + \int_{0^+}^{t} D(t-s)\frac{dP}{ds}ds\right] \tag{2.6}$$

where s is a time variable, P(s) is the loading history, and D(t) is the creep compliance of the material. Similarly the viscoelastic solution for a conical tip geometry can be derived from the Sneddon solution and is given as follows:

$$h^2(t) = \frac{\pi(1-\mu^2)}{2tan\theta}\left[P_0 D(t) + \int_{0^+}^{t} D(t-s)\frac{dP}{ds}ds\right] \tag{2.7}$$

If we assume a constant load P_0 the second part of Eq. 2.6 and Eq. 2.7 reduces to zero and for the spherical and conical solution respectively we obtain:

$$h_t^{3/2}(t) = \frac{(1-\mu^2)}{R^{1/2}}\left[P_0 D(t)\right] \tag{2.8}$$

$$h^2(t) = \frac{\pi(1-\mu^2)}{2tan\theta}\left[P_0 D(t)\right] \tag{2.9}$$

In this work we use a three element Voigt spring-dashpot analog model to represent the

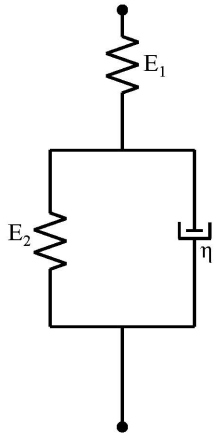

Figure 2.2: Voigt spring and dashpot viscoelastic model

viscoelastic behavior of asphalt binder, shown in Fig. 2.2. It is important to note here is the voigtspring model does not contain a pure viscous term which can account for a viscoelastic fluidlike long term behavior. However, the focus of the work here is to quantify the viscoelastic creep properties for short term creep data ranging no more than a a few seconds in time length. The creep compliance for this given analog model is defined as follows:

$$D(t) = \left[\frac{1}{E_1} + \frac{1}{E_2}(1 - e^{-tE_2/\eta})\right] \tag{2.10}$$

However, as mentioned before, the geometry of the tip used for imaging and indentation is conospherical as opposed to the two extremes of a hemisphere and cone represented in equations 2.1 and 2.4. Consequently, one of the objectives of this work was to use the finite element method to compute the deformation in a thin film of asphalt using a conospherical tip geometry and compare it to the analytical solutions provided for both spherical and conical elastic and viscoelastic solutions. The hypothesis was that, these comparisons could be used to determine the most appropriate analytical solution to obtain the microrheology of

binders using indentation data obtained through AFM indentation of asphalt thin film with a conospherical tip.

2.3.2 Finite Element Model

Sharp indenters used in practice are not infinitely sharp, and hence contain some level of spherocity to the tip. Typically the term "conospherical" is used to refer to these types of tips, as shown in Fig. 2.1b. This conospherical tip would be expected to behave differently than a spherical or a conical tip. An infinitely sharp conical tip is able to indent any material with much less effort than a conospherical tip. The study of this phenomenon is part of the focus of this work. Here, an axisymmetric finite element model is developed to simulate the static and time dependent indentation of asphalt thin film under a constant load using Abaqus CAX3 (3 noded axisymmetric) elements. Typically an AFM tip is approximately 1 micron in length. A 200 nm long and 80 nm wide portion of the indenter was modeled to obtain numerical efficiency. The ranges of radii considered here were between 5-9 nm, which is well representative of PPP-NCL NANOANDMORE tips used for the experimental portion of this study. The cone angle of the indenter is approximately 21°. The typical dimensions of asphalt thin film used in AFM indentation experiments as part of this study are approximately 1 micron in height, 75 mm in length, and 20 mm in width. Here, only a 250 nm wide and 200 nm high portion of the film is modeled for numerical efficiency. The height of the thin film was ensured to be adequate to minimize the effect of the substrate. The depth of the indentation was kept fairly shallow and stresses are mostly contained to the top half of the film. This was done to ensure that large levels of deformation do not occur, since this level of deformation in actuality would introduce plastic deformation. Figure 2.3 shows a magnified view of the finite element mesh for the tip along with the specimen at the point of contact.

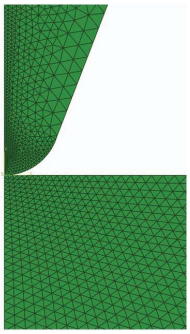

Figure 2.3: Close up view of indenter and specimen mesh

2.3.3 Preliminary Investigation: Indenting an Elastic Material

Initially both the indenter and the asphalt thin film were assumed to be linear elastic. In order to simulate the the relatively rigid nature of the indenter, the indenter was assigned a much higher modulus than the specimen. According to Huang [19] at low tempeartures and high loading frequencies the stiffness modulus of asphalt binders approach a limit of 3 Gpa. Assuming a softer asphalt binder at room temperature, the specimen was assigned a Young's modulus of 0.103 GPa (15,000 psi), and the indenter was assigned a modulus value of 1×10^6 GPa. Typical Poisson's ratio for asphaltic materials can range between 0.1 to 0.5 [29]. For this work a Poisson's ratio of 0.3 is used. The first part of the finite element simulation involved static loading of the tip using a constant concentrated load. The concentrated static load of 5 nN, consistent with the creep AFM test is applied in the y (vertical) direction at the top of the tip. The response was examined and compared against the Hertz and Galin-Sneddon solution.

The finite element static indentation solution is shown in Table 2.1 and compared to both the Sneddon and Hertz solution. The finite element results are very close to that of the Hertzian solution for a hemispherical tip with radius of 5 nm. This can be attributed to the sphericity of the tip wherein the contact between the tip and the material is dominated by the spherical portion of the tip and contribution from the conical part of the tip is negligible. An

analogy here is the the process of pressing a soft sponge using the tip of the finger. In this case little to no contact is made with the side of the finger at low levels of indented depth. The finite element simulation here is also performed with low load levels consistent with load used during AFM indentation experiments, to ensure fairly shallow depth of indentation compared to the radius of the indenter itself. This is done to ensure realism, since from a practical standpoint any material loaded beyond a certain point would exhibit plasticity (permanent deformation), and therefore would make extremely large levels of elastic deformation highly unlikely.

Table 2.1: Static Indentation Results Comparison

Sneddon Indentation Solution (Depth in nm)	Hertz Indentation Solution (radius 5 nm) (Depth in nm)	Finite Element Results (Depth in nm)	Force Applied (nN)
13.45	6.03	6.24	5.00
19.02	10.20	10.33	5.00
23.29	13.36	13.98	5.00

2.3.4 Parametric Analysis for Indentation of a Viscoelastic Material

The finite element method was used to conduct a parametric analysis for the AFM indentation of a viscoelastic material. As mentioned before, the objective of this parametric analysis was to determine the most accurate analytical closed form solution for AFM indentation using a conospherical tip. The ultimate goal was to use the aformentioned solution to estimate microrheology of asphalt binders using AFM indentation. A summary of this parametric analysis is presented in this section.

In Abaqus, the finite element software used for this parametric analysis, a viscoelastic material is characterized using the Prony series as follows:

$$g(t) = 1 - \sum_{i=1}^{n} g_i(1 - exp(-t/\tau_i)) \tag{2.11}$$

where $g(t) = G(t)/G_0$ is a non-dimensional shear relaxation moduus. Here g_i and τ are the time dependent prony series parameters, and g_i is calculated based on G_0 and G_n(time dependent prony series shear modulus parameter). The finite element results are then compared to viscoelastic analytical solutions derived in the previous section. $G(t)$ is the time dependent shear relaxation modulus of the specimen, and G_0 is the instantaneous shear modulus of the specimen, which is calculated internally by using the specified Young's Modulus E and the Poisson's ratio μ of the material. A one term prony series was used for this study, and the material properties E, g_1, τ, and the radius of the indenter R were varied for the parametric analysis. The cone angle was kept at a constant value of 21°, based on typical cone angle values of manufactured sharp AFM indenters. The viscoelastic finite element analysis was performed for a period of 30 seconds, and the instantaneous indentation depth h_0 and the final depth of indentation h_t due to the creep indentation is determined. Table 2.2 lists the range of values for the aforementioned parameters. This range of values was arrived at based on relaxation properties of typical asphalt binders at 25°C. A total of 256 simulations were conducted. The indentation depth from the simulations were compared to the indentation depth from the analytical solution for a hemi-spherical indenter.

Table 2.2: Parameter Values for Parametric Study

Parameter	Values			
R in nm	5	7	9	11
E in MPa	0.103	0.203	0.303	0.403
g_1	0.585	0.62	0.659	0.705
τ	0.342	0.372	0.402	0.432

The comparisons revealed that there was a significant difference between the simulation and analytical solution for a hemi-sphere, espeically in the time dependent portion of the deformation. Based on the comparisons, the analytical solution for the hemispherical indenter was modified to include two modification factors α and β. The modified analytical solution is:

$$h_t^{3/2}(t) = \frac{(1-\mu^2)}{R^{1/2}} P_0 \left[\alpha \frac{1}{E_1} + \beta \frac{1}{E_2} (1 - e^{-tE_2/\eta}) \right] \tag{2.12}$$

For α a modification factor of 0.90 was determined, and for β a modification factor of 0.77 was determined. These values were able to reduce the error for the time dependent portion of the solution from approximately 20% to a range between 1 and 5%. Figure 2.4(a) to Fig. 2.4(d) shows the error between the $h_t - h_{0FEM}$ and $h_t - h_{0ANAL}$ as a function of non-dimensionalized material parameter g_1 (see Eq. 2.11), where h_t is the final depth of indentation and h_0 is the instantaneous depth of indentation. Figure 2.5 shows the total depth of indentation as a function of material parameter g_1.

2.4 Experimental Methods and Analysis

2.4.1 Methodology

We start here with Eq. 2.12 with modification factors α and β as 0.9 and 0.77 as discussed in the previous section. The following is a brief summary of the sequence of steps that were performed to obtain the phase distribution and indentation curves for different asphalt binders. A more detailed description of the experimental procedure can be found in the work of Allen et al. [4].

- Two binders AAD and ABD were selected for this study. These two binders were obtained from the Strategic Highway Research Program (SHRP), Material Reference Library (MRL). The detailed chemical and mechanical properties of these binders can

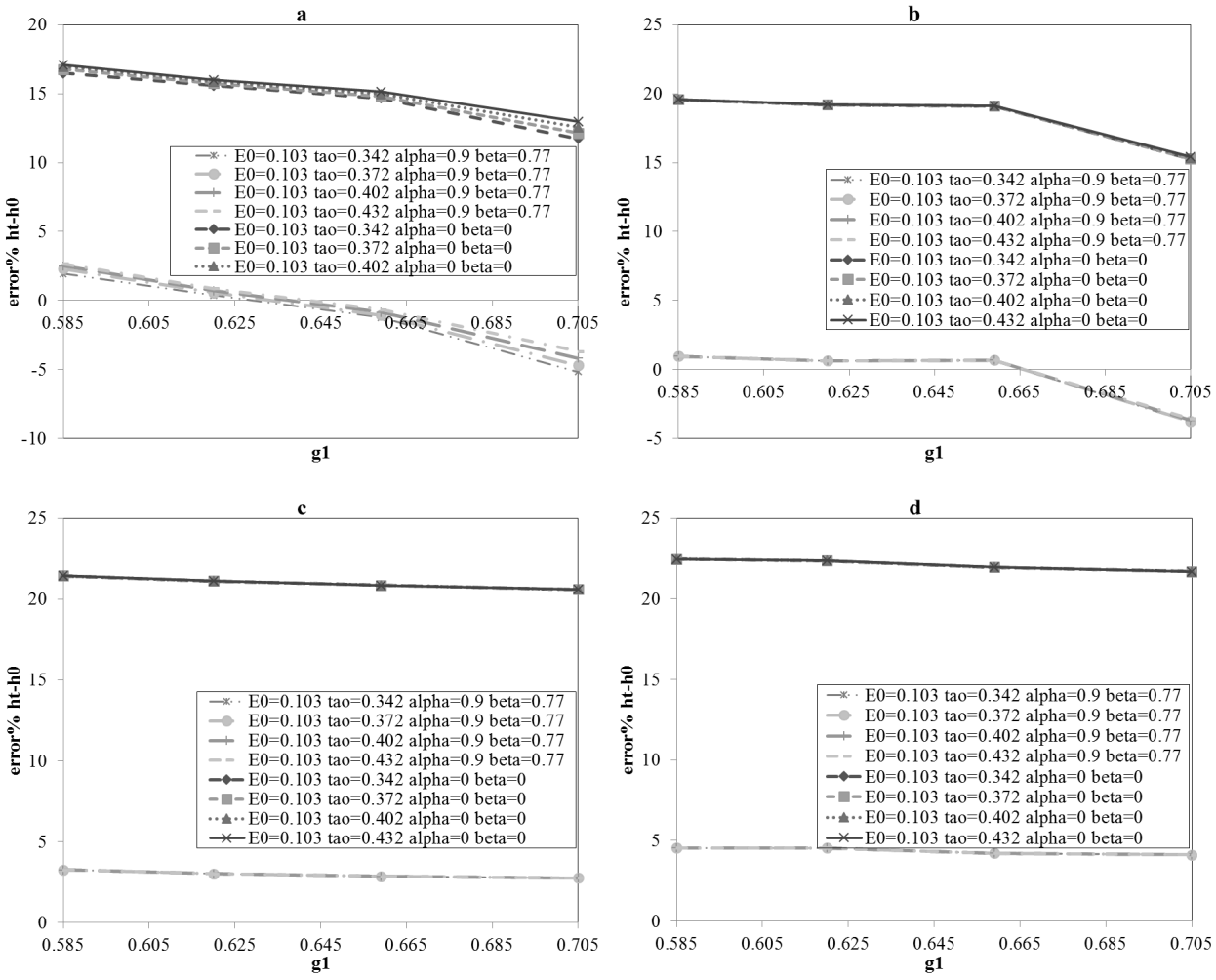

Figure 2.4: (a) %error $h_t - h_0$ for conospherical indenter with radius of 5nm (b) %error $h_t - h_0$ for conospherical indenter with radius of 7nm (c) %error $h_t - h_0$ for conospherical indenter with radius of 9nm (d) %error $h_t - h_0$ for conospherical indenter with radius of 11nm

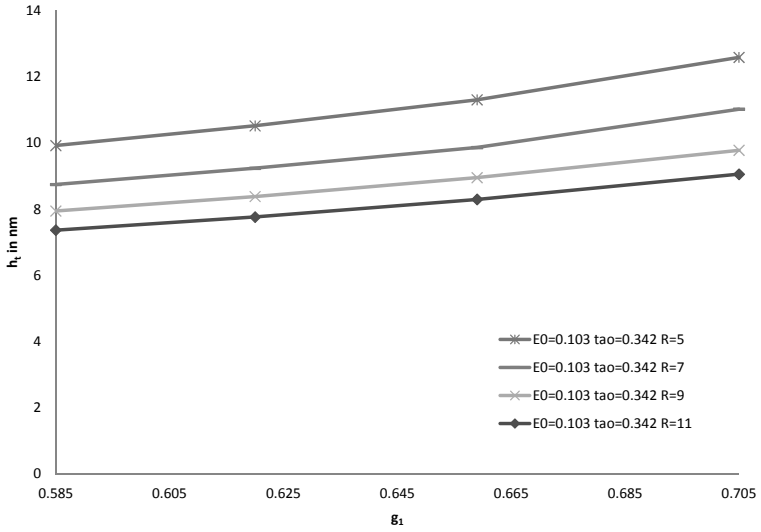

Figure 2.5: Total depth of indentation as a function of material parameter g_1 (FEM)

be found in [37]

- The Agilent 5400 AFM system was used to perform imaging and indentation on aged and unaged samples using silicon nitride tips, and the tests were carried out at room temperature (25°) . The main component of the system is a microscope, which includes the scanner, sample stage, high-resolution probe/tip and detector. Other essential equipment included a high-speed computer, an AFM controller and head electronics box (HEB). Optional equipment included an environmental enclosure and vibration isolation stage to control vibrations, air turbulence and acoustic noise. All aspects of the AFM, including alignment, calibration and imaging were controlled by a software package called PicoView©.

- A cono-spherical tip was used to perform imaging on a 25 micrometer x 25 micrometer portion of the asphalt binder. The imaging clearly showed that the asphalt binders AAD and ABD comprised of two distinct phases: a dispersed phase and a continuous phase. Immediately after imaging, the AFM tip was then directed to approximately

10 randomly selected points within each phase to perform the indentation experiment. A constant load of 5 nN was applied at each location while the indentation depth was recorded. A semi-quantitative analyses of this creep data clearly demonstrated that the mechanical properties of the different phases within the asphalt binder were significantly different from each other.

- Imaging was also conducted on long-term aged samples of these asphalt binders. Long-term aging was found to clearly induce microstructural changes in the asphalt binder by changing the phase structure and distribution. As with the unaged binder, indentation was also performed on each of the different phases that were imaged. Once again, a preliminary analyses of the creep data demonstrated that not only was the mechanical response different for each phase within the binder, but it was also different from the mechanical response of a similar phase in the unaged binder.

2.4.2 Analysis and Results

In this section, we examine the results obtained from the AFM creep indentation of asphalt binder AAD, ABD. More specifically, we will use the measured indentation versus time curves with the viscoelastic spherical solution (Eq. 2.12 to determine the nano-rheological properties of the different phases within the asphalt binder before and after aging. Figures 2.6 through 2.9 show AFM surface images, along with creep data recorded unaged and aged binder AAD, and ABD respectively. Note that the creep, or more correctly, the indentation versus time curves shown in these figures is the average measurements made at several locations within each phase. The experimental data for very low levels of deformation contained noise, which was reduced by applying a polynomial fit. It is important to also note that the original experimental data contained very large levels of deformation. For this purpose, the data was reduced and the fit was applied to the indentation data for a shorter period of time yielding more realistic viscoelastic properties associated with small deformations.

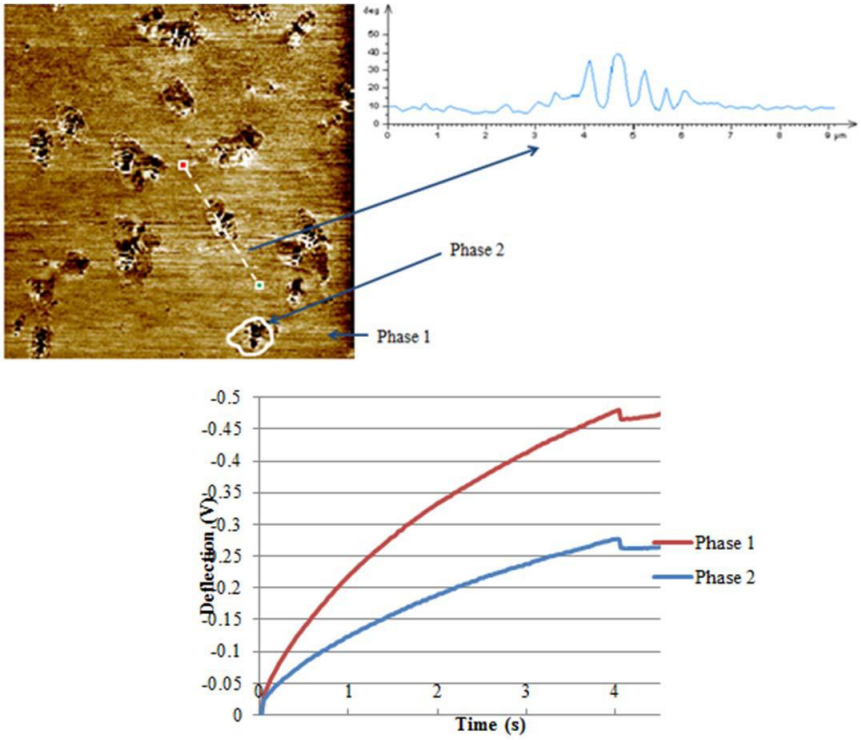

Figure 2.6: Phase image, profile extraction and creep measurements for unaged asphalt AAD [4]

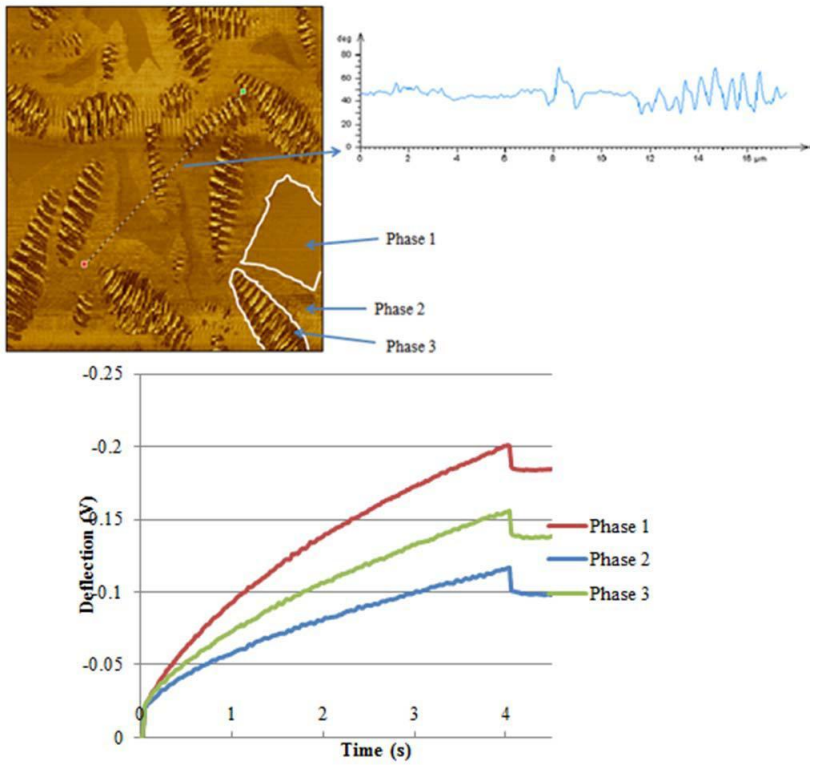

Figure 2.7: Phase image, profile extraction and creep measurements for aged asphalt AAD [4]

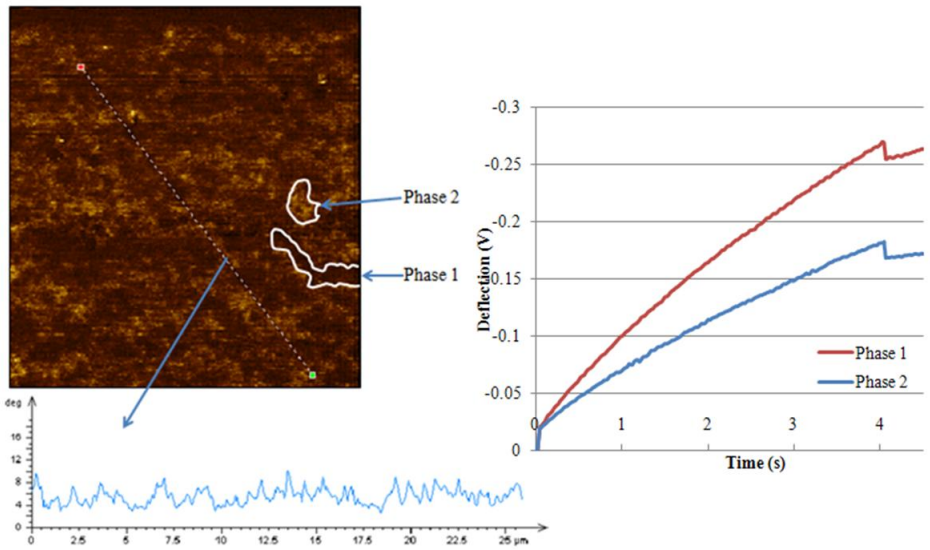

Figure 2.8: Phase image, profile extraction and creep measurements for unaged asphalt ABD [4]

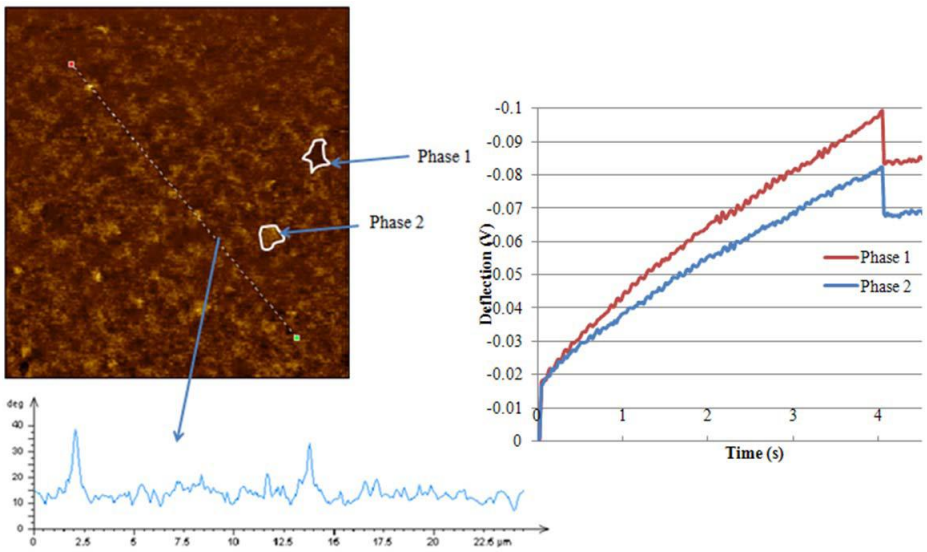

Figure 2.9: Phase image, profile extraction and creep measurements for aged asphalt ABD [4]

The next step involved the use of Excel solver function to perform a least squares analysis, to fit the recorded data to the modified viscoelastic spherical function show in Eq. 2.12. The instantaneous modulus calculated, may have been influenced by the rising time effect. However, the error expected due to this effect will introduce a small bias and the relative comparison of E1 (instantaneous modulus) between different phases or conditions would still be meaningful. Figures 2.10 to 2.11 show the unaged and aged creep indentation data along with modified viscoelastic spherical solution fit for binder AAD. Figure 2.12 to 2.13 show the unaged and aged creep indentation data along with modified viscoelastic solution fit for binder ABD. The fit parameters obtained through these fits are shown in Table 2.3, and. The units for E_1, E_2, and η are in N/m^2, N/m^2 and $Pa.s$ respectively.

2.5 Discussion

The numerical analysis of an AFM indentation experiment using small loads and a cono-spherical tip behaves closer to a tip with a hemispherical shape, rather than a perfectly conical tip. Consequently, the Hertz solution may well represent the indentation experiment under

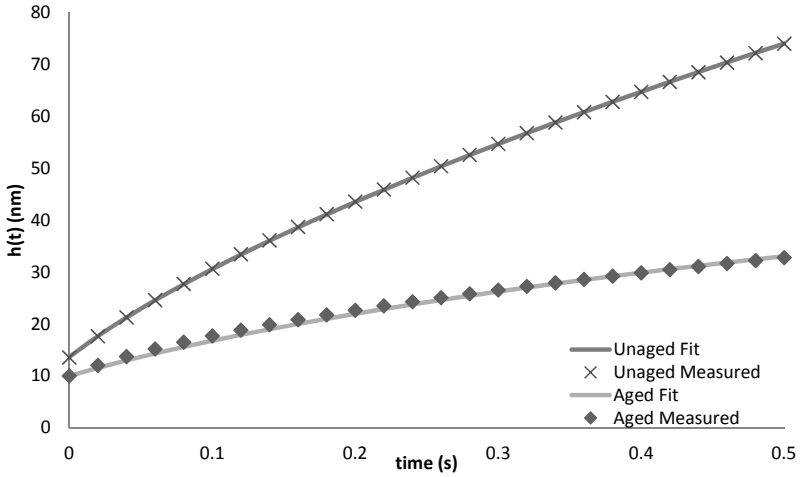

Figure 2.10: Depth of indentation as a function of time for unaged and aged asphalt AAD continuous phase (identified as Phase 1 in Figure 2.6) [4]

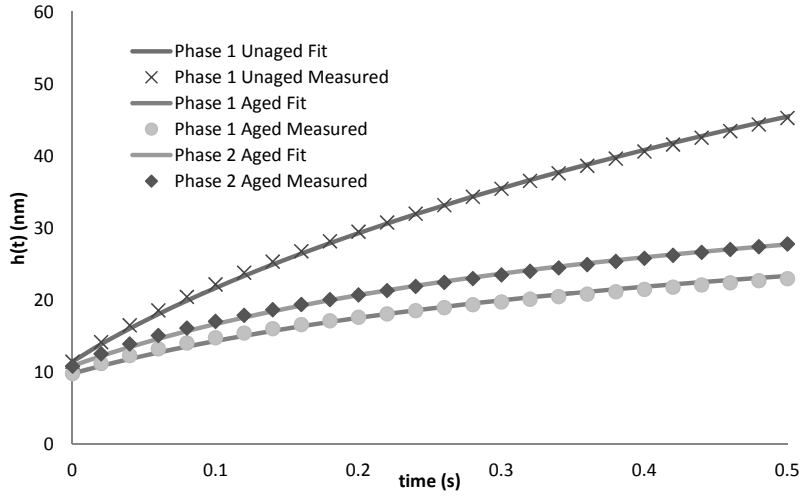

Figure 2.11: Depth of indentation as a function of time for unaged and aged asphalt AAD discrete phases (identified as phases 2 and 3 in Figure 2.7) [4]

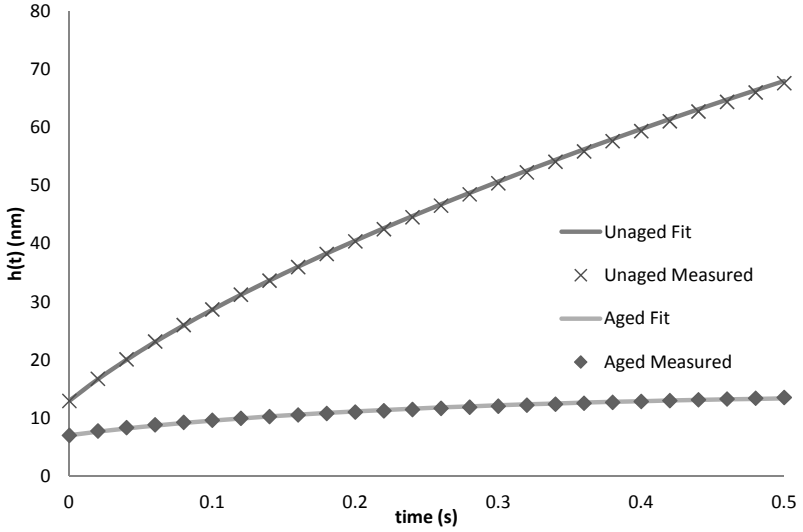

Figure 2.12: Depth of indentation as a function of time for unaged and aged asphalt ABD continuous phase (identified as phase 1 in Figure. 2.8) [4]

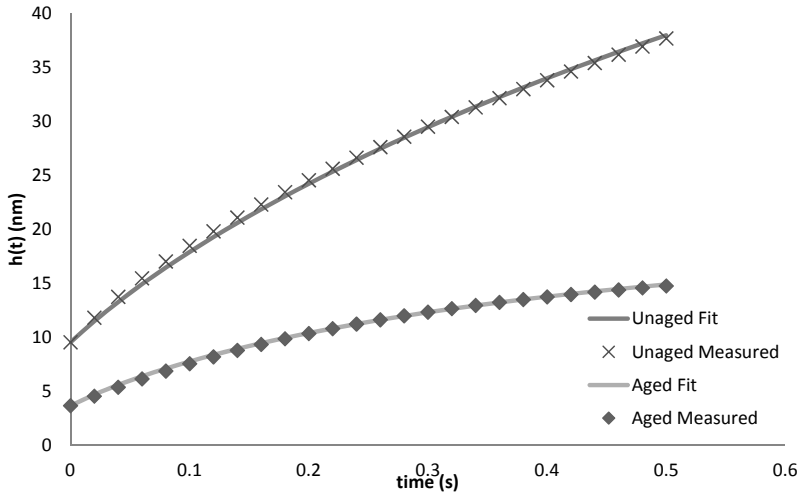

Figure 2.13: Depth of indentation as a function of time for unaged and aged asphalt ABD discrete phase (identified as phase 2 in Figure 2.8 and Figure 2.9) [4]

Table 2.3: Fitting parameters for binder AAD viscolelastic spherical indentation modified solution

Binder	Parameter	Phase 1 Unaged	Phase 2 Unaged	Phase 1 Aged	Phase 2 Aged	Phase 3 Aged
AAD	E_1	2.75×10^7	3.55×10^7	4.40×10^7	4.48×10^7	3.86×10^7
AAD	E_2	5.14×10^4	1.40×10^6	2.50×10^6	9.00×10^6	7.00×10^6
AAD	η	1.09×10^6	2.00×10^6	3.34×10^6	5.00×10^6	3.60×10^6
ABD	E_1	2.95×10^7	4.69×10^7	7.40×10^7	1.99×10^8	N/A
ABD	E_2	2.00×10^5	1.57×10^7	3.20×10^7	1.50×10^7	N/A
ABD	η	1.20×10^6	2.71×10^7	1.00×10^7	8.00×10^6	N/A

such conditions.

For an elastic material, the numerical analysis shows that the material response indented by a conospherical tip agrees well with the Hertz solution for a hemispherical tip. However, the time dependent numerical solution (creep deformation) shows significant deviation from the Hertz viscoelastic solution (Eq. 2.8), with between 15% to 20% error. The modification factors introduced are able to successfully reduce this error to acceptable values of 1 to 5% error. This is important, considering even a small error in the time dependent solution can lead to major deviation in the calculation of the viscoelastic material parameters.

Figures 2.10 and 2.11 show the creep indentation data along with the modified viscoelastic spherical solution fit for asphalt binder AAD. After ageing, both the continuous, and the discrete phases showed an increase in the instantaneous modulus resulting in a smaller elastic deformation. The continuous aged phase deformed half as much of the unaged. The discrete phase for the aged binder also experience half the amount of deformation as the unaged phase. Phase 2 discrete phase (bee like) was found to be more stiff than the unaged discrete phase 1, but less than the aged discrete phase 1.

Figures 2.12 and 2.13 show the creep indentation data along with the viscoelastic spherical modified solution fit for asphalt binder ABD. For this binder, the data indicated that

the binder experienced significant stiffening due to aging. Both the continuous, and discrete phases were found to experience less instantaneous and time dependent deformation for the aged phases as opposed to the unaged ones. The aged continuous phase here was found to experience significant stiffening, resulting in only 20% deformation of the unaged sample. The aged discrete phase was found to deform approximately 40% of the unaged phase. However, aging did not lead to the formation of the bee like structures (AAD discrete phase 2). Both binder AAD, and ABD were find to be similar in terms of both instantaneous and time dependent modulus. The continuous phase in binder AAD experienced less stiffening due to aging than the continuous phase in binder ABD. However, the discrete aged phases of binder AAD were determined to be stiffer than the discrete phase of binder ABD.

The focus of this study was to quantify the time-dependent response of the various phases within the asphalt binder. Table 2.3 presents the microrheological properties of the asphalt binder. These properties were estimated using equation 2.12 and AFM indentation experiments. It is well established that the stiffness of the bulk binder increases with oxidative aging. The material properties listed in Table 2.3 demonstrate that this increase is consistent, albeit at different rates, amongst the different phases in the asphalt binder. In all cases the total creep was reduced from the unaged to the aged sample. Results also indicate that the one term prony series approximation, which was the creep compliance function chosen for this study, was adequate to describe the time dependent behavior obtained from AFM indentation of the phases within the asphalt binder. Regardless, in the future solutions incorporating extra terms in the creep compliance function should also be explored. However, this also increases the complexity in determining the modification factors and determining material constants.

During larger levels of deformation, other phenomena such as strain hardening, plasticity may very likely be present, and will therefore have a large effect on the outcome. The material behavior examined here is constrained to the surface of the specimen. This behavior may or may not be present in the same concentration throughout the depth of the material. Hence,

it is important to establish that the phenomena examined here may entirely be a surface phenomena and may not extend to the bulk level. This matter needs to be addressed in future research, and will lead to a better understanding of volumetric composition of asphalt binder.

Kringos et al. [24] discuss the formation of high stress regions around phases that evolve in asphalt binders due to kinetic processes. These high stress regions eventually lead to cracking and failure. The work described here can be used to provide material properties required for such failure analyses, and help uncover the complex processes that lead to the degradation of mechanical properties in asphalt binder.

2.6 Conclusions

The main objective of this work was to present the development of a modified viscoelastic spherical indentation solution and demonstrate its ability to analyze the time dependent response of a soft material under a cono-spherical tip of an AFM. The solution was used to determine the microrheology, i.e., the creep compliance properties of different phases, of two different asphalt binders before and after long-term aging. The following are some of the conclusions that can be drawn from this study:

- The modified viscoelastic solution was found to be suitable to analyze creep data obtained from nano-indentation of different phases of the asphalt binder using the AFM. The solution resulted in meaningful creep compliance parameters for the two binders based on a Voigt model.

- For a given binder and aging condition, the continuous phase was typically less stiff than the discrete phase/phases. Elastic (instantaneous) and time dependent (viscoelastic) responses were quantified in terms of material constants according to the Voigt model by means of the modified viscoelastic solution. The ability to characterize the individual phases according to this methodology offers a means for characterization of the rheological responses of the composite (comprised of all phases) as well as the

promise of being able to predict and quantify damage at this length scale. This is a first step in the evaluation of damage and healing characteristics at a length scale not normally considered and for nano-characterization and nano-modification.

- The stiffness of individual phases for both AAD and AAB consistently increased after aging. The overall stiffness of the aged phases were upto three times that of the unaged phases. While the increase in stiffness of the binder due to aging is expected, it is important to note that the modified viscoelastic spherical solution could be used to quantify these changes within the different phases of the asphalt binder.

Future work in this area will include, the development of an analytical solution with multiple term prony series along with the updated modification factors. Surface forces such as van der Waals forces during the initial contact period must be incorporated into the solution. Other complex material behavior such as plasticity, and the coupling of plasticity and viscoelasticity may yield more realistic material response, and hence must be studied. The material behavior as a bulk must be examined, to ensure whether the observed material response is not only limited to the surface of the specimen. These steps will lead to more clear and in depth understanding of the AFM indentation of asphalt thin film. Proper quantification of the viscoelastic properties of micro-constituents of asphalt thin film can lead to the understanding of the effects of temperature, aging, binder modifiers etc. The formation of additional phases through the process of aging can help explain the evolution of asphalt behavior under different environmental conditions.

3. THE EVOLUTION OF ASPHALT BINDER MICROSTRUCTURE DUE TO TENSILE LOADING DETERMINED USING THE ATOMIC FORCE MICROSCOPY AND IMAGE PROCESSING TECHNIQUES*

3.1 Introduction

The study of the physical properties of asphalt binder or bitumen is motivated by economic implications. Due to the significant rise in bitumen prices over the last few decades, engineering of modified binders with enhanced properties has become one of the main focuses of the asphalt industry. In order to engineer binders that can deliver improved field performance with longer durability, a better understanding of the complex mechanisms that drive the degradation of binder properties is necessary. Technological advancement in the field of microscopy has greatly facilitated this aspect of asphalt research. The development of experimental techniques such as atomic force microscopy (AFM), scanning electron microscopy (SEM), and X-ray tomography has allowed researchers to examine bitumen and asphalt mixtures at a much smaller scale [4, 2, 28, 44, 20, 33, 34, 42]. These techniques have led to an improved understanding of the link between the microstructure of the bitumen (or bitumen-aggregate composite) and the resulting mechanical processes during loading that lead to distresses such as fatigue damage and cracking.

During the last few decades the ability to examine bitumen using an AFM has resulted in considerable improvements in the understanding of the bitumen microstructure and behavior. Techniques for using the AFM to investigate the bitumen microstructure have also significantly improved during this time. Loeber et al. [28, 27] were among the first to report the existence of so called “bee” structures with an oblong shaped outline and rippled topogra-

*Reprinted from "Evolution of asphalt binder microstructure due to tensile loading determined using AFM and image analysis techniques" by Rezwan Jahangir, Dallas N. Little, and Amit Bhasin. International Journal of Pavement Engineering, 16(4), 337-349,2015, ©(2015) with permission from IJPE

phy (see figure 3.1). They reported an increase in these "bee" structures with an increase in asphaltene content. Jager et al. [20] and Tarefder et al. [54] were able to use AFM indentation and nanoindentation, respectively, to measure the differences in stiffness among the different phases found in bitumen. Following the work of Loeber et al., Pauli and Grimes [43] also examined the correlation of asphaltene content with the formation of the bee structures. Their initial work was in good agreement with Loeber's work and they also reported that for some AFM devices, the laser used during the imaging process seemed to dissolve the bee structures. Subsequent work by Pauli et al. [44] demonstrated that the formation of such structures was attributed to the presence of waxes in asphalt binders. A more recent study by Allen at el. [4] also examined these bee structures. They reported an increase in the formation of bee structures with aging of the asphalt binder. They were able to use AFM indentation to measure viscoelastic creep properties for the different identifiable phases within the binder. Allen et al. [3] further developed this work and studied chemically doped asphalt binders. They also used chemical force microscopy with the AFM to study the characteristics of the microstructure with respect to the change in relative proportions of different asphalt fractions based on their polarity. Allen reported that an increase in the saturate content led to an increase in the size and concentration of bee structures at the bitumen surface. In some respects, the findings reported by Allen et al. [4] are consistent with the findings reported by Pauli et al. [44] since waxes are a subset of the saturates present in the asphalt binder. In addition, Allen et al. [3] and Pauli et al. [44] both discussed that the formation of bee structures cannot be attributed to just one factor, but rather a combination of factors and quite possibly may be the result of incompatibility of different molecular species interacting with one another. Das [9] referred to this process as phase separation and described that the mobility of the different phases found within the bitumen correlated well with the results from differential calorimetry. They concluded that the phase separation mostly occurred within the crystallization temperature range for each bitumen sample tested.

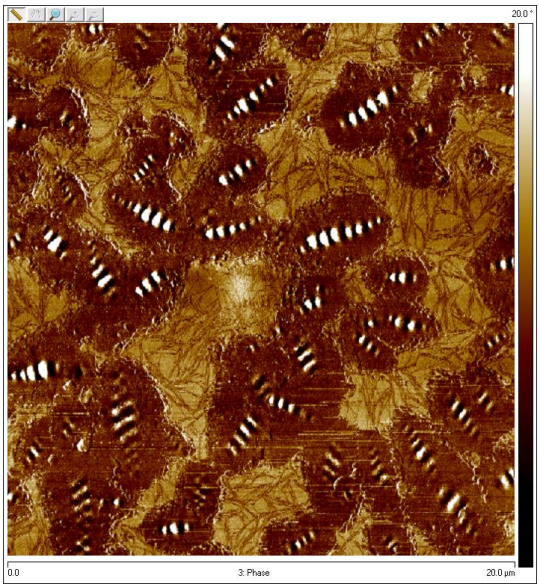

Figure 3.1: AFM phase image of VALERO PG 70-22 binder (20×20

Although there are a considerable number of publications on the formation of micro structures at the surface of the bitumen, very little research has been done on the relationship between these microstructures and failure mechanisms in the binder. Kringos et al. [24] discussed the possibility of weak interstitial zones existing between the bee phase and the surrounding phases. Kringos suggested that the composite response of the material due to loading would result in high stress regions at the boundaries of the bee structures which could serve as nucleation sites for cracking and damage assuming all regions have comparable strength. Another possible theory for crack nucleation was proposed by Allen [2]. According to Allen [2] the bee structures themselves might serve as crack nucleation sites. Based on this assumption, Allen used fracture mechanics to describe crack growth resulting from high tensile strains induced in the material. Das [9] examined damage evolution by applying thermal cycles to various bitumen samples with different chemical compositions. They proposed that an increase in wax content increased crack formation during thermal cycling of bitumen samples. All the aforementioned studies discuss various hypotheses regarding damage mech-

anisms in bitumen at a micrometer length scale. One of the main purposes of this study was to examine the role of the microstructure of bitumen on damage initiation and propagation.

3.2 Background

The overall goal of this study was to better understand the relationship between bitumen microstructure and damage evolution. As mentioned before the three main elements to achieve this goal were to-

- Observe the microstructure and measure microrheology of different domains using the AFM.
- Use the microrheology and geometry obtained using the AFM with finite element analysis to evaluate the internal stress distribution of a bitumen specimen subjected to tensile strain.
- Image a test specimen of the bitumen before and after applying a tensile strain under an AFM with the aid of a loading frame.

This section presents the background relevant to each of the aforementioned three steps. It is assumed that the reader is familiar with the basics of AFM imaging. Also, the following terminology will be used in the remainder of this paper to avoid any ambiguity. The term phase will be used to refer to the microstructural entities or domains observed using AFM phase imaging. The term "phase" is used for brevity and does not imply a different physical structure with the same chemical composition (as in the case of the traditional definition of phase). The term microstructure refers to the spatial distribution of different phases observed on the surface of the bitumen sample. The term microrheology refers to the time dependent properties of different phases.

3.2.1 Microstructure and Microrheology

The creep response of an AFM tip indenting into a soft time dependent material is a function of material properties, geometry of the indenting tip and external factors such as temperature. Galin [14] and Sneddon [51] relate the applied load to the depth of indentation for an elastic material indented using different tip geometries. Hertz also provides a solution for the indentation of elastic bodies using a spherical indenter [18, 17]. Both solutions are based on the assumption of infinitesimal strains, and a semi-infinite half space. More recent work involving nanoindentation was carried out by Fischer-Cripps [13], and Vandamme et al. [57] who provide viscoelastic solutions for creep indentation of materials exhibiting time dependent behavior. Fischer-Cripps [13] used the work of Radok and Lee [26] and Hertz to construct viscoelastic solutions for the spherical and conical indenters. These solutions are based on mechanical analog models that utilize springs and dashpots to represent viscoelastic behavior. Van Damme used Laplace transforms to obtain the time dependent solutions from Radok and Lee's linear solutions. Van Damme derived solutions for viscoelastic materials that can be represented by a 3-parameter Maxwell model, 4-parameter Kelvin-Voigt model, and 5-parameter Kelvin-Voigt-Maxwell model. Jones [22] derived a viscoelastic solution using similar method to Van Damme. This solution is not limited to mechanical analog models and can be used with any creep compliance function. Jones assumed a constant Poisson's ratio and a conical indenter for his solution.

The extent of AFM research involving the extraction or quantification of micro-scale properties of bitumen has been fairly limited. For example, Jager et al. [20] used AFM indentation and reported relative differences in stiffness values among asphalt phases. Jager et al. also stated that measuring the micro-mechanical properties of constituent phases of a bitumen is an important step in order to establish a chemo-mechanical link between the chemical composition and rheology of the bitumen. In this study, AFM imaging and indentation combined with a solution similar to the one developed by Fisher-Cripps [13] and Jones [22] was

used to determine microrheology of the bitumen samples.

3.2.2 Finite Element Analysis

The Finite Element Method (FEM) is a common tool that is used to obtain numerical solutions to problems that are difficult to analyze analytically. In the area of asphalt materials, several researchers have used this method to study the composite behavior of hot mix asphalt (HMA) [35, 31, 32, 8, 59]. X-ray tomography or other microscopy techniques such as AFM are typically used to obtain the geometry required for the finite element model. For example, Dai [8] used x-ray tomography images of hot mix asphalt samples (HMA) to develop two dimensional and three dimensional finite element models to predict viscoelastic properties such as dynamic modulus and phase angle of the hot mix asphalt composite. She simulated a uniaxial compression test using the finite element model and compared the results from the model to actual experiments performed under similar loading conditions. She found that two dimensional simulation provided reasonably accurate results, which improved with the use of three dimensional simulation. Taesun et al. [59] also used x-ray tomography to obtain a three-dimensional microstructural image of hot mix asphalt core samples. Using these three-dimensional images and a combination of viscoelastic and viscoplastic damage material models they were able to determine the composite properties of HMA samples.

In summary, several researchers have used the finite element method to evaluate local stress distributions and properties of asphalt composites as a function of the properties and spatial distribution of their constituent materials. These studies have also demonstrated that results from such computational methods compare well with experimental results. However, to best of the authors' knowledge, such studies have only been applied to the material at a millimeter or higher length scale and have not been used to evaluate the bitumen. In this study, two dimensional finite element analysis was used at a micrometer length scale to model the bitumen as a composite. The geometry of this composite was obtained using AFM imaging and material properties for different phases were obtained by AFM indentation.

3.2.3 Microscale Tensile Testing

Microscale tensile testing has been used in many fields to obtain mechanical properties of thin film specimens. Tuck et al. [56] and Paryab et al. [41] used micro-scale tensile testing to evaluate creep in thermal actuators by investigating fatigue properties of poly-silicon. Several other researchers [12, 25, 40, 36] used micro-scale tensile testing to evaluate the relaxation and creep behavior of switches made of aluminum and gold films. Sontheimer [52] used this method to address wear issues in micro-meters.

The use of microscale testing has been relatively nonexistent in the area of asphalt research. Small scale evaluation of bitumen properties has been based on the testing of thin films. For example, Marek and Herrin [30] were among the first to report the tensile behavior of bitumen thin films. They determined that film thickness and tensile strength are inversely related when the film thickness exceeds a hundred microns. Poulikakos et al. [47] performed uniaxial tensile tests on thin bitumen films at multiple temperatures in order to investigate the failure mechanism. More recently, Sultana et al. [53] demonstrated that bitumen films under a similar state of stress had similar tensile strength irrespective of film thickness.

3.3 Methodology

One of the main objectives of this paper is to determine the role of bitumen microstructure in damage evolution at a micrometer length scale. Figure 3.2 provides a visual representation of the methodology adopted for this study. Each element of this methodology is described in the following sections.

3.3.1 Materials

Bitumen samples from two different sources were selected for this study. The two selected binders were used extensively in previous research projects by the authors and several other research agencies in the USA. Specifically, one of these binders is from the materials reference library developed and used by the Asphalt Research Consortium (ARC) and des-

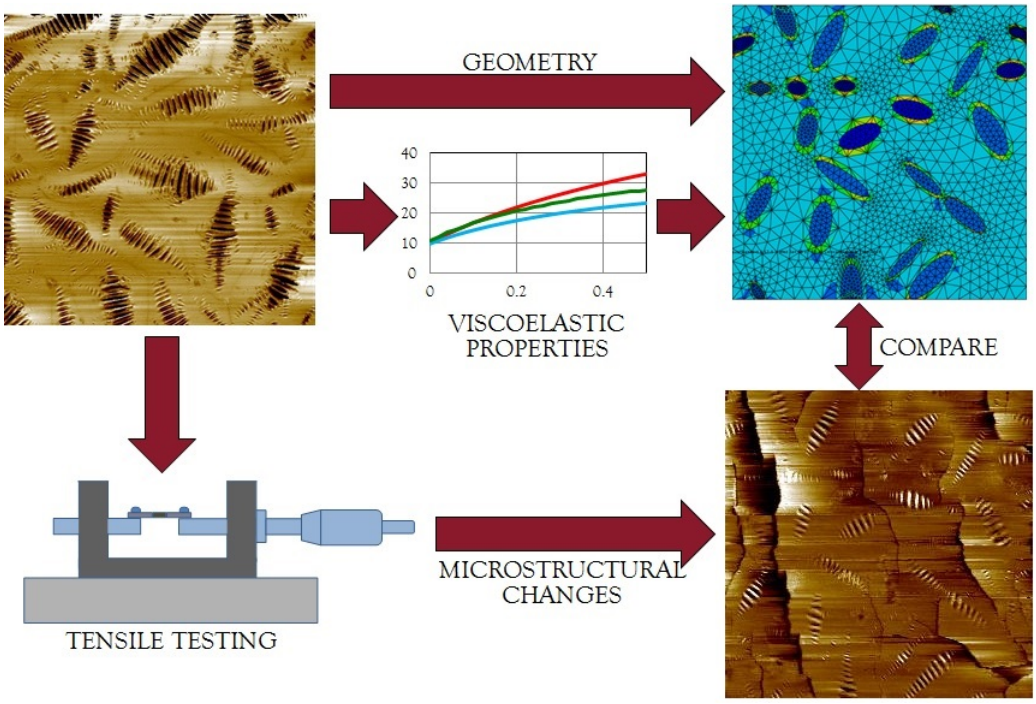

Figure 3.2: Flowchart of methodology adopted for this study

ignated as binder BI0002 in the various reports that were generated by the ARC. The other binder was from the materials reference library developed and used by the Strategic Highway Research Program (SHRP) and designated as binder AAD. In this work asphalt binder BI0002 is referred to as binder A and asphalt binder AAD is referred to as binder B. Additional information regarding these two binders can be found in Allen [2].

3.3.2 Specimen Preparation

Several studies on AFM imaging of bitumen have used spin coating to prepare thin film samples on glass substrates. This process produces a thin and homogeneous smooth surface that is ideal for AFM imaging. Although specimen preparation using spin coating is advantageous for AFM imaging, it is not known whether this process influences the microstructure of the binder compared to a hot melt specimen preparation. In order to prepare the test specimens for this study a custom made Teflon mold was fabricated. The purpose of the Teflon

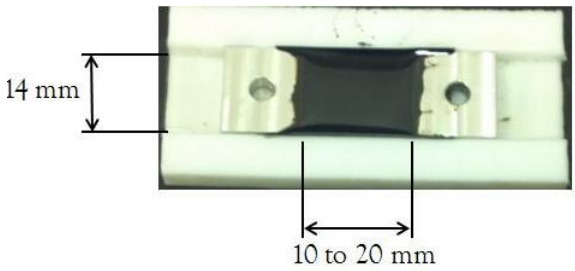

Figure 3.3: Teflon mold used to prepare asphalt binder samples

mold was to shape and support the test specimens formed to a specified thickness that could then be used in conjunction with a loading frame apparatus to study the effects of tensile loads. Figure 3.3 shows the custom designed mold used to prepare the asphalt binder test specimen for this study. The mold can be used to extend the specimen length from 10 to 20 mm, while the specimen width and thickness are fixed at 14mm and 3.5mm respectively.

The specimen preparation procedure is as follows:

- Sufficient amount of bitumen was placed into the Teflon mold and the binder was heated to 150° C, comparable to mixing temperatures for asphalt mixtures.
- The specimen was then cooled by lowering the temperature by 10° C every five minutes.
- Once the sample reached 50° C, it was maintained at that temperature for a period of 20 minutes and then allowed to cool to the ambient temperature.
- The sample was then kept in a sealed container overnight before testing was performed.

3.3.3 Microrheology Using AFM Creep Indentation

The AFM creep indentation test was used to obtain viscoelastic properties of the bitumen by generally following the work of Allen et al. [4, 2, 3]. The procedure used to obtain microrheology for different phases on the bitumen surface is briefly described below.

- Two replicate specimens for each of the two binders A and B were prepared using the heat casting method on glass slides.

- The Agilent 5400 AFM system was used to perform imaging and indentation using silicon nitride tips. The tests were carried out at room temperature (25°) . The main component of the system is a microscope, which includes the scanner, sample stage, high-resolution probe/tip and detector. Other essential equipment included a high-speed computer, an AFM controller and head electronics box (HEB), an environmental enclosure and vibration isolation stage to control vibrations, air turbulence and acoustic noise. All aspects of the AFM, including alignment, calibration and imaging were controlled by a software package called PicoView©.

- AFM imaging was used to determine the presence of different phases on the bitumen surface. A cono-spherical tip was used to image a 50 micrometer x 50 micrometer portion of the bitumen surface.

- Immediately after imaging, the AFM tip was directed to seven randomly selected points within each of the identifiable phases to perform the indentation experiment. A constant load using a voltage value of 0.2V was applied at each location while the indentation depth was recorded. The voltage was transformed into a force value by multiplying it with the deflection sensitivity and the spring constant of the cantilever used for the test.

- The results from the randomly selected points for each phase were averaged for further analyses.

A three element Voigt spring-dashpot analog model was used to model the viscoelastic behavior of the different phases observed in the bitumen (Fig. 3.4). The creep compliance for this analog model is defined as follows:

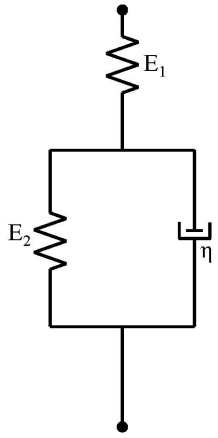

Figure 3.4: Voigt spring and dashpot viscoelastic model

$$D(t) = \left[\frac{1}{E_1} + \frac{1}{E_2}(1 - e^{-tE_2/\eta})\right] \tag{3.1}$$

where, $D(t)$ is the creep compliance, E_1 is the instantaneous modulus, E_2 and η are time dependent parameters. The data from the indentation tests were used to determine the instantaneous modulus and the time dependent parameters for each of the identifiable phases for each bitumen specimen.

3.3.4 Finite Element Analysis

In order to study the composite effect of individual phases present within the asphalt binder a finite element model was developed for each of the two binders. The phase images obtained using the AFM were used as geometry inputs for the finite element model. Figures 3.5 and 3.6 show the finite element meshes along with the corresponding AFM phase images. The "bee" phases are highlighted in green, the "bee casing" regions are highlighted in red, and the "interstitial" regions are highlighted in light blue in fig. 3.5 and 3.6.

The measurements obtained using the AFM indentation tests were used as the material

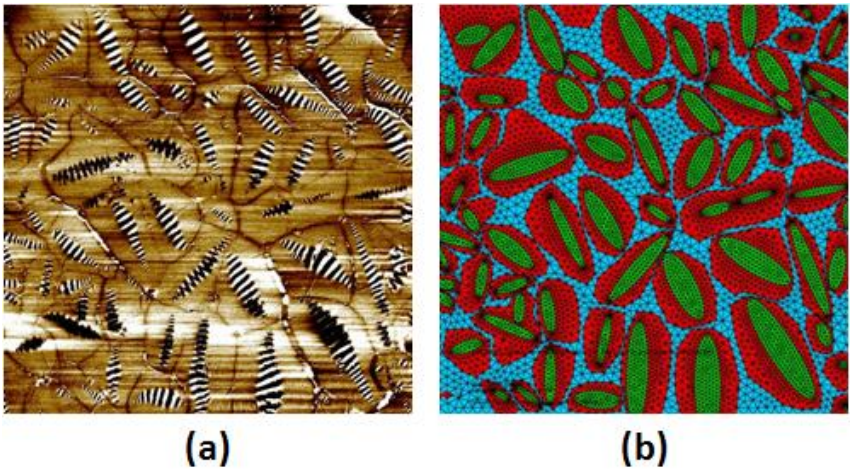

Figure 3.5: (a) AFM phase image and (b) Finite element mesh of asphalt binder A (50x50 microns^2)

property inputs for the finite element model. More specifically, the Abaqus finite element software used in this study requires a Prony series stress relaxation function to model the viscoelastic response. The expression is given by:

$$g(t) = 1 - \sum_{i=1}^{n} g_i(1 - exp(-t/\tau_i)) \tag{3.2}$$

where, $g(t) = G(t)/G_0$ is a non-dimensional shear relaxation modulus. The terms g_i and τ are the time dependent Prony series parameters, and g_i is calculated based on G_0 and G_n (time dependent Prony series shear modulus parameter). $G(t)$ is the time dependent shear relaxation modulus of the specimen, and G_0 is the instantaneous shear modulus of the specimen, which is calculated internally by using the specified Young's Modulus E and the Poisson's ratio μ of the material. With the use of Laplace transformation, the creep compliance function given by the Voigt spring-dasphot analog model was transformed to a one term Prony series required for Abaqus implementation. The finite element simulation entailed the application of a strain of 10% being held for a duration of 4 seconds.

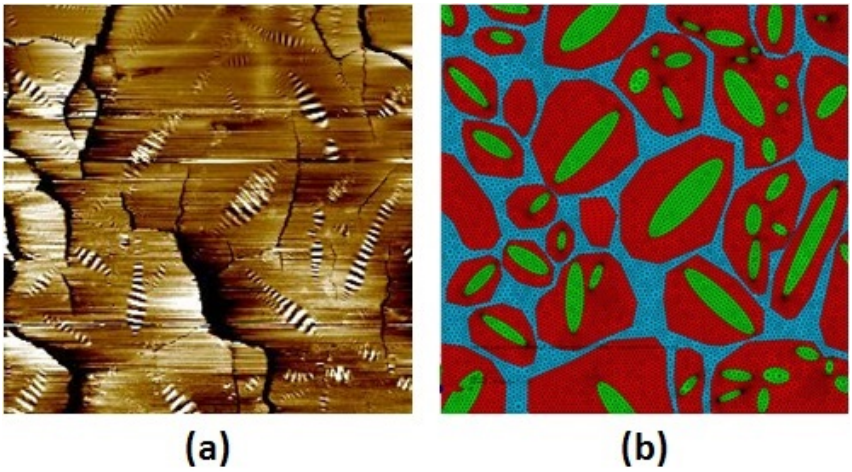

Figure 3.6: (a) AFM phase image and (b) Finite element mesh of asphalt binder B (50x50 microns^2)

3.3.5 Loading Frame Setup

In order to examine the effect of applied load/displacement on the microstructure of asphalt binder a loading frame was designed to precisely apply tensile displacement to the test specimen. Due to the sensitivity of the AFM to electrical noise the device was designed to be manually driven using a micrometer drive. Figure 3.7 is a schematic of the loading frame. Axial displacement of the non-rotating spindle was achieved using a micrometer drive with precision of 0.0001 mm. The specimen is held between two metal plates that are screwed onto the fixed spindle and the micrometer spindle allowing it to translate along the spindle axis. The spindles are held onto the base plate using a metallic U-frame. Figure 3.8 shows the final prototype of the loading frame that was used to carry out the experiments.

Once the specimen was prepared it was attached to the loading frame using the screws on the metallic fixture plates. The experimental procedure used to study the effect of tensile displacement on the microstructure is described as follows:

- The initial length of the specimen was measured using a vernier caliper. Using this measurement the amount of displacement that was to be applied in order to obtain 1%

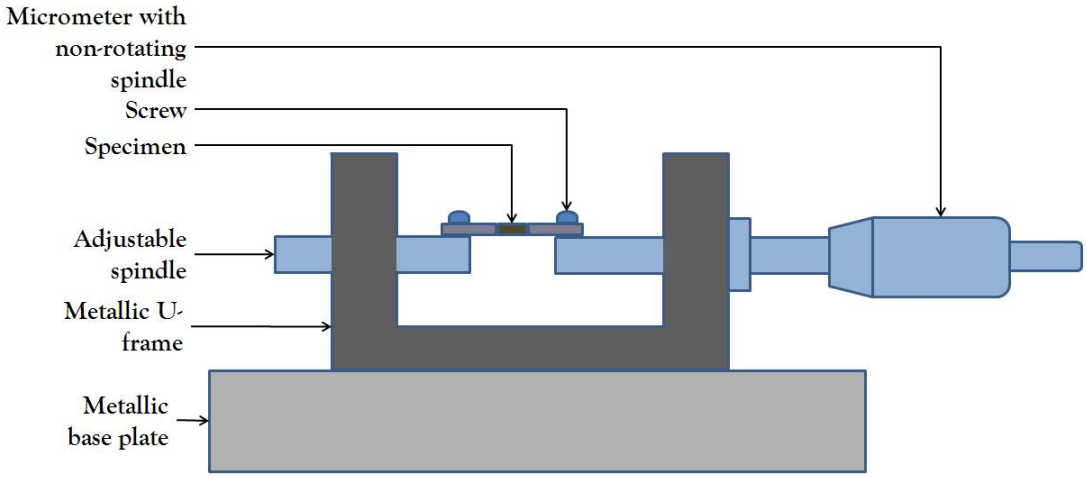

Figure 3.7: Micro-loading frame design

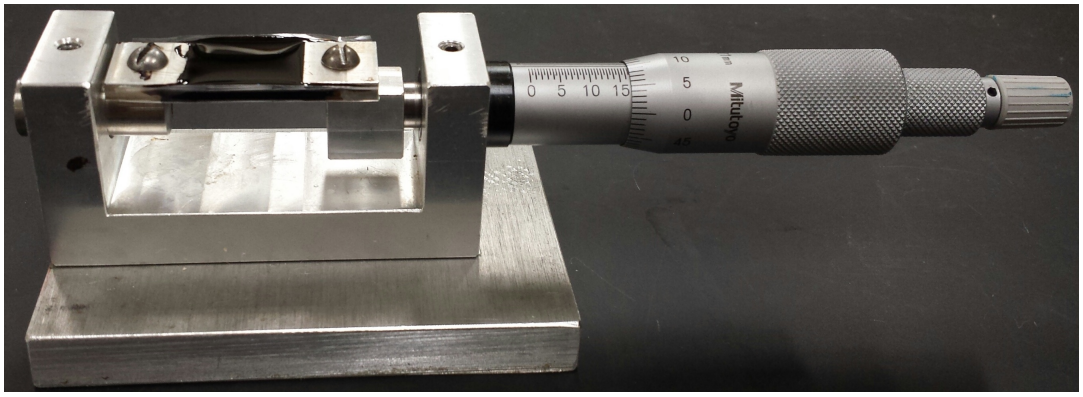

Figure 3.8: Micro-loading frame final prototype

and 5% strain was calculated.

- Once the sample was mounted on the loading frame it was allowed to rest for ten minutes to allow the binder to relieve any stresses that may have built up during the mounting of the specimen.

- The sample was then imaged using AFM phase imaging in its initial condition without any load being applied.

- The amount of displacement necessary to obtain 1% tensile strain was then applied. The specimen was allowed to relax for a period of five minutes in order for it to reach a steady state condition. The specimen was then re-imaged to obtain the microstructure after deformation.

- Each time a minimum of five 50x50 microns^2 images were obtained.

- This process was repeated and AFM images of binder microstructure were obtained after 1% and 5% applied tensile strain.

3.4 Results

3.4.1 AFM Creep Indentation Results

Using the creep indentation technique discussed in the methodology section, viscoelastic properties for the "bee" phase, the "bee casing" phase, and the "interstitial" phase were obtained. Figures 3.9 and 3.10 show the creep indentation response of different phases in bitumens A and B. The applied constant load was calculated to be approximately one micronewton. The load was applied for a period of four seconds and the indentation response was fit to a conical Sneddon viscoelastic solution in order to obtain the viscoelastic creep compliance parameters for each phase. Table 3.1 summarizes these results.

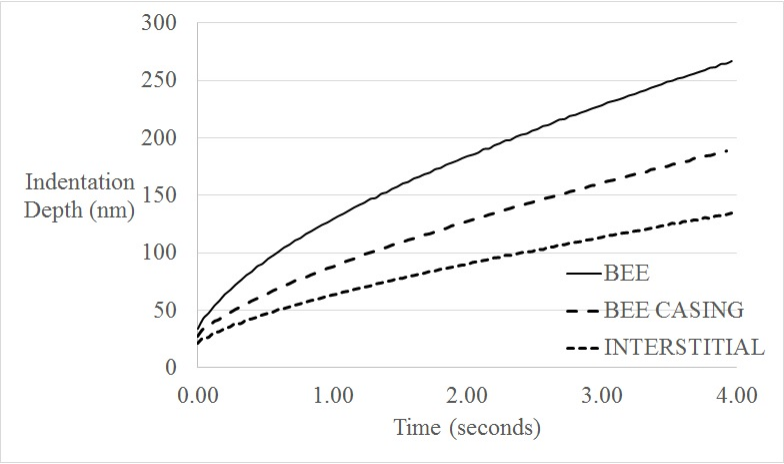

Figure 3.9: Viscoelastic creep indentation response of asphalt binder BI0002 Unaged

Table 3.1: AFM creep indentation analysis of asphalt binder A and B

Binder	Parameter (unit)	Bee	Bee Casing	Interstitial
A	E1 (Pa)	2.66E+09	4.12E+09	5.25E+09
A	E2 (Pa)	2.00E+04	9.00E+05	9.00E+06
A	eta (Pa.s)	1.79E+08	3.52E+08	8.02E+08
B	E1 (Pa)	1.75E+09	2.53E+09	4.35E+09
B	E2 (Pa)	5.00E+04	8.00E+04	9.00E+04
B	eta (Pa.s)	2.43E+07	1.32E+08	6.82E+07

3.4.2 Results from the Finite Element Analysis

Figures 3.11 (a) and (b) show the von Mises stress contours for finite element simulations of stress relaxation experiments performed on binders (a) A and (b) B. The highest stresses were observed in the interstitial phase and the lowest stresses were observed in the bee phase. The bee casing phase exhibits an intermediate level of stresses compared to the other phases. Figure 3.12 (a) and (b) show the internal distribution of tensile strains experienced by both binders. The contours here show that the bee regions experience the highest local tensile strains while the interstitial zones experience the lowest amount of local tensile strains which

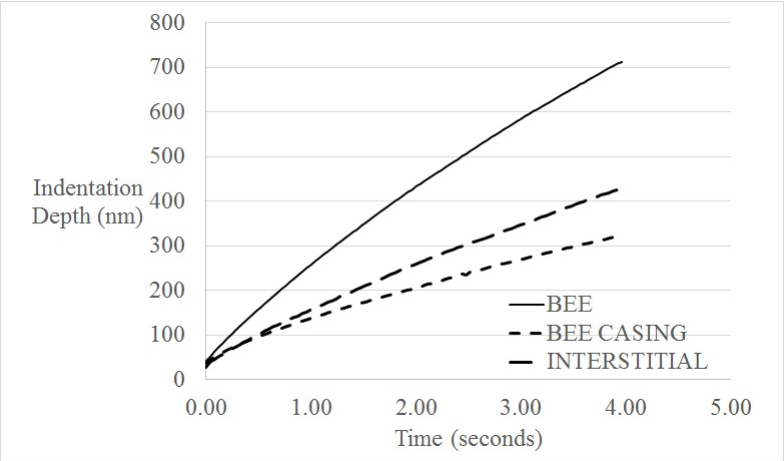

Figure 3.10: Viscoelastic creep indentation response of asphalt binder AAD Unaged

is consistent with the results shown in figure 3.11 (a) and (b).

Table 3.2 shows the maximum and minimum von Mises, and tensile strain values for both binders based on the FEM simulations. The maximum stress for binders A and B are approximately 2.5 and 3.5 times the minimum stress, respectively.

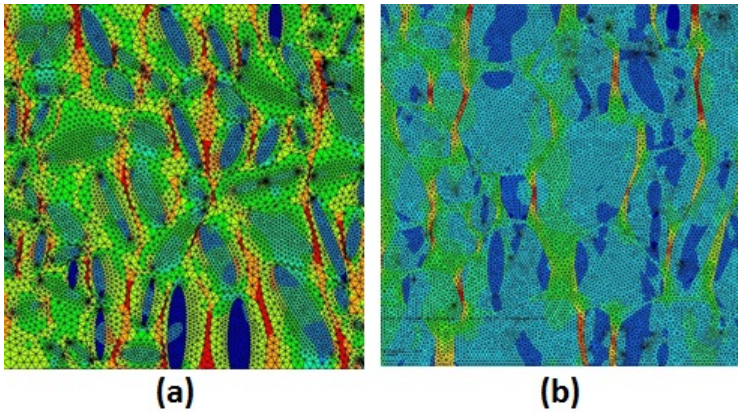

Figure 3.11: Von mises stress contours for finite element simulations of asphalt binders (a) A and (b) B (50x50 microns^2)

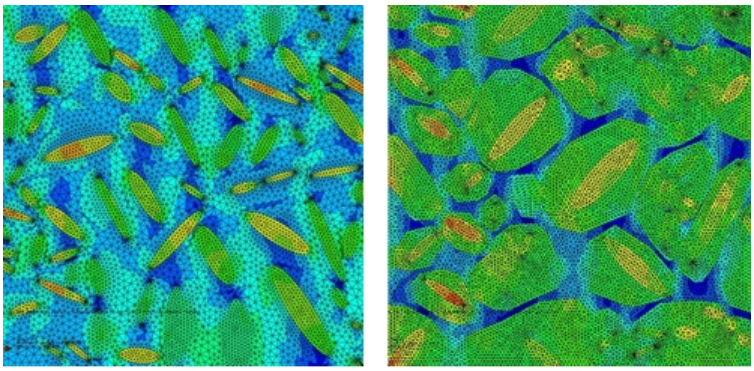

Figure 3.12: Tensile strain contours for finite element simulations of asphalt binders (a) A and (b) B (50x50 microns^2)

Table 3.2: Finite element results of stress relaxation simulation of asphalt binders A and B

BINDER	MAX TENSILE STRAIN	MIN TENSILE STRAIN	MAX VON MISES STRESS	MIN VON MISES STRESS
A	0.169	0.0613	0.628 GPa	0.258 GPa
B	0.194	0.0503	0.558 GPa	0.167 GPa

3.4.3 AFM Imaging Before and After Load Application

Three distinct phases were observed in the AFM images of each of the two binders (Figure 3.13). The first phase can be described as the "bee" phase, a second phase that surrounds the "bee" phase referred to as the "bee casing" phase, and a third phase referred to as the "interstitial phase" that occupies the space between the bee casing. The interstitial phase is not clearly visible without image enhancement and has been highlighted for the convenience of the reader in figure 3.14 .

Figure 3.15 shows AFM phase images of binders A and B after the application of one percent strain. Both test specimens show clear signs of load induced phase separation (LIPS). It is also evident from the microstructural changes in the images that the LIPS occurs around

the bee casing phases and go through the interstitial zones. Figure 3.16 shows AFM phase images of binders A and B after five percent strain. Microstructural changes observed here are consistent with that of figure 3.15. Here the LIPS zones are more prominent.

Figure 3.13: AFM phase image showing microstructural features of asphalt binder (a) AAD and (b) BI0002 (50x50 microns^2)

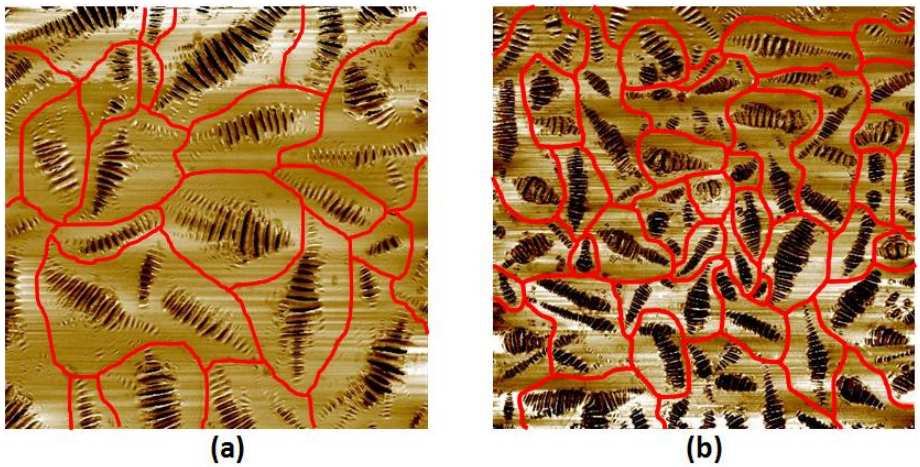

Figure 3.14: AFM phase image showing interstitial phase of asphalt binder (a) AAD and (b) BI0002 (50x50 microns^2)

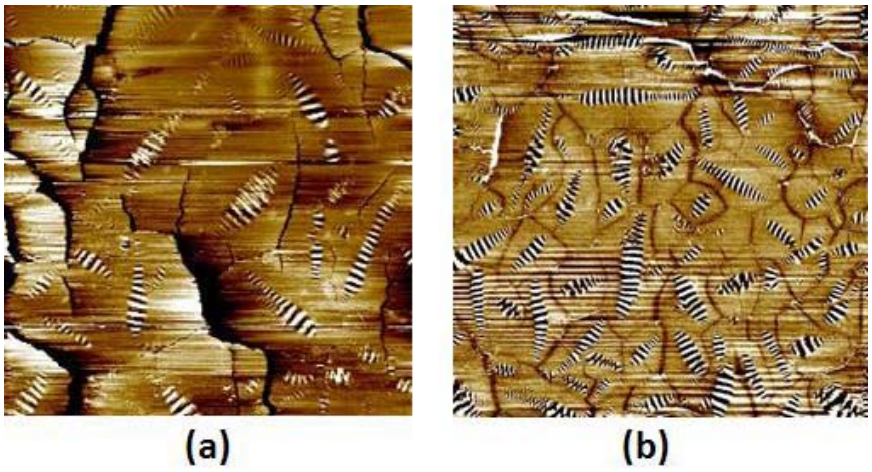

Figure 3.15: AFM phase image showing microstructural features of asphalt binder (a) AAD and (b) BI0002 (50x50 microns^2) after 1% strain

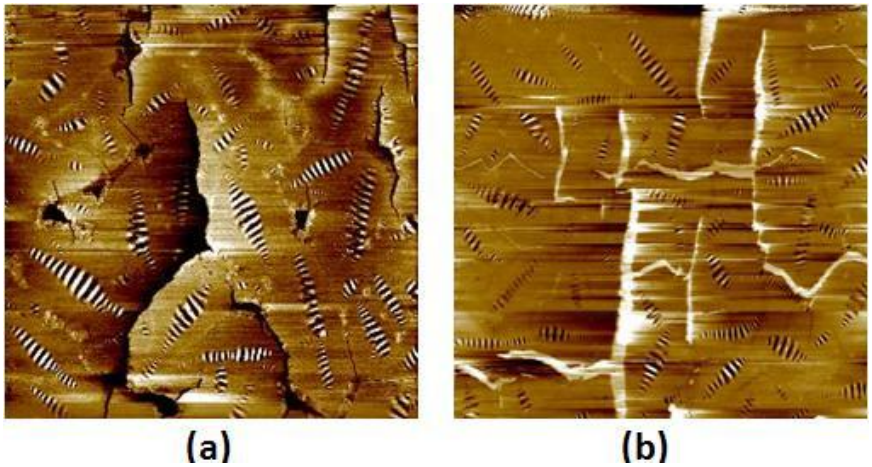

Figure 3.16: AFM phase image showing microstructural features of asphalt binder (a) AAD and (b) BI0002 (50x50 microns^2) after 5% strain

In order to quantitatively assess the changes in the microstructure due to the applied tensile strain we employed image analysis techniques using the open source image analysis tool ImageJ. Various geometric attributes were obtained and a comparison of these attributes was

done before and after strain was applied to the test specimens. Due to phase separation and changes that occurred in the bee casing and interstitial phases, comparisons here are only made on the basis of the discrete bee phase. Table 3.3 compares the distribution of the bee structures before and after load is applied to binders A and B.

Table 3.3: Microstructural analysis of asphalt binder A and B

STRAIN LEVEL	TOTAL COUNT	MEAN AREA (μm^2)	%Area
before (binder A)	743	2.93	21.39
one percent (binder A)	586	2.99	17.07
five percent (binder A)	490	2.61	12.35
before (binder B)	369	5.40	19.58
one percent (binder B)	317	5.29	16.26
five percent (binder B)	272	3.21	8.69

3.5 Discussion

3.5.1 Microrheology

A creep AFM indentation technique was used to obtain the micro-rheology of the three different phases observed in each binder (Figures 3.10 and 3.9). The indentation response for a similar phase was distinctly different for each binder; this would be expected given that the two binders were from very different sources and had different chemical composition and mechanical properties. The rank order of instantaneous modulus for each of the three phases was similar for both binders. The bee phase had the lowest while the interstitial phase had the highest magnitude of instantaneous modulus. The time dependent response showed a slightly

different trend for binder A compared to binder B. Although the interstitial phase was determined to be the least compliant for binder A, it showed an intermediate level of compliance compared to the two other phases for binder B. Dourado et al. [10] and Allen et al. [4] reported similar trends between the bee and the surrounding phases using similar indentation techniques. The findings from this study and the studies of Dourado et al. [10] and Allen et al. [4] strongly suggest that the mechanical properties of the different phases are substantially different. A corollary to this observation is that stress localization is likely to occur within the bitumen when subjected to external loads. Such localization will be a function of the rheology and geometric distribution of phases. However, further work is needed to determine whether there exists any consistent relationship between different structural features and rank order of stiffness.

Note that the authors recognize that the properties obtained for different phases through such microrheological measurements and analyses are not absolute properties. For example, the properties are obtained by surface indentation and as such the material structure beneath the surface even for a thick melt specimen will influence the results obtained. Similarly, the indentation using a conospherical tip is not the same as one dimensional uniaxial loading. However, despite these biases, the measured microrheology does show substantial and consistent differences in mechanical properties of the different phases. While such measurements may not be perfect, they are nonetheless a good semi-quantitative representation of the properties of different phases within the binder.

3.5.2 Finite Element Analysis

Figures 3.11 (a) and (b) illustrate the internal distribution of the von Mises stress in both binders undergoing stress relaxation over a period of four seconds. As expected, the highest level of stress was found within the interstitial and bee casing phases while the bee phase experienced the lowest level of stress. This suggests that the interstitial or the bee casing phases are the most likely to experience damage once the specimen is loaded. One of the

more interesting observations from these analyses was that the local stress amplification for binder A (ratio of the highest to lowest local stress) was much lower in magnitude compared to the stress amplification in binder B. Also, both binders A and B had a similar percentage of area occupied by the bee structures (approximately 20%). However, binder A had a higher number of bee structures with a smaller mean size compared to binder B, which had fewer bee structures with a larger mean size. We speculate that the dispersed nature of these bee structures in binder A results in a more homogenous stress distribution and consequently lower stress amplification.

3.5.3 The Effect of Tensile Strain on Microstructure

A comparison of images before and after applying 1% tensile strain (e.g. Figure 3.15) clearly shows the formation of a crack like network notably between the bee structures. The term "crack like" is emphasized here because the experimental work in this area is premature to conclude that there features are indeed cracks in the conventional sense, wherein a new surface is formed. Instead these features may be more appropriately referred to as the change in phase or morphology due to the action of load or simply load induced phase separation (LIPS). It is speculated that these LIPS zones are the precursor to conventional forms of damage. Another notable feature of the LIPS zone is that these occur predominantly in areas in between the bee casings or the "interstitial spaces" as described previously. In fact, based on the microrheology measurements and finite element analyses the regions that correspond to the LIPS zones are also the regions that correspond to higher stress amplification (discussed in section 5.2)

The second observation from these experiments is that the LIPS zones occur most likely at the expense of the bee-structures. In other words, the tensile strain not only resulted in the formation of the LIPS zones but also the disintegration of the bee structures that possibly were in the proximity of these zones. This is further supported by the quantitative analysis of these structures using ImageJ before and after the application of the tensile strains. Binders A and B

had approximately 21% and 14% reduction in the number of bee structures, respectively after the application of 1% strain. The area occupied by these bee structures was approximately 3-4% less of the total surface after 1% applied strain. Also, the smaller bee structures most likely were the first to completely dissipate due to the tensile displacement experienced. The larger bee structures were only partially dissipated since the amount of the strain applied may not have been large enough in magnitude to cause complete dissipation of the larger area taken up by the larger sized features.

In summary, the numerical simulations verify that differences in mechanical properties among the different phases lead to stress localization. In the finite element simulations we can clearly see that the highest stresses occur in the bee casing and interstitial phases. The formation of the LIPS zones or crack like networks correlates well to the locations where highest levels of stresses occurred in the finite element simulations. This verifies that the differences in material properties most likely lead to high levels of localized stresses that lead to damage initiation in the interstitial and the bee casing phases.

3.6 Conclusions

The objective of this study was to evaluate the inter-relationship of tensile load, damage nucleation and microstructure of the bitumen. A combination of AFM imaging and creep indentation measurements were used to obtain geometry and microrheology of the phases observed on the bitumen surface. This information was used with the finite element method to examine the internal stresses in the binder and potential evolution of damage. The following conclusions are drawn from the study:

- AFM phase imaging revealed three different phases for each of the two binders studied. AFM indentation was used to semi-quantitatively evaluate of the rheology of these phases for a given bitumen, referred to as microrheology. Results clearly show that the compliance of different phases within a bitumen are substantially different. In other

words, viscoelastic properties obtained through AFM creep indentation experiments show material inhomogeneity exists within the bitumen at a micrometer length scale.

- The composite finite element simulations show that the differences in properties of the different phases result in high levels of localized stress or stress amplification within the interstitial zones. The stress amplification was higher for the binder with larger but fewer bee structures compared to the binder with smaller but more bee structures.

- The application of tensile load or displacement causes cracks or phase separation zones to appear which are referred to as LIPS zones.

- The high stress regions observed from the finite element simulation coincide with the areas within which the LIPS zones form. This suggests that material inhomogeneity leads to the development of high stresses within interstitial zones which leads to damage nucleation and propagation.

The above conclusions suggest that the ability to manipulate the microstructure of bitumen (e.g. using chemical or other modifiers) has a significant influence on the durability and inherent ability of the bitumen to resist damage. Further work is required to (i) more accurately characterize the microrheology of bitumen, (ii) more accurately and quantitatively assess the relationship between damage evolution in the bitumen and its microstructure, and (iii) establish a better understanding of the relationship between the chemical composition of the bitumen and its microstructure.

4. A STUDY OF THE EVOLUTION OF ASPHALT BINDER MICROSTRUCTURE DUE TO AGING AND TENSILE LOADING

4.1 Introduction

The study of the physical properties of asphalt binder or bitumen is motivated by economic implications. Due to the significant rise in bitumen prices over the last few decades, engineering of modified binders with enhanced properties has become one of the main focuses of the asphalt industry. In order to engineer binders that can deliver improved field performance with longer durability, a better understanding of the complex mechanisms that drive the degradation of binder properties is necessary. Technological advancement in the field of microscopy has greatly facilitated this aspect of asphalt research. The development of experimental techniques such as atomic force microscopy (AFM), scanning electron microscopy (SEM), and X-ray tomography has allowed researchers to examine bitumen and asphalt mixtures at a much smaller scale [4, 2, 28, 44, 20, 33, 34, 42]. These techniques have led to an improved understanding of the link between the microstructure of the bitumen (or bitumen-aggregate composite) and the resulting mechanical processes during loading that lead to distresses such as fatigue damage and cracking.

During the last few decades the ability to examine bitumen using an AFM has resulted in considerable improvements in the understanding of the bitumen microstructure and behavior. Techniques for using the AFM to investigate the bitumen microstructure have also significantly improved during this time. Loeber et al. [28, 27] were among the first to report the existence of so called "bee" structures with an oblong shaped outline and rippled topography (see figure 4.1). They reported an increase in these "bee" structures with an increase in asphaltene content. Jager et al. [20] and Tarefder et al. [54] were able to use AFM indentation and nanoindentation, respectively, to measure the differences in stiffness among the

different phases found in bitumen. Following the work of Loeber et al., Pauli and Grimes [43] also examined the correlation of asphaltene content with the formation of the bee structures. Their initial work was in good agreement with Loeber's work and they also reported that for some AFM devices, the laser used during the imaging process seemed to dissolve the bee structures. Subsequent work by Pauli et al. [44] demonstrated that the formation of such structures was attributed to the presence of waxes in asphalt binders. A more recent study by Allen at el. [4] also examined these bee structures. They reported an increase in the formation of bee structures with aging of the asphalt binder. They were able to use AFM indentation to measure viscoelastic creep properties for the different identifiable phases within the binder. Allen et al. [3] further developed this work and studied chemically doped asphalt binders. They also used chemical force microscopy with the AFM to study the characteristics of the microstructure with respect to the change in relative proportions of different asphalt fractions based on their polarity. Allen reported that an increase in the saturate content led to an increase in the size and concentration of bee structures at the bitumen surface. In some respects, the findings reported by Allen et al. [4] are consistent with the findings reported by Pauli et al. [44] since waxes are a subset of the saturates present in the asphalt binder. In addition, Allen et al. [3] and Pauli et al. [44] both discussed that the formation of bee structures cannot be attributed to just one factor, but rather a combination of factors and quite possibly may be the result of incompatibility of different molecular species interacting with one another. Das [9] referred to this process as phase separation and described that the mobility of the different phases found within the bitumen correlated well with the results from differential calorimetry. They concluded that the phase separation mostly occurred within the crystallization temperature range for each bitumen sample tested.

Although there are a considerable number of publications on the formation of micro structures at the surface of the bitumen, very little research has been done on the relationship between these microstructures and failure mechanisms in the binder. Kringos et al.

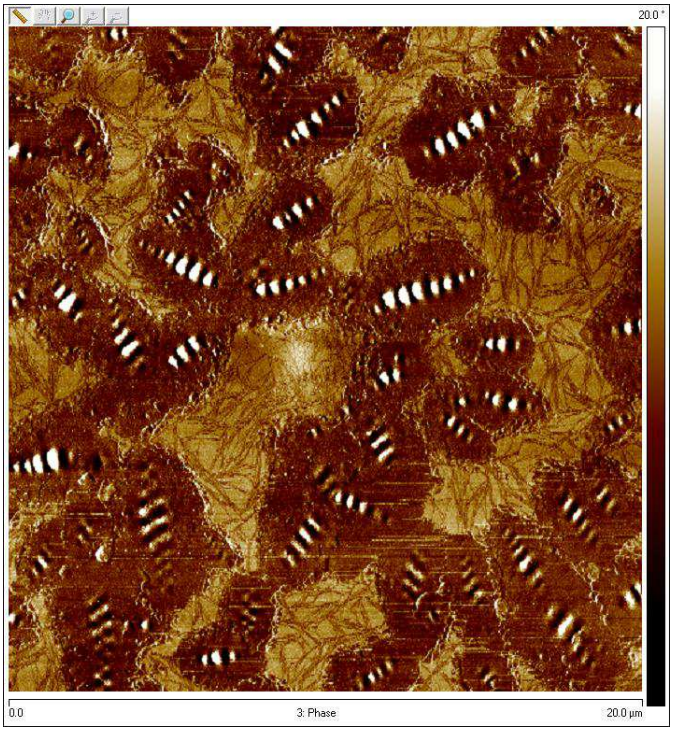

Figure 4.1: AFM phase image of VALERO PG 70-22 binder (20×20

[24] discussed the possibility of weak interstitial zones existing between the bee phase and the surrounding phases. Kringos suggested that the composite response of the material due to loading would result in high stress regions at the boundaries of the bee structures which could serve as nucleation sites for cracking and damage assuming all regions have comparable strength. Another possible theory for crack nucleation was proposed by Allen [2]. According to Allen [2] the bee structures themselves might serve as crack nucleation sites. Based on this assumption, Allen used fracture mechanics to describe crack growth resulting from high tensile strains induced in the material. Das [9] examined damage evolution by applying thermal cycles to various bitumen samples with different chemical compositions. They proposed that an increase in wax content increased crack formation during thermal cycling of bitumen samples. All the aforementioned studies discuss various hypotheses regarding damage mechanisms in bitumen at a micrometer length scale. One of the main purposes of this study was

to examine the role of the microstructure of bitumen on damage initiation and propagation.

4.2 Background

The overall goal of this study was to better understand the relationship between bitumen microstructure and damage evolution. As mentioned before the three main elements to achieve this goal were to-

- Observe the microstructure and measure microrheology of different domains using the AFM.
- Use the microrheology and geometry obtained using the AFM with FE analysis to evaluate the internal stress distribution of a bitumen specimen subjected to tensile strain.
- Image a test specimen of the bitumen before and after applying a tensile strain under an AFM with the aid of a loading frame.

This section presents the background relevant to each of the aforementioned three steps. It is assumed that the reader is familiar with the basics of AFM imaging. Also, the following terminology will be used in the remainder of this paper to avoid any ambiguity. The term phase will be used to refer to the microstructural entities or domains observed using AFM phase imaging. The term "phase" is used for brevity and does not imply a different physical structure with the same chemical composition (as in the case of the traditional definition of phase). The term microstructure refers to the spatial distribution of different phases observed on the surface of the bitumen sample. The term microrheology refers to the time dependent properties of different phases.

4.2.1 Microstructure and Microrheology

The creep response of an AFM tip indenting into a soft time dependent material is a function of material properties, geometry of the indenting tip and external factors such as temperature. Galin [14] and Sneddon [51] relate the applied load to the depth of indentation

for an elastic material indented using different tip geometries. Hertz also provides a solution for the indentation of elastic bodies using a spherical indenter [18, 17]. Both solutions are based on the assumption of infinitesimal strains, and a semi-infinite half space. More recent work involving nanoindentation was carried out by Fischer-Cripps [13], and Vandamme et al. [57] who provide viscoelastic solutions for creep indentation of materials exhibiting time dependent behavior. Fischer-Cripps [13] used the work of Radok and Lee [26] and Hertz to construct viscoelastic solutions for the spherical and conical indenters. These solutions are based on mechanical analog models that utilize springs and dashpots to represent viscoelastic behavior. Van Damme used Laplace transforms to obtain the time dependent solutions from Radok and Lee's linear solutions. Van Damme derived solutions for viscoelastic materials that can be represented by a 3-parameter Maxwell model, 4-parameter Kelvin-Voigt model, and 5-parameter Kelvin-Voigt-Maxwell model. Jones [22] derived a viscoelastic solution using similar method to Van Damme. This solution is not limited to mechanical analog models and can be used with any creep compliance function. Jones assumed a constant Poisson's ratio and a conical indenter for his solution.

The extent of AFM research involving the extraction or quantification of micro-scale properties of bitumen has been fairly limited. For example, Jager et al. [20] used AFM indentation and reported relative differences in stiffness values among asphalt phases. Jager et al. also stated that measuring the micro-mechanical properties of constituent phases of a bitumen is an important step in order to establish a chemo-mechanical link between the chemical composition and rheology of the bitumen. In this study, AFM imaging and indentation combined with a solution similar to the one developed by Fisher-Cripps [13] and Jones [22] was used to determine microrheology of the bitumen samples.

4.2.2 Finite Element Analysis

The Finite Element Method (FEM) is a common tool that is used to obtain numerical solutions to problems that are difficult to analyze analytically. In the area of asphalt mate-

rials, several researchers have used this method to study the composite behavior of hot mix asphalt (HMA) [35, 31, 32, 8, 59]. X-ray tomography or other microscopy techniques such as AFM are typically used to obtain the geometry required for the FE model. For example, Dai [8] used x-ray tomography images of hot mix asphalt samples (HMA) to develop two dimensional and three dimensional FE models to predict viscoelastic properties such as dynamic modulus and phase angle of the hot mix asphalt composite. She simulated a uniaxial compression test using the FE model and compared the results from the model to actual experiments performed under similar loading conditions. She found that two dimensional simulation provided reasonably accurate results, which improved with the use of three dimensional simulation. Taesun et al. [59] also used x-ray tomography to obtain a three-dimensional microstructural image of hot mix asphalt core samples. Using these three-dimensional images and a combination of viscoelastic and viscoplastic damage material models they were able to determine the composite properties of HMA samples.

In summary, several researchers have used the FE method to evaluate local stress distributions and properties of asphalt composites as a function of the properties and spatial distribution of their constituent materials. These studies have also demonstrated that results from such computational methods compare well with experimental results. However, to best of the authors' knowledge, such studies have only been applied to the material at a millimeter or higher length scale and have not been used to evaluate the bitumen. In this study, two dimensional FE analysis was used at a micrometer length scale to model the bitumen as a composite. The geometry of this composite was obtained using AFM imaging and material properties for different phases were obtained by AFM indentation.

4.2.3 Microscale Tensile Testing

Microscale tensile testing has been used in many fields to obtain mechanical properties of thin film specimens. Tuck et al. [56] and Paryab et al. [41] used micro-scale tensile testing to evaluate creep in thermal actuators by investigating fatigue properties of poly-silicon. Several

other researchers [12, 25, 40, 36] used micro-scale tensile testing to evaluate the relaxation and creep behavior of switches made of aluminum and gold films. Sontheimer [52] used this method to address wear issues in micro-meters.

The use of microscale testing has been relatively nonexistent in the area of asphalt research. Small scale evaluation of bitumen properties has been based on the testing of thin films. For example, Marek and Herrin [30] were among the first to report the tensile behavior of bitumen thin films. They determined that film thickness and tensile strength are inversely related when the film thickness exceeds a hundred microns. Poulikakos et al. [47] performed uniaxial tensile tests on thin bitumen films at multiple temperatures in order to investigate the failure mechanism. More recently, Sultana et al. [53] demonstrated that bitumen films under a similar state of stress had similar tensile strength irrespective of film thickness.

4.3 Methodology

One of the main objectives of this paper is to determine the role of bitumen microstructure in damage evolution at a micrometer length scale. Figure 4.2 provides a visual representation of the methodology adopted for this study. Each element of this methodology is described in the following sections.

4.3.1 Materials

Bitumen samples from two different sources were selected for this study. The two selected binders were used extensively in previous research projects by the authors and several other research agencies in the USA. Specifically, one of these binders is from the materials reference library developed and used by the Asphalt Research Consortium (ARC) and designated as binder BI0002 in the various reports that were generated by the ARC. The other binder was from the materials reference library developed and used by the Strategic Highway Research Program (SHRP) and designated as binder AAD. In this work asphalt binder BI0002 is referred to as binder A and asphalt binder AAD is referred to as binder B. Addi-

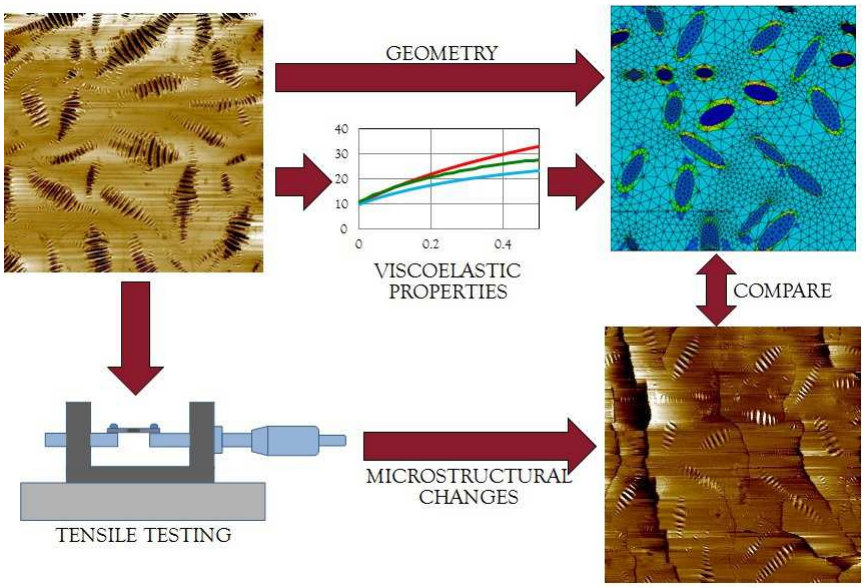

Figure 4.2: Flowchart of methodology adopted for this study

tional information regarding these two binders can be found in Allen [2].

4.3.2 Specimen Preparation

Several studies on AFM imaging of bitumen have used spin coating to prepare thin film samples on glass substrates. This process produces a thin and homogeneous smooth surface that is ideal for AFM imaging. Although specimen preparation using spin coating is advantageous for AFM imaging, it is not known whether this process influences the microstructure of the binder compared to a hot melt specimen preparation. In order to prepare the test specimens for this study a custom made Teflon mold was fabricated. The purpose of the Teflon mold was to shape and support the test specimens formed to a specified thickness that could then be used in conjunction with a loading frame apparatus to study the effects of tensile loads. Figure 4.3 shows the custom designed mold used to prepare the asphalt binder test specimen for this study. The mold can be used to extend the specimen length from 10 to 20 mm, while the specimen width and thickness are fixed at 14mm and 3.5mm respectively.

The specimen preparation procedure is as follows:

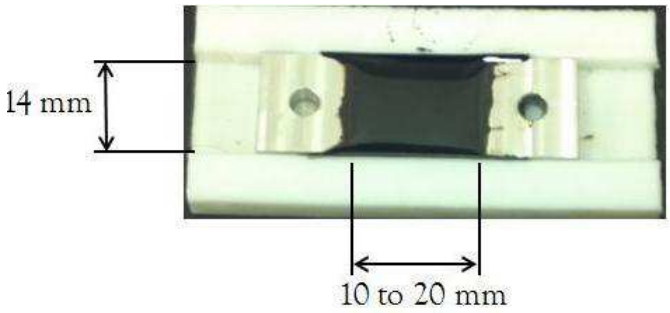

Figure 4.3: Teflon mold used to prepare asphalt binder samples

- Sufficient amount of bitumen was placed into the Teflon mold and the binder was heated to 150° C, comparable to mixing temperatures for asphalt mixtures.
- The specimen was then cooled by lowering the temperature by 10° C every five minutes.
- Once the sample reached 50° C, it was maintained at that temperature for a period of 20 minutes and then allowed to cool to the ambient temperature.
- The sample was then kept in a sealed container overnight before testing was performed.

4.3.3 Microrheology Using AFM Creep Indentation

The AFM creep indentation test was used to obtain viscoelastic properties of the bitumen by generally following the work of Allen et al. [4, 2, 3]. The procedure used to obtain microrheology for different phases on the bitumen surface is briefly described below.

- Two replicate specimens for each of the two binders A and B were prepared using the heat casting method on glass slides.
- The Agilent 5400 AFM system was used to perform imaging and indentation using silicon nitride tips. The tests were carried out at room temperature (25°) . The main component of the system is a microscope, which includes the scanner, sample stage,

high-resolution probe/tip and detector. Other essential equipment included a high-speed computer, an AFM controller and head electronics box (HEB), an environmental enclosure and vibration isolation stage to control vibrations, air turbulence and acoustic noise. All aspects of the AFM, including alignment, calibration and imaging were controlled by a software package called PicoView©.

- AFM imaging was used to determine the presence of different phases on the bitumen surface. A cono-spherical tip was used to image a 50 micrometer x 50 micrometer portion of the bitumen surface.

- Immediately after imaging, the AFM tip was directed to seven randomly selected points within each of the identifiable phases to perform the indentation experiment. A constant load using a voltage value of 0.2V was applied at each location while the indentation depth was recorded. The voltage was transformed into a force value by multiplying it with the deflection sensitivity and the spring constant of the cantilever used for the test.

- The results from the randomly selected points for each phase were averaged for further analyses.

A three element Voigt spring-dashpot analog model was used to model the viscoelastic behavior of the different phases observed in the bitumen (Fig. 4.4). The creep compliance for this analog model is defined as follows:

$$D(t) = \left[\frac{1}{E_1} + \frac{1}{E_2}(1 - e^{-tE_2/\eta})\right] \tag{4.1}$$

where, $D(t)$ is the creep compliance, E_1 is the instantaneous modulus, E_2 and η are time dependent parameters. The data from the indentation tests were used to determine the

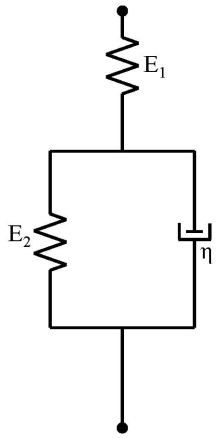

Figure 4.4: Voigt spring and dashpot viscoelastic model

instantaneous modulus and the time dependent parameters for each of the identifiable phases for each bitumen specimen.

4.3.4 Finite Element Analysis

In order to study the composite effect of individual phases present within the asphalt binder a FE model was developed for each of the two binders. The phase images obtained using the AFM were used as geometry inputs for the FE model. Figures 4.5 and 4.6 show the FE meshes along with the corresponding AFM phase images. The "bee" phases are highlighted in green, the "bee casing" regions are highlighted in red, and the "interstitial" regions are highlighted in light blue in fig. 4.5 and 4.6.

The measurements obtained using the AFM indentation tests were used as the material property inputs for the FE model. More specifically, the Abaqus FE software used in this study requires a Prony series stress relaxation function to model the viscoelastic response. The expression is given by:

$$g(t) = 1 - \sum_{i=1}^{n} g_i(1 - exp(-t/\tau_i)) \tag{4.2}$$

where, $g(t) = G(t)/G_0$ is a non-dimensional shear relaxation modulus. The terms g_i and τ are the time dependent Prony series parameters, and g_i is calculated based on G_0 and G_n (time dependent Prony series shear modulus parameter). $G(t)$ is the time dependent shear relaxation modulus of the specimen, and G_0 is the instantaneous shear modulus of the specimen, which is calculated internally by using the specified Young's Modulus E and the Poisson's ratio μ of the material. With the use of Laplace transformation, the creep compliance function given by the Voigt spring-dasphot analog model was transformed to a one term Prony series required for Abaqus implementation. The FE simulation entailed the application of a strain of 1% being held for a duration of 4 seconds.

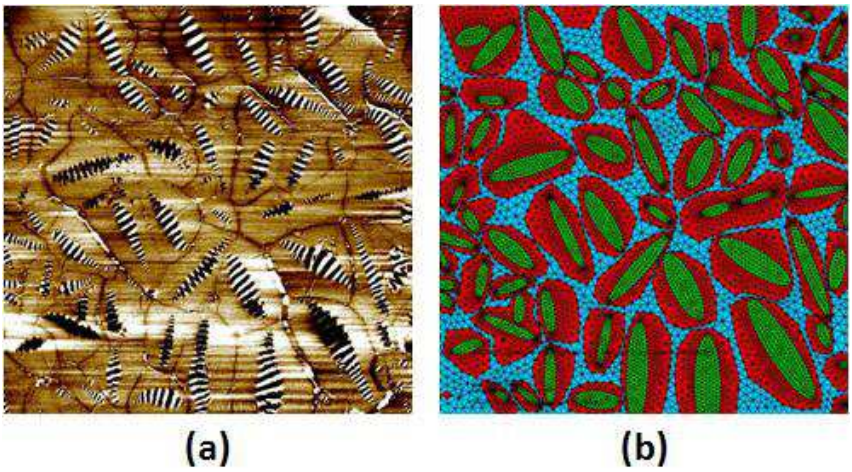

Figure 4.5: (a) AFM phase image and (b) Finite element mesh of asphalt binder A (50x50 microns^2)

4.3.5 Loading Frame Setup

In order to examine the effect of applied load/displacement on the microstructure of asphalt binder a loading frame was designed to precisely apply tensile displacement to the test specimen. Due to the sensitivity of the AFM to electrical noise the device was designed to

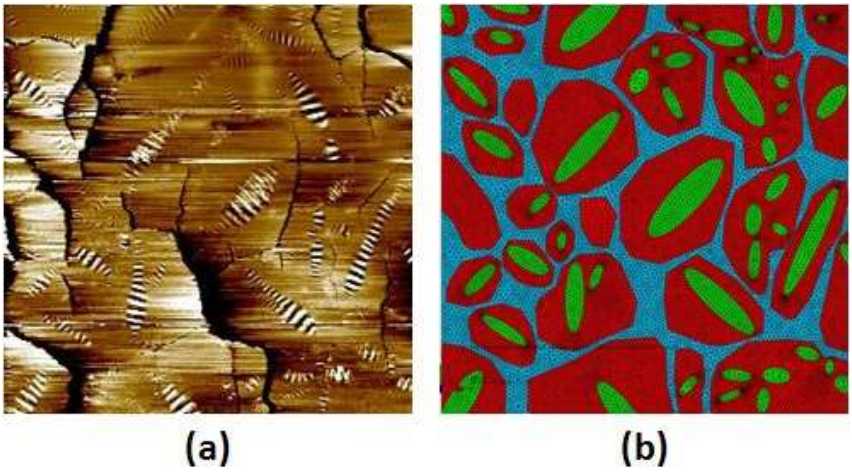

Figure 4.6: (a) AFM phase image and (b) Finite element mesh of asphalt binder B (50x50 microns^2)

be manually driven using a micrometer drive. Figure 4.7 is a schematic of the loading frame. Axial displacement of the non-rotating spindle was achieved using a micrometer drive with precision of 0.0001 mm. The specimen is held between two metal plates that are screwed onto the fixed spindle and the micrometer spindle allowing it to translate along the spindle axis. The spindles are held onto the base plate using a metallic U-frame. Figure 4.8 shows the final prototype of the loading frame that was used to carry out the experiments.

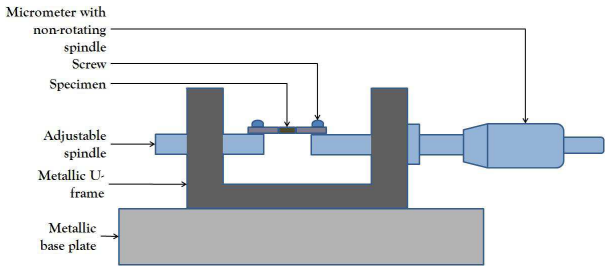

Figure 4.7: Micro-loading frame design

Once the specimen was prepared it was attached to the loading frame using the screws

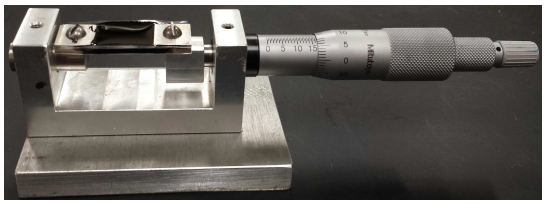

Figure 4.8: Micro-loading frame final prototype

on the metallic fixture plates. The experimental procedure used to study the effect of tensile displacement on the microstructure is described as follows:

- The initial length of the specimen was measured using a vernier caliper. Using this measurement the amount of displacement that was to be applied in order to obtain 1% and 5% strain was calculated.
- Once the sample was mounted on the loading frame it was allowed to rest for ten minutes to allow the binder to relieve any stresses that may have built up during the mounting of the specimen.
- The sample was then imaged using AFM phase imaging in its initial condition without any load being applied.
- The amount of displacement necessary to obtain 1% tensile strain was then applied. The specimen was allowed to relax for a period of five minutes in order for it to reach a steady state condition. The specimen was then re-imaged to obtain the microstructure after deformation.
- Each time a minimum of five 50x50 microns^2 images were obtained.
- This process was repeated and AFM images of binder microstructure were obtained after 1% and 5% applied tensile strain.

4.4 Results

4.4.1 AFM Creep Indentation Results

Using the creep indentation technique discussed in the methodology section, viscoelastic properties for the "bee" phase, the "bee casing" phase, and the "interstitial" phase were obtained. Figures 4.9 and 4.10 show the creep indentation response of different phases in bitumens A and B. The applied constant load was calculated to be approximately one micronewton. The load was applied for a period of four seconds and the indentation response was fit to a conical Sneddon viscoelastic solution in order to obtain the viscoelastic creep compliance parameters for each phase. Table 4.1 summarizes these results.

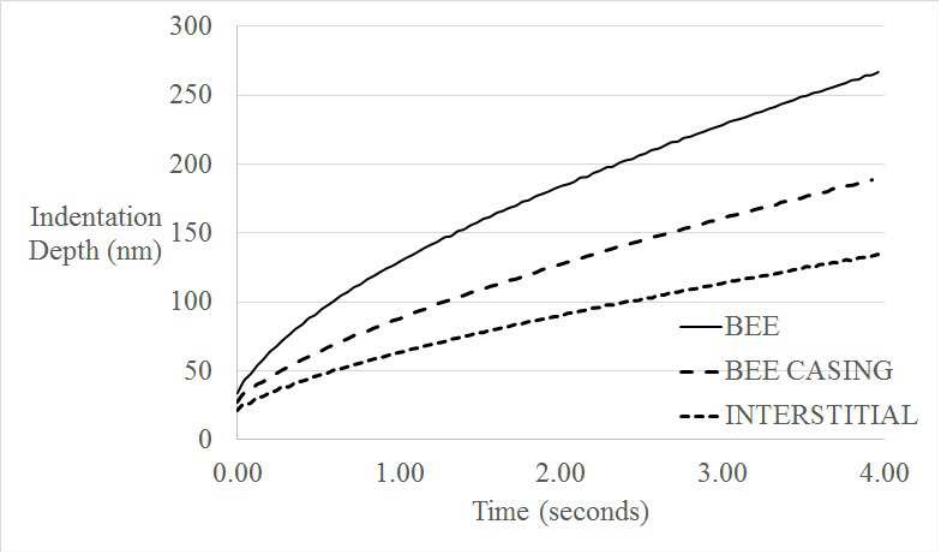

Figure 4.9: Viscoelastic creep indentation response of asphalt binder A Unaged

4.4.2 Results from the Finite Element Analysis

Figures 4.11 (a) and (b) show the von Mises stress contours for FE simulations of stress relaxation experiments performed on binders (a) A and (b) B. The highest stresses were

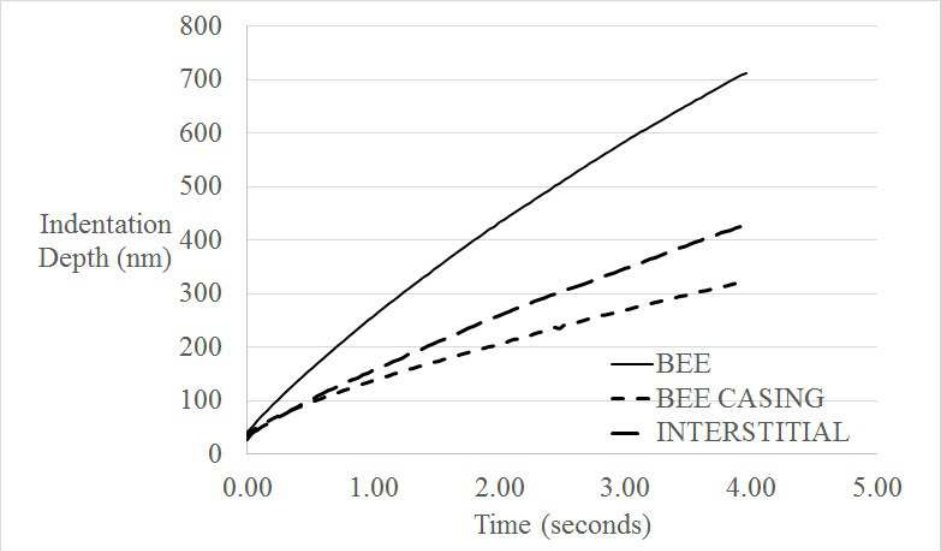

Figure 4.10: Viscoelastic creep indentation response of asphalt binder B Unaged

Table 4.1: AFM creep indentation analysis of asphalt binder A and B

Binder	Parameter (unit)	Bee	Bee Casing	Interstitial
A	E1 (Pa)	2.66E+09	4.12E+09	5.25E+09
A	E2 (Pa)	2.00E+04	9.00E+05	9.00E+06
A	eta (Pa.s)	1.79E+08	3.52E+08	8.02E+08
B	E1 (Pa)	1.75E+09	2.53E+09	4.35E+09
B	E2 (Pa)	5.00E+04	8.00E+04	9.00E+04
B	eta (Pa.s)	2.43E+07	1.32E+08	6.82E+07

observed in the interstitial phase and the lowest stresses were observed in the bee phase. The bee casing phase exhibits an intermediate level of stresses compared to the other phases. Figure 4.12 (a) and (b) show the internal distribution of tensile strains experienced by both binders. The contours here show that the bee regions experience the highest local tensile strains while the interstitial zones experience the lowest amount of local tensile strains which is consistent with the results shown in figure 4.11 (a) and (b).

Table 4.2 shows the maximum and minimum von Mises, and tensile strain values for

both binders based on the FEM simulations. The maximum stress for binders A and B are approximately 2.5 and 3.5 times the minimum stress, respectively.

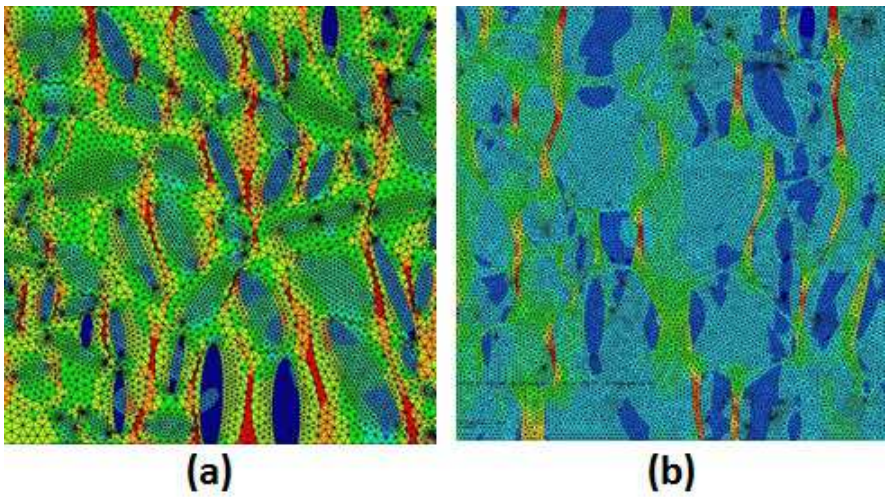

Figure 4.11: Von mises stress contours for finite element simulations of asphalt binders (a) A and (b) B (50x50 microns^2)

Table 4.2: Finite element results of stress relaxation simulation of asphalt binders A and B

BINDER	MAX TENSILE STRAIN	MIN TENSILE STRAIN	MAX VON MISES STRESS	MIN VON MISES STRESS
A	0.169	0.0613	0.628 GPa	0.258 GPa
B	0.194	0.0503	0.558 GPa	0.167 GPa

4.4.3 AFM Imaging Before and After Load Application

Three distinct phases were observed in the AFM images of each of the two binders (Figure 4.13). The first phase can be described as the "bee" phase, a second phase that surrounds

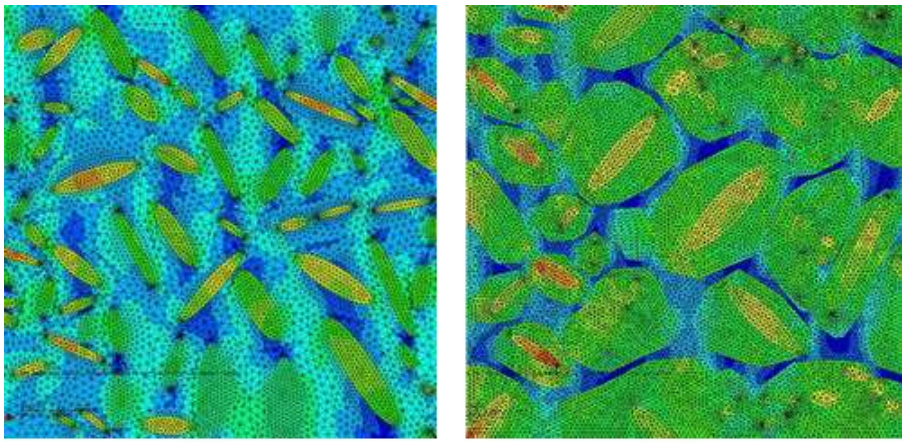

Figure 4.12: Tensile strain contours for finite element simulations of asphalt binders (a) A and (b) B (50x50 microns^2)

the "bee" phase referred to as the "bee casing" phase, and a third phase referred to as the "interstitial phase" that occupies the space between the bee casing. The interstitial phase is not clearly visible without image enhancement and has been highlighted for the convenience of the reader in figure 4.14 .

Figure 4.15 shows AFM phase images of binders A and B after the application of one percent strain. Both test specimens show clear signs of load induced phase separation (LIPS). It is also evident from the microstructural changes in the images that the LIPS occurs around the bee casing phases and go through the interstitial zones highlighted in red in figure 4.14. Figure 4.16 shows AFM phase images of binders A and B after five percent strain. Microstructural changes observed here are consistent with that of figure 4.15. Here the LIPS zones are more prominent.

In order to quantitatively assess the changes in the microstructure due to the applied tensile strain we employed image analysis techniques using the open source image analysis tool ImageJ. Various geometric attributes were obtained and a comparison of these attributes was

Figure 4.13: AFM phase image showing microstructural features of asphalt binder (a) A and (b) B (50x50 microns^2)

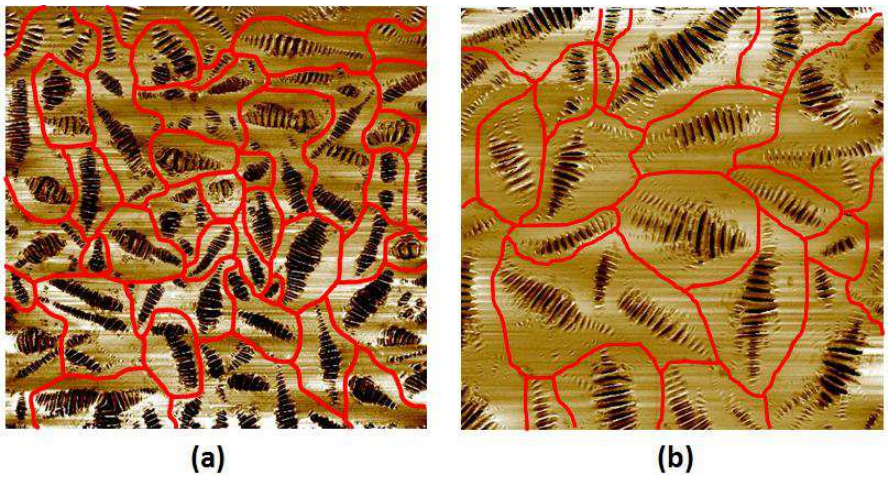

Figure 4.14: AFM phase image showing interstitial phase of asphalt binder (a) A and (b) B (50x50 microns^2)

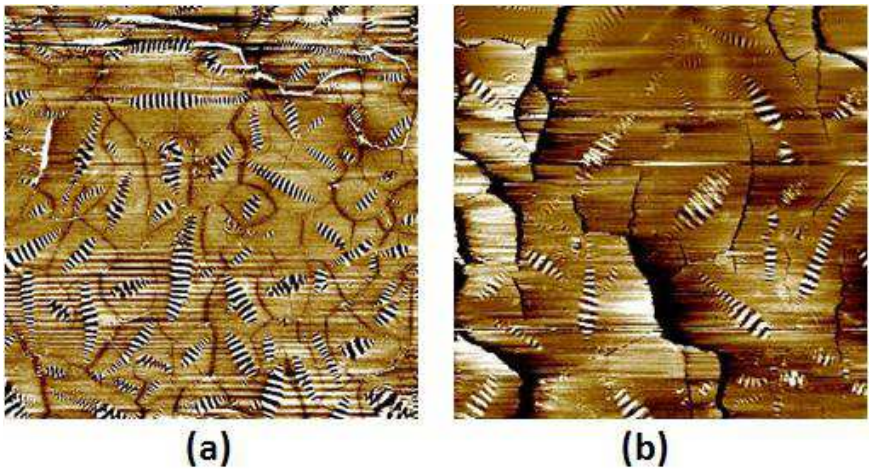

Figure 4.15: AFM phase image showing microstructural features of asphalt binder (a) A and (b) B (50x50 microns^2) after 1% strain

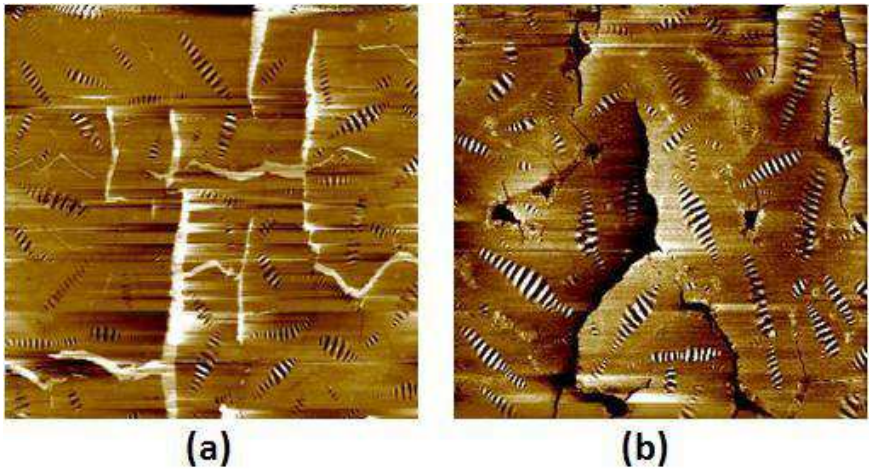

Figure 4.16: AFM phase image showing microstructural features of asphalt binder (a) A and (b) B (50x50 microns^2) after 5% strain

done before and after strain was applied to the test specimens. Due to phase separation and changes that occurred in the bee casing and interstitial phases, comparisons here are only made on the basis of the discrete bee phase. Table 4.3 compares the distribution of the bee structures before and after load is applied to binders A and B.

Table 4.3: Microstructural analysis of asphalt binder A and B

STRAIN LEVEL	TOTAL COUNT	MEAN AREA (μm^2)	%Area
before (binder A)	743	2.93	21.39
one percent (binder A)	586	2.99	17.07
five percent (binder A)	490	2.61	12.35
before (binder B)	369	5.40	19.58
one percent (binder B)	317	5.29	16.26
five percent (binder B)	272	3.21	8.69

4.5 Discussion

4.5.1 Microrheology

A creep AFM indentation technique was used to obtain the micro-rheology of the three different phases observed in each binder (Figures 4.10 and 4.9). The indentation response for a similar phase was distinctly different for each binder; this would be expected given that the two binders were from very different sources and had different chemical composition and mechanical properties. The rank order of instantaneous modulus for each of the three phases was similar for both binders. The bee phase had the lowest while the interstitial phase had the highest magnitude of instantaneous modulus. The time dependent response showed a slightly

different trend for binder A compared to binder B. Although the interstitial phase was determined to be the least compliant for binder A, it showed an intermediate level of compliance compared to the two other phases for binder B. Dourado et al. [10] and Allen et al. [4] reported similar trends between the bee and the surrounding phases using similar indentation techniques. The findings from this study and the studies of Dourado et al. [10] and Allen et al. [4] strongly suggest that the mechanical properties of the different phases are substantially different. A corollary to this observation is that stress localization is likely to occur within the bitumen when subjected to external loads. Such localization will be a function of the rheology and geometric distribution of phases. However, further work is needed to determine whether there exists any consistent relationship between different structural features and rank order of stiffness.

Note that the authors recognize that the properties obtained for different phases through such microrheological measurements and analyses are not absolute properties. For example, the properties are obtained by surface indentation and as such the material structure beneath the surface even for a thick melt specimen will influence the results obtained. Similarly, the indentation using a conospherical tip is not the same as one dimensional uniaxial loading. However, despite these biases, the measured microrheology does show substantial and consistent differences in mechanical properties of the different phases. While such measurements may not be perfect, they are nonetheless a good semi-quantitative representation of the properties of different phases within the binder.

4.5.2 Finite Element Analysis

Figures 4.11 (a) and (b) illustrate the internal distribution of the von Mises stress in both binders undergoing stress relaxation over a period of four seconds. As expected, the highest level of stress was found within the interstitial and bee casing phases while the bee phase experienced the lowest level of stress. This suggests that the interstitial or the bee casing phases are the most likely to experience damage once the specimen is loaded. One of the

more interesting observations from these analyses was that the local stress amplification for binder A (ratio of the highest to lowest local stress) was much lower in magnitude compared to the stress amplification in binder B. Also, both binders A and B had a similar percentage of area occupied by the bee structures (approximately 20%). However, binder A had a higher number of bee structures with a smaller mean size compared to binder B, which had fewer bee structures with a larger mean size. We speculate that the dispersed nature of these bee structures in binder A results in a more homogenous stress distribution and consequently lower stress amplification.

4.5.3 The Effect of Tensile Strain on Microstructure

A comparison of images before and after applying 1% tensile strain (e.g. Figure 4.15) clearly shows the formation of a crack like network notably between the bee structures. The term "crack like" is emphasized here because the experimental work in this area is premature to conclude that there features are indeed cracks in the conventional sense, wherein a new surface is formed. Instead these features may be more appropriately referred to as the change in phase or morphology due to the action of load or simply load induced phase separation (LIPS). It is speculated that these LIPS zones are the precursor to conventional forms of damage. Another notable feature of the LIPS zone is that these occur predominantly in areas in between the bee casings or the "interstitial spaces" as described previously. In fact, based on the microrheology measurements and FE analyses the regions that correspond to the LIPS zones are also the reasons that correspond to higher stress amplification (discussed in section 5.2)

The second observation from these experiments is that the LIPS zones occur most likely at the expense of the bee-structures. In other words, the tensile strain not only resulted in the formation of the LIPS zones but also the disintegration of the bee structures that possibly were in the proximity of these zones. This is further supported by the quantitative analysis of these structures using ImageJ before and after the application of the tensile strains. Binders A and B

had approximately 21% and 14% reduction in the number of bee structures, respectively after the application of 1% strain. The area occupied by these bee structures was approximately 3-4% less of the total surface after 1% applied strain. Also, the smaller bee structures most likely were the first to completely dissipate due to the tensile displacement experienced. The larger bee structures were only partially dissipated since the amount of the strain applied may not have been large enough in magnitude to cause complete dissipation of the larger area taken up by the larger sized features.

In summary, the numerical simulations verify that differences in mechanical properties among the different phases lead to stress localization. In the FE simulations we can clearly see that the highest stresses occur in the bee casing and interstitial phases. The formation of the LIPS zones or crack like networks correlates well to the locations where highest levels of stresses occurred in the FEsimulations. This verifies that the differences in material properties most likely lead to high levels of localized stresses that lead to damage initiation in the interstitial and the bee casing phases.

4.6 Conclusions

The objective of this study was to evaluate the inter-relationship of tensile load, damage nucleation and microstructure of the bitumen. A combination of AFM imaging and creep indentation measurements were used to obtain geometry and microrheology of the phases observed on the bitumen surface. This information was used with the FE method to examine the internal stresses in the binder and potential evolution of damage. The following conclusions are drawn from the study:

- AFM phase imaging revealed three different phases for each of the two binders studied. AFM indentation was used to semi-quantitatively evaluate of the rheology of these phases for a given bitumen, referred to as microrheology. Results clearly show that the compliance of different phases within a bitumen are substantially different. In other

words, viscoelastic properties obtained through AFM creep indentation experiments show material inhomogeneity exists within the bitumen at a micrometer length scale.

- The composite FE simulations show that the differences in properties of the different phases result in high levels of localized stress or stress amplification within the interstitial zones. The stress amplification was higher for the binder with larger but fewer bee structures compared to the binder with smaller but more bee structures.

- The application of tensile load or displacement causes cracks or phase separation zones to appear which are referred to as LIPS zones.

- The high stress regions observed from the FE simulation coincide with the areas within which the LIPS zones form. This suggests that material inhomogeneity leads to the development of high stresses within interstitial zones which leads to damage nucleation and propagation.

The above conclusions suggest that the ability to manipulate the microstructure of bitumen (e.g. using chemical or other modifiers) has a significant influence on the durability and inherent ability of the bitumen to resist damage. Further work is required to (i) more accurately characterize the microrheology of bitumen, (ii) more accurately and quantitatively assess the relationship between damage evolution in the bitumen and its microstructure, and (iii) establish a better understanding of the relationship between the chemical composition of the bitumen and its microstructure.

5. A STUDY OF EFFECT OF GEOMETRY OF MICROSTRUCTURE ON THE MECHANICAL RESPONSE OF ASPHALT BINDER TREATED AS A COMPOSITE

5.1 Introduction

The study of asphalt binder microstructure is heavily motivated by the contribution of the microstructure towards its mechanical behavior. Previous studies show how the microstructural features present within the asphalt binder play an important role towards its overall mechanical properties [10, 4, 48, 21]. The work of Allen et al [4], and Jahangir et al. [21] specifically establish the heterogeneous nature of the phases found within asphalt binder referred to as the bee, bee casing, and interstitial by examining their geometry and rheology. Using Atomic Force Microscopy (AFM) imaging techniques Jahangir et al. [21] were able to determine the shapes and distributions of these microstructural features. In addition, using an AFM creep indentation technique they were able to measure time dependent mechanical properties of these phases and were able to establish the composite response of asphalt binder subjected to tensile strains using finite element simulations. Furthermore, Jahangir et al. [21] established that the presence of these microstructural features are directly related to damage initiation and propagation within asphalt binder. When thin bitumen samples of asphalt binder were subjected to high levels of tensile strain, phase separation and cracking were observed primarily in the interstitial zones within the asphalt binder.

Although the distribution and density of the microstructural features in asphalt binder were found to be completely random, little work has been completed to establish how the geometry of these features contribute towards the overall composite mechanical response. In particular, the bee/bee casing features are of particular interest due to their defined oblong shapes. The AFM proved to be a invaluable in terms of obtaining geometries of these microstructures and giving researchers a clear idea of how the composition, shape, and orien-

tation of these features can vary from sample to sample and even from one location of interest to another [21]. In this work, the effect of the geometry of aforementioned microstructural features is examined in detail using image creation and numerical analysis techniques. The primary focus here is to establish how various different geometric parameters affect the output maximum and minimum stresses. Determination of stress distribution within the material is crucial since localized high stresses can lead to damage initiation and propagation.

In this study, finite element simulations of asphalt binder being subjected to tensile loads are performed for both a defined microstructural arrangement and also for a random arrangement of microstructural features. The finite element technique provides an effective method for simulating scenarios that would otherwise be impossible. In addition, the finite element method can be used to obtain solutions to the problem of interest without carrying out repititive, costly, and time consuming experimentation. Here, the images used to create the geometry of the finite simulations of asphalt binder with a defined microstructural arrangement are created using AutoCAD. The images used to create the geometry of the finite element simulations of asphalt binder with random microstructural arrangements are created using a *Mathematica* image creation algorithm. The various geometric parameters of interest are the size, area fraction, and distribution of microstructural features on the resulting stresses. In order to only study the effect of the geometry on the instantaneous stress response, the asphalt binder is treated as a linear elastic material. The focus here is to analyze the elastic response due to the heterogeneity within the material properties evident by our previous work and the geometry of the microstructural features.

5.2 Scope

This work is a continuation of the examination of the microstructural features or phases present within asphalt binder which were found to have unique mechanical properties by [21]. The goal of this work is to establish how the size, area fraction, and density of bee/bee casing features affect the resulting stresses and strains when subjected to a monotonic load. The

aim of this work is to demonstrate that in addition to the heterogeneity present within asphalt binder, the geometry of the microstructural features also affect the output stresses, strains, and have an effect on the resulting damage. The main components of this work include:

- Define the asphalt binder as a material composed of multiple phases with a defined geometry. Here both the bee and the bee casing phases are defined using an elliptical geometry as evidenced by our previous findings. The bee and the bee casing features have been found to be interrelated, where the bee casing surrounds the bee feature. In this work the primary interest is to study the effect of the geometry of the bee and bee casing features on the output stress.

- Generate images of asphalt binder microstructure with specified geometry and location for the bee/bee casing features using Autocad.

- Generate images asphalt binder microstructure with geometry of bee/bee casing features based on a Gamma distribution using a Mathematica image creation algorithm. In addition, randomly distribute the location of the bee/bee casing features.

- Use the images created using the specifications above to create mesh for the finite element simulations. Apply a vertical distributed axial load of 1 MPa to the top surface of the sample. Apply symmetry boundary conditions to the left and bottom surface of the model. (see Figure 5.1)

- Analyze the effect of bee/bee casing size, area fraction, and packing on the resulting stresses using finite element simulations based on the created images representing certain geometric configurations of interest of asphalt binder.

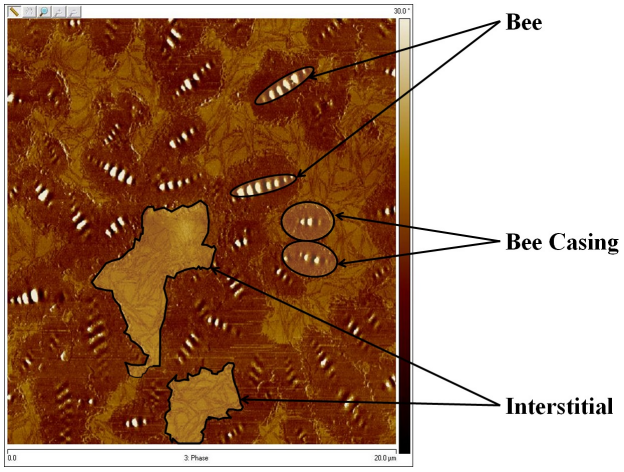

Figure 5.1: Microstructural phases present within asphalt binder

5.3 Methodology

5.3.1 Discretization of Asphalt Binder Into Domains

Jahangir et al. [21] used AFM imaging techniques to determine the microstructure of asphalt binder. They found that the asphalt binder surface contained three unique phases with varying mechanical properties (figure 5.1). These phases were referred to as the bee phase, bee casing phase, and the interstitial phase. [21] also correlated the existence of these phases to phase separation and damage resulting from the application of high levels of tensile strains. They also discovered that high stress localization in the vicinity of interstitial and bee casing phases led to phase separation and cracking which were referred to as load induced phase separation or LIPS. In this study, the asphalt binder is divided into three separate domains, i.e. bee, bee casing, and interstitial. Here the asphalt binder is modeled as a linear elastic material and the Young's modulus for the bee, bee casing, and the interstitial phase is defined to be 2 GPa, 4 GPa, and 6 GPa. These values in the same order of magnitude and are comparable to the microrheology determined in Section 3 and Section 4. All three phases were designated to be virtually incompressible and, therefore, a Poisson's ratio of 0.49 was used in this study.

5.3.2 Construction of Two Dimensional Finite Element Simulations Based on Specific Geometric Arrangements of Microstructural Phases

As determined in our previous work (Section 3 and Section 4) microstructural features within asphalt binder exhibits a random distribution in terms of location. The sizes of the bee/bee casing features can be represented using a highly negatively skewed normal distribution or a Gamma distribution. Here, two separate approaches are used to construct the images used to create the the geometry for the finite element simulations performed in this study. First, a specific arrangement of microstructural features is used to study the effect of area fraction, and density of the bee/bee casing features on the resulting stresses. The focus here is to determine the maximum stress within the model, in addition to the distribution of the stresses within the model. The variation of the maximum stresses with respect the aforementioned geometric parameters of interest are also examined.

In order to create a specific arrangement of bee/bee casing phases within a matrix of interstitial material Autocad was used. An example of microstructure constructed using this method is shown in figure 5.2.

5.3.2.1 Effect of Area Fraction on The Resulting Stress Output

In this portion of the study, the area fraction of the bee/bee casing phases are varied and the resulting stresses are examined. The geometric parameter values in this analysis are shown in table 5.1.

5.3.2.2 Effect of Packing on The Resulting Stress

In this portion of the study, the effect of packing of the bee/bee casing features are examined. In order to examine the packing the of the bee/bee casing features the horizontal distance between the adjacent bee/bee casing features are varied. Table 5.2 shows the geometric parameters values used for this analysis.

In each case the number of bee features, area fraction of bee phase, bee casing feature

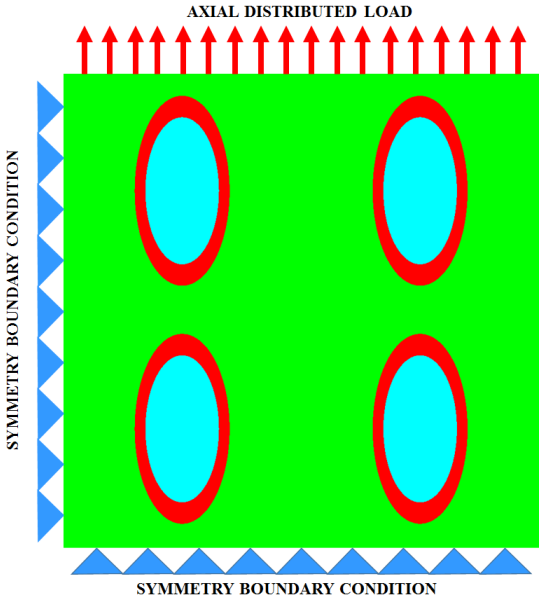

Figure 5.2: Typical finite element geometry of asphalt binder created using AutoCAD. Light blue area highlights the bee phase, red area highlights the bee casing phase, and the green area highlights the interstitial phase.

Table 5.1: Geometric parameters of microstructural features

NUMBER OF BEE FEATURES	AREA FRACTION	BEE CASING SEMI-MAJOR AXIS	BEE SEMI-MAJOR AXIS	BEE TO CASING AREA RATIO
4	0.25	9.9736	7.7255	0.6
4	0.3	10.9255	8.4628	0.6
4	0.35	11.8009	9.1409	0.6

Table 5.2: Geometric parameters of microstructural features

TRIAL	NUMBER OF BEE FEATURES	HORIZONTAL GAP
1	4	15
2	4	5
3	4	2.5
4	4	1.25
5	4	0.625

semi-major axis, and bee feature semi-major axis, bee to bee casing area ratio, and vertical gap were kept constant at 0.25, 9.97 micrometers, 7.73 micrometers, 0.6, and 5 micrometers respectively.

5.3.3 Construction of Two Dimensional Finite Element Simulations Based on Random Geometric Arrangements of Microstructural Phases

Early studies show that the orientation, and location of the bee structures within asphalt binder exhibit a random distribution. The size of the bee structures were non-normally distributed are the probability density function of the bee structures can be well described using a Gamma distribution (Appendix A). In order to correctly simulate the distribution of bee sizes a Mathematica image generation script was developed which used the Gamma distribution to select the size of the bee structures. The Gamma distribution is especially suitable for describing data that is non-normally distributed and is bound by a lower limit. In this case the lower limit of individual bee feature used for the Gamma distribution size is zero. For more details on the Gamma distribution please see the work of Gentle [15]. Using the image generation script the area fraction of bee/bee casing phase, orientation range, and also the variability within the bee feature sizes can be controlled. The image created using the Mathematica script was then used to create the mesh of the finite element model using OOF2 open source finite element package. Finally, the mesh obtained from OOF2 was used to develop the finite element model and obtain the solution using Abaqus commercial finite element package.

In this portion of this work, two geometric effects were examined in detail. The first factor examined was the effect of area fraction of the bee/bee casing phase on the maximum stress response. The second factor examined was the effect of the number of bee features present within the sample on the output maximum stress. In this case the orientation of the bee features were fixed to a vertical position and the individual bee features were constrained to be the same size in order to reduce the effect of variability within the orientation and the

size of the features.

5.4 Results and Discussion

5.4.1 Two Dimensional Finite Element Simulations Based on Specific Geometric Arrangements of Microstructural Phases

Figure 5.4 shows the maximum stress ratio (maximum von Mises stress/axial load) as a function of the area fraction. von Mises stress is a stress measure that accounts for all normal and shear stresses at a given point and is given by equation 5.1:

$$\sigma_{mises} = \sqrt{0.5[(\sigma_x - \sigma_y)^2 + (\sigma_y - \sigma_z)^2 + (\sigma_z - \sigma_x)^2]} + \sqrt{3(\tau_{xy}^2 + \tau_{yz}^2 + \tau_{zx}^2)}] \qquad (5.1)$$

Here σ_x, σ_y, σ_z are the normal stress components and τ_{xy}, τ_{yz}, τ_{zx} are the shear stress components. Due to the two dimensional nature of the simulations used in this study out of plane stress components can be assumed to be zero.

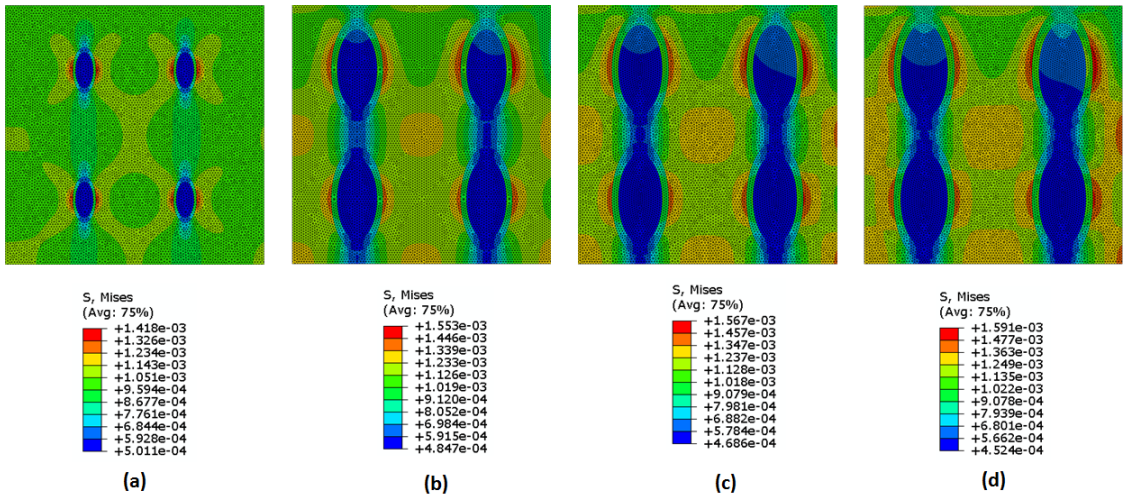

Figure 5.3: von Mises Stress contour plots for area fraction of (a) 5 % (b) 25 % (c) 30 % (d) 35 % for bee/bee casing phase within asphalt binder subjected to axial vertical tensile load of 1 MPa

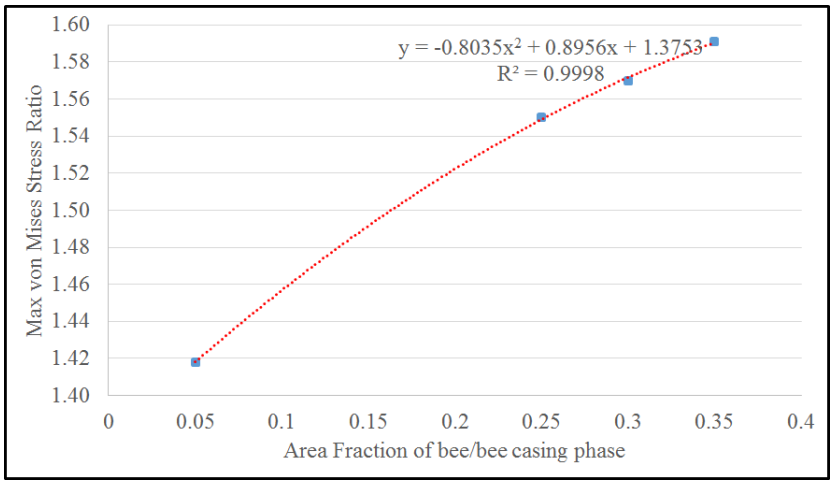

Figure 5.4: Maximum stress ratio as a function of area fraction of bee/bee casing phase

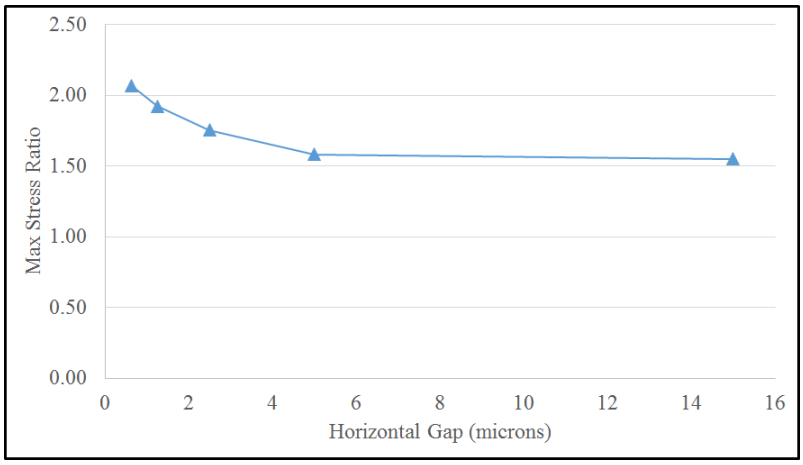

Figure 5.5: Maximum stress ratio as a function of horizontal gap between bee/bee casing phase

Figure 5.3 shows contour plots corresponding to the stresses presented in figure 5.4. In figure 5.4 we observe a direct correlation between the area fraction and the maximum stress ratio. A polynomial line of best shows the maximum stress ratio can be described as a quandratic function of the area fraction of the bee/bee casing phase.

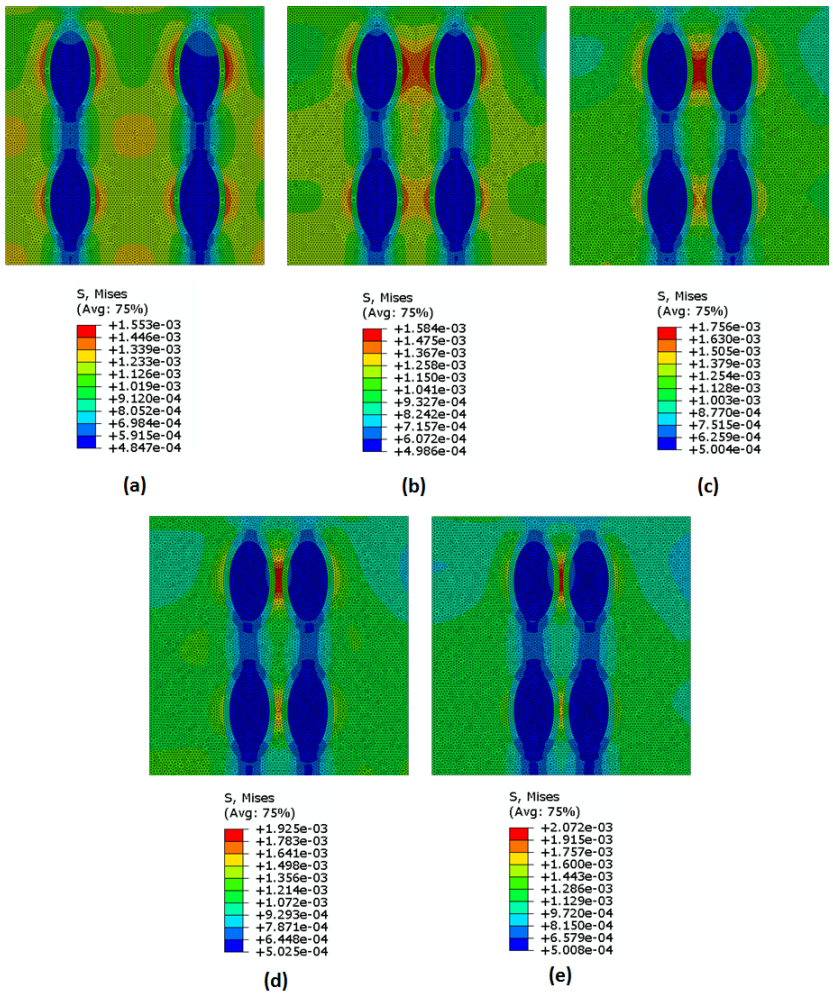

Figure 5.6: von Mises Stress contour plots for horizontal gap of (a) 15 μm (b) 5 μm (c) 2.5 μm (d) 1.25 μm and (e) 0.625 μm for bee/bee casing features within asphalt binder subjected to axial vertical tensile load of 1 MPa

Figure 5.5 show the maximum stress ratio as a function of the horizontal gap between adjacent bee features. Here an initial inverse relationship is observed between the horizontal gap and the maximum stress ratio between the bee features. Once the horizontal gap surpasses 5 micrometers the change in the maximum stress ratio becomes negligible. The horizontal gap is of affects the maximum stress due to the maximum stress occurring on the vertical side of the bee feature due to a vertical axial load and is affected by the thickness of the matrix. The thickness of the matrix or the interstitial zone between neighboring bee features is the horizontal gap between the bee features itself. This is clearly demonstrated in figure 5.6. As the horizontal distance between the bee features is reduced the interstitial zones become narrower resulting in a higher aspect ratio of the interstitial zones and also a higher magnitude of stresses within the interstitial zones. Note that this only occurs due to the interstitial zones having the highest stiffness within the three identifiable phases of asphalt binder. This also demonstrates that if the loading was horizontal as opposed to vertical the vertical gap between the individual bee features would dictate the maximum stress ratio. These observations clearly imply that the packing of the bee/bee casing features has a strong effect on the resulting stresses. The contour plots also show that as the neighboring bee features come closer the high stress zones shown in red merge together. In addition, the data presented in the contour plots suggest that the bee features themselves exhibit the minimum stresses and as evidenced from the findings in Section 3 are the least likely regions for crack initiation. This observation was also confirmed through experimental observation of LIPS zone formation in both Section 3 and Section 4.

5.4.2 Two Dimensional Finite Element Simulations Based on Random Geometric Arrangements of Microstructural Phases

Figure 5.7 shows the maximum stress ratio as a function of area fraction of bee/bee casing phases. Here an overall increase in the maximum stress ratio is observed with an increase in the area fraction of the bee/bee casing phase. Although an overall increase in the maximum

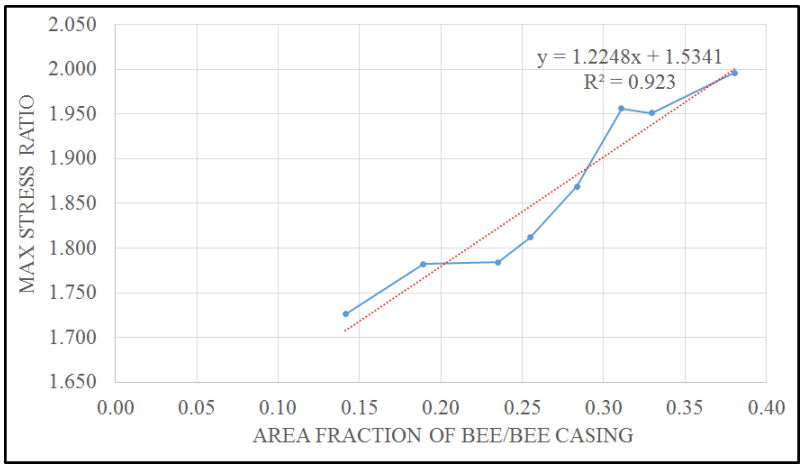

Figure 5.7: Maximum stress ratio as a function of area fraction of bee/bee casing phase

stress ratio was observed, unlike the results of the non-random distribution analysis as a function of area fraction here a specified correlation function cannot be established. The data was fit to a linear relationship with an R^2 of 0.923 as shown. Figure 5.8 shows the stress distribution as a function of number of bee/bee casing features. Here an increase in the number of bee features is observed with an increase in the area fraction. In addition an increase in the area fraction of the bee/bee casing phase lead to an increase in the number of bee/bee casing features. This leads to higher number of thin sections of interstitial zones where potentially high stresses can occur. A close look at the stress distribution shown in the contour plots exhibit an inverse correlation with the thickness of the interstitial zone perpendicular to the direction of the load, and the output stress due to the applied vertical axial distributed load. In fact, almost all of the high stress zones are observed to have a longitudinal slender shape and are oriented in the same direction as the loading direction. This again reinforces the notion that for the given difference in the material properties among the different phases present within asphalt binder, the packing of the bee features has a strong effect on the output stress due to the narrowing of the interstitial zones in the neighboring regions.

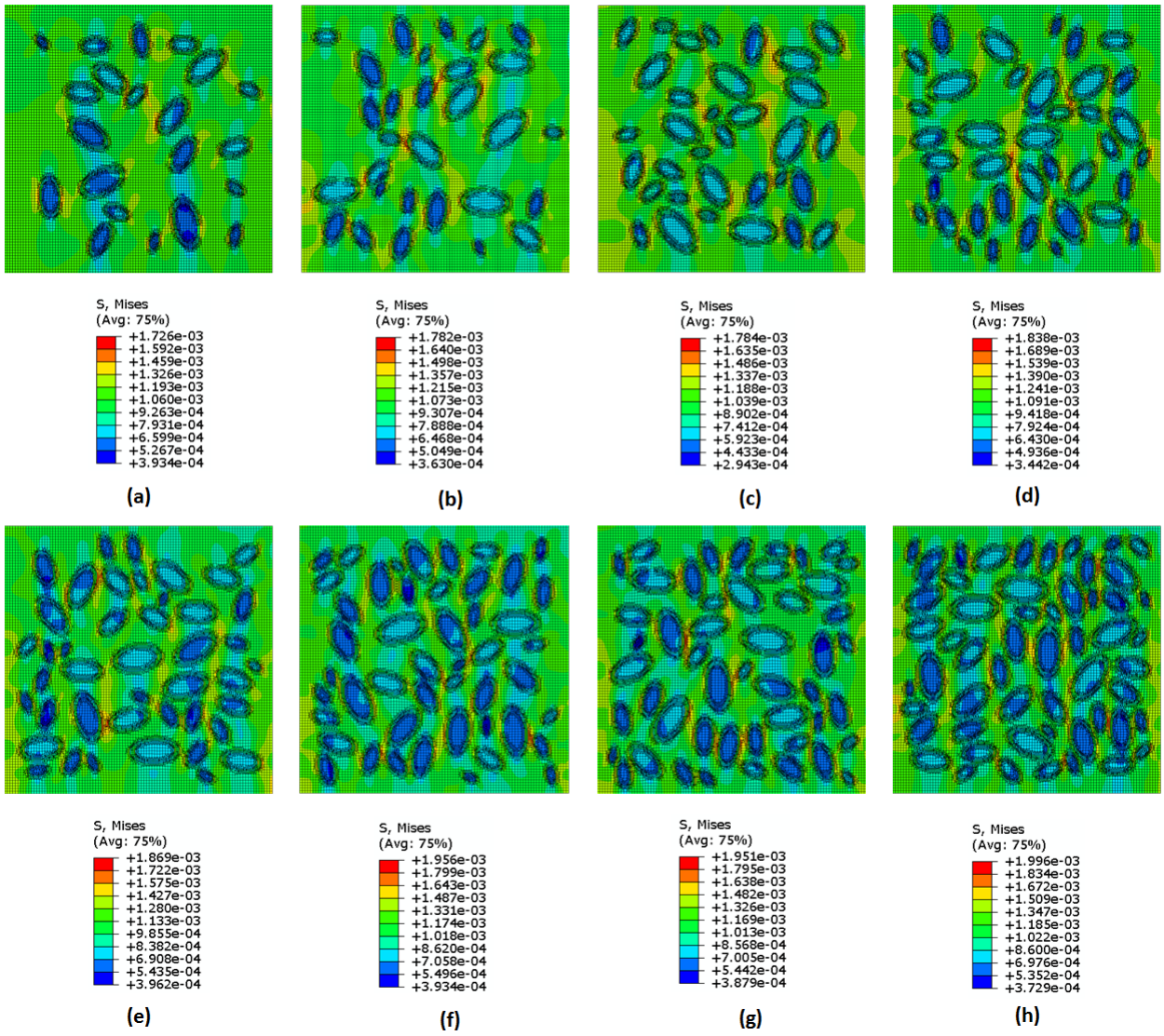

Figure 5.8: von Mises Stress contour plots for area fraction of (a) 15 % (b) 20 % (c) 25 % (d) 27 % (e) 30 % (f) 33 % (g) 35 % (h) 40 % for bee/bee casing phase within asphalt binder subjected to axial vertical tensile load of 1 MPa

The effect of packing of the bee features is further validated by the results shown in figure 5.9 which shows the maximum stress ratio as a function of the number of bee/bee casing features occupying 20% of the sample surface area. As the number of bee features are increased an overall downward trend is observed in the maximum stress ratio as shown in figure 5.10. In addition, the contour plots shown in figure 5.9 show that increasing the number of bee features despite keeping the area fraction constant increase the probability of localized high stress zones as demonstrated by the regions highlighted in red. This occurs due to the increased probability of bee features being placed closer to each other resulting from an increase in the overall number of bee features. An interesting point to note here is that as the number of bee features are increased the bee phase is dispersed over a larger area of the total sample. As speculated in Section 3 the dispersion of bee phases may lead to a lower value of maximum stress ratio. The relationship observed in figure 5.10 support this notion. As evident by the contour plots, although the number of localized high stress zones may increase with an increase in the number of bee features, due to the overall reduction in the magnitude of the stresses the probably of the occurrence of the LIPS zones may indeed reduce.

The numerical analyses performed here clearly suggest that geometric variation of the microstructural features can lead to variation in the stress distribution of the asphalt binder sample due to a loading. We observe that an increase in area fraction, and a reduction of the interstitial zone thickness will directly lead to an increase in the localized stresses. Thus, in order to design a binder with enhanced damage resistant properties, reducing the occurrence of the bee features through some chemical modification would be ideal. This would not only lead to increased homogeneity of the asphalt binder, but also lead to a uniform distribution of stresses within the material. In addition, further evidence by figure 5.9 an increase in the the number of bee features for a given area fraction will also lead to improved dispersion also resulting in increased homogeneity within the material.

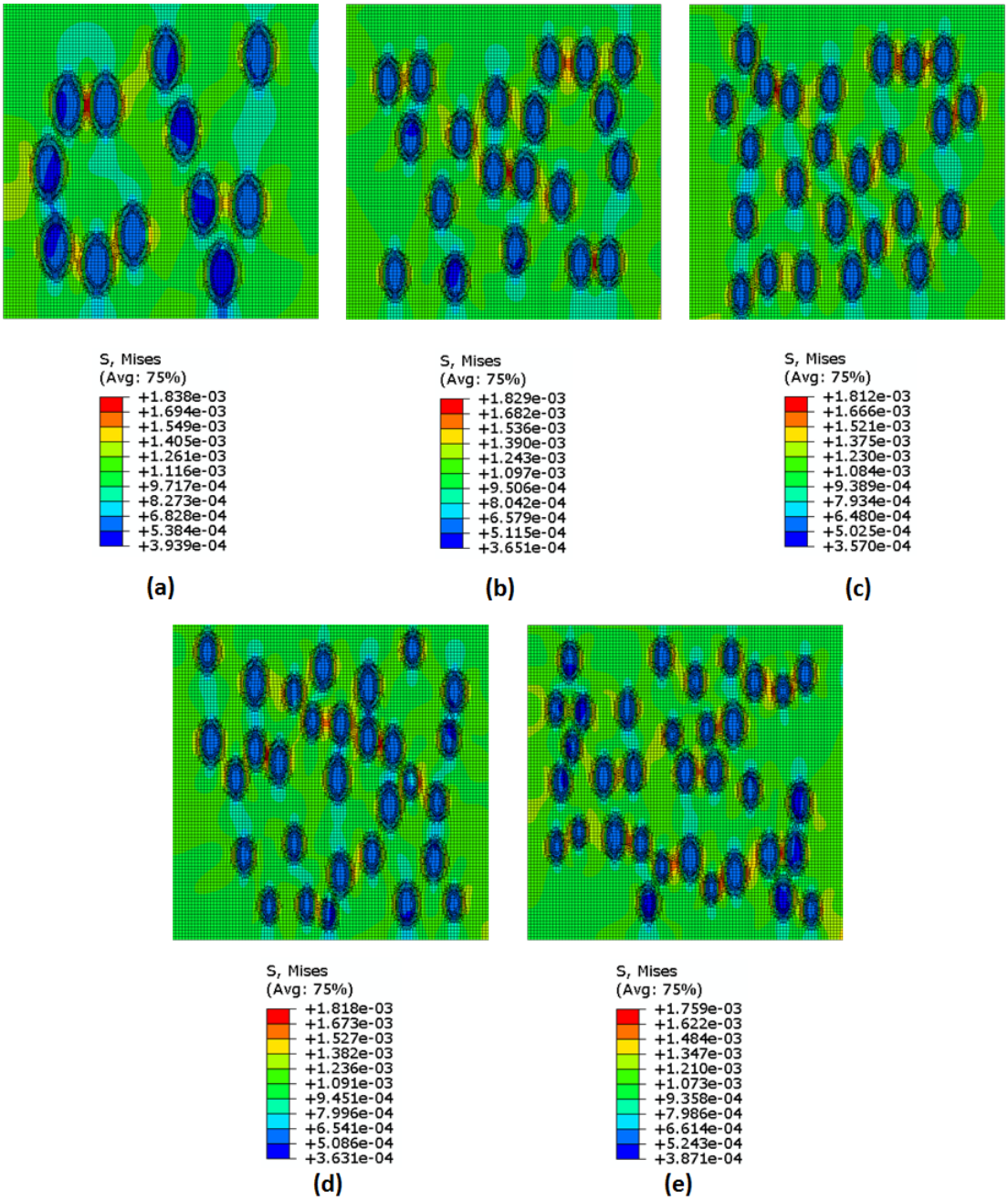

Figure 5.9: von Mises Stress contour plots for (a) 12 (b) 20 (c) 25 (d) 30 and (e) 34 bee/bee casing features within asphalt binder with an area fraction of 0.2 subjected to axial vertical tensile load of 1 MPa

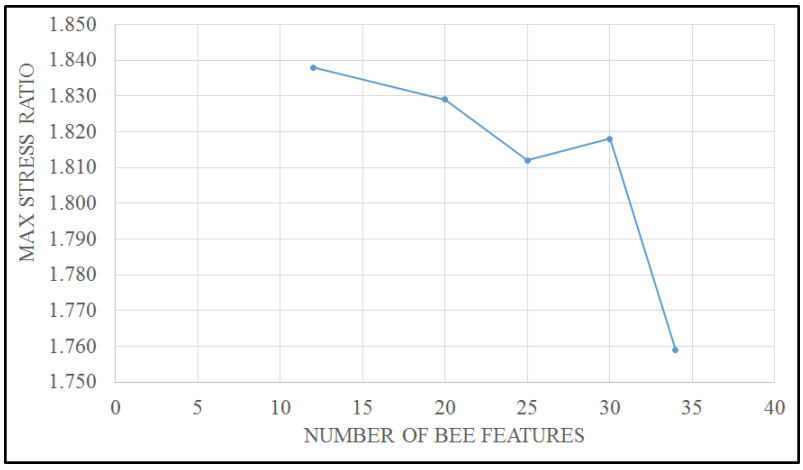

Figure 5.10: Maximum stress ratio as a function of number of bee/bee casing features with an area fraction of 0.2

5.5 Conclusions

In Section 2 and Section 3, experimental analysis of asphalt binder samples subjected to tensile loads provided with an insight and understanding of how the geometry of the microstructural features can vary due to loading, and aging. The objective of this study was to determine the effect of variation within geometric parameters of microstructural features present within asphalt binder on the resulting stresses. In order to complete this objective image creation techniques, along with the finite element method was used to carry out virtual experiments. The following conclusions can be drawn from the results of this study:

- An increase in the area fraction of the bee and bee casing feature resulted in an increase in the maximum stress ratio due to the increase of the probability of the formation of LIPS zones.

- The packing of the bee/bee casing features affect the local stress magnitudes. Interstitial zones with high aspect ratios located longitudinally in the same direction as the loading direction resulting from close placement of bee features results in high stresses

in that zone. Increasing the area fraction of the bee/bee casing feature also results in closer packing of these features.

- Increase in the number of bee features without increasing the area fraction of the bee and the bee casing phase can result in a reduction in localized stresses in addition to a reduction in the maximum stress magnitude. This occurs due to reduction of the aspect ratio of the interstitial zones between the bee features.

The findings of this study can be used as a guideline for future work in the design of modified asphalt binders with enhanced mechanical properties. The results obtained in this study clearly indicate that the geometry of the microstructural features present within asphalt binder have an effect on its mechanical response. Furthermore, different aspects of the geometry studied here potentially explain how damage can be reduced in asphalt binder. The modification of asphalt binder leading to changes in the composition and microstructure at the micron length scale can eventually lead to an enhanced pavement material with increased damage and distress resistance.

6. CONCLUSIONS AND RECOMMENDATIONS FOR FUTURE RESEARCH

The processes and mechanisms that lead to damage in asphalt binder are complex. In order to gain a proper understanding of these processes and mechanisms, the microstructure of asphalt binder must be examined in detail. In addition, the interrelationship of the asphalt binder microstructure to its mechanical properties and damage resulting from tensile loading can explain how it responds to different types of mechanical stimuli. This study implements a unique combination of experimentation and numerical analysis in order to understand how the microstructure of asphalt binder is related to damage. In order to reach this objective, AFM imaging, indentation, and image analysis techniques were employed. Numerical finite element analyses were also performed to compare and verify experimental observations and vice versa. Furthermore, this study demonstrated the usefulness and effectiveness of combining an experimental technique such as AFM imaging and indentation with numerical finite element analysis in examining the mechanical response of asphalt binder due to mechanical loading. This study establishes the significance of the ability to reduce the nucleation of damage at the microscopic level. A reduction of microscopic damage at the bitumen level would have significant implications on the resulting distresses at the pavement level. The conclusions of this study can be divided into specific categories as follows:

- The effect of tip geometry on the indentation response of a viscoelastic material.
- The effect of tensile loading on the microstructure and damaging mechanisms.
- The effect of aging on the microstructure and how aging affects the damage caused by tensile strains.
- The effect of geometry of microstructural features on the stress output of asphalt binder subjected to a axial tensile load.

6.1 Detailed Conclusions

6.1.1 The Effect of Tip Geometry on the Indentation Response of a Viscoelastic Material

To obtain a practical solution for extracting viscoelastic properties of asphalt binder a finite element model was developed to account for the finite tip radius effect on the indentation response. The cono-spherical tip geometry was incorporated into the finite element model and modification parameters were introduced to account for the differences between the spherical viscoelastic indentation solution and the finite element results. The following conclusions were drawn from the study:

- The indentation response of a cono-spherical tip indenting a relatively soft viscoelastic material was closer to the indentation response of a spherical tip rather than a conical tip as expected. However, this is contingent upon the depth of the indentation being close in magnitude to the radius of the indenter. Once the depth of indentation or the deformation of the sample reached a value much larger than radius of the cono-spherical tip, the indentation response approached that of conical tip.

- The modified viscoelastic solution was found to be suitable for analyzing creep data obtained from AFM indentation of different phases of apshalt binder. The solution was used to successfully back-calculate creep compliance parameters of two types of binders assuming a Voigt spring-dashpot viscoelastic analog model for the asphalt binder.

- The data analyzed suggested variation within the elastic (instantaneous) and time dependent (viscoelastic) responses of the different phases analyzed. In addition, the stiffnesses of the individual phases for both asphalt binder AAD and AAB consistently increased after aging. The overall stiffness of the aged phases were found to be up to three times that of the unaged phases. The analysis of the creep indentation

data demonstrated the ability of the modified viscoelastic spherical solution to quantify creep compliance parameters for different types of asphalts and different phases given the assumptions for which the solution was developed under are applicable towards the experiment performed.

6.1.2 The Effect of Tensile Loading on the Microstructure and Damaging Mechanisms

The discovery of heterogeneity within the asphalt binder by Loeber et al. [28] led to further research aiming towards the understanding of chemical and microstructural properties of asphalt binder. The existence of multiple phases present within the asphalt binder led to the speculation that these phases were related to the damaging mechanisms within asphalt binder. Kringos et al. [24] discussed the possible existence of weak interstitial zones between the bee phase and surrounding phases. They stated that the composite response of asphalt binder being subjected to mechanical loading would result in high stress zones at the boundaries of bee structures that could serve as nucleation sites for cracking and damage, assuming comparable strength between the different phases. The work in this study validates this hypothesis by combining AFM imaging and indentation techniques with finite element analysis to examine and validate the occurrence of phase separation and cracking which were designated as load induced phase separation or LIPS. The following conclusions were a direct result of this portion of our study:

- AFM phase imaging further validated the existence of multiple phases within asphalt binder which were categorized as the bee phase, bee casing phase, and interstitial phase.
- AFM creep indentation experiments were performed on two separate types of bitumens under unaged conditions. The results showed substantial difference between the compliance of different phases. This further supported the notion that inhomogenity existed not only geometrically, but also in terms of mechanical properties.

- The composite finite element simulations show that the differences in the properties among the different phases resulted in high level of stress localization.

- The application of tensile strains resulted in phase separation or cracking which were referred to as LIPS zones. The level of strain applied correlated positively with the level of cracking or phase separation observed. Both bitumen types showed consistent pattern of phase separation or cracking within the interstitial regions.

- The high stress regions observed from the finite element simulations coincided with the areas within which the LIPS zones formed. This suggested that material inhomogeneity led to the development of high stresses within the interstitial zones causing the phase separation and damage.

6.1.3 The Effect of Aging on the Microstructure and How Aging Affects the Damage Caused by High Levels of Tensile Strains

The effects of aging are significant on the mechanical properties, microstructure, and damaging mechasims of asphalt binder. In order to investigate these effects a combination of experimental and numerical techniques were combined. The geometry and the microrheology of two different asphalt binders under varying aging conditions were obtained using AFM imaging and indentation techniques. The microstructure obtained through AFM imaging was analyzed using AFM imaging techniques to detect the effect of aging and mechanical loading on the microstructure. The mechanical properties obtained were compared between the different bitumens under unaged, RTFOT aged, and RTFOT+PAV aged conditions. Using the microstructure and mechanical properties obtained finite element simulations were developed to examine the stress distribution within the asphalt binders subjected to tensile strains. The following conclusions were made from this portion of the study:

- AFM phase imaging showed the formation of LIPS zones in all six combinations of asphalt binder BI0002 (binder A) and asphalt binder AAD (binder B), which were

subjected to one percent and five percent strain. However, aged specimens exhibited significantly lower level of LIPS zone formation. This suggested that aging led to some degree of material property homogenization in the asphalt binder.

- AFM indentation experiments showed an increase in the Young's modulii of all three phases with aging. However, aging also resulted in a reduction in the differences amongst elastic modulii between the different phases. This explained why a lower level of LIPS zone formation was observed in the aged samples compared to the unaged ones, and supported the notion that aging led to homogenization of the material properties amongst the different phases. Indentation experiments also showed a decrease in the time dependent deformation among the different phases present within both asphalt binders with an increase in the level of aging.

- The composite finite element simulations showed high localized stresses within the interstitial zones and some the neighboring bee casing phases. Maximum stress ratios (highest stress/lowest stress) were observed for the unaged specimens and lowest for the RTFOT and the RTFOT+PAV aged specimens. The localized high stress zones also coincided with the formation of the LIPS zones supporting the hypothesis that the interstitial zones were primarily responsible for the nucleation of damage within asphalt binder.

6.1.4 The Effect of Geometry of Microstructural Features on the Stress Output of Asphalt Binder Subjected to a Axial Tensile Load

In Section 2 and Section 3, experimental analysis of asphalt binder samples subjected to tensile loads provided with an insight and understanding of how the geometry of the microstructural features can vary due to loading, and aging. The objective here was to determine the effect of variation within geometric parameters of microstructural features present within asphalt binder on the resulting stresses. In order to understand how the variation within ge-

ometric parameters of microstructural features present within asphalt binder can affect the output stresses, image creation techniques and numerical finite element analyses were used to carry out virtual experiments. The following conclusions were drawn from this portion of this study:

- An increase in the area fraction of the bee and bee casing feature resulted in an increase in the maximum stress ratio, increasing the probability of the formation of LIPS zones. Increasing the area fraction of the bee/bee casing feature also results in closer packing of these features.

- The packing of the bee/bee casing features affect the local stress magnitudes. Interstitial zones with high aspect ratios located longitudinally in the same direction as the loading direction resulting from close placement of bee features results in high stresses in that zone.

- Increase in the number of bee features without increasing the area fraction of the bee and the bee casing phase can result in a reduction in localized stresses in addition to the maximum stress magnitude. This occurs due to reduction of the aspect ratio of the interstitial zones between the bee features.

These findings can be used as a guideline for future work in the design of modified asphalt binders with enhanced mechanical properties, making asphalt more resistant to damage. The results of this portion of the study clearly indicate that the geometry of the microstructural features present within asphalt binder have an effect on its mechanical response. Furthermore, different aspects of the geometry studied here potentially explain how damage can be reduced in asphalt binder through modification processes. The modification of asphalt binder leading to changes in the composition and microstructure at the micron length scale can eventually lead to an enhanced pavement material with increased damage and distress resistance. This

will enable pavement engineers to design pavements with an increased design life, lower maintenance and rehabilitation cost.

6.2 Recommendations for Future Research

The work done in this study provides an insight into the complex mechanisms related to damage within asphalt binder. Here the interrelationship between asphalt binder microstructure, mechanical properties, and aging is examined in detail. However, this work leads to numerous potential areas of research that can be examined in the future, and are discussed here in detail. In addition, further improvements can be made to many aspects of this study. The potential areas of research along with the potential improvements can be divided into the following categories:

- Development of finite element indentation simulation accounting for effects of adhesion and other mechanical effects
- The formation of bee structures analyzed using experimental and numerical methods
- Improvements of creep indentation experiments using the AFM
- Improvement in sample preparation and loading frame apparatus
- Statistical analysis of data obtained through AFM imaging and indentation techniques
- Development of testing protocol for examining brittleness of asphalt binder using the AFM
- Examination of chemically modified asphalt using tensile testing and AFM techniques
- Development of a multi-scale finite element model to establish a link between micro-scale and macro-scale mechanical properties, and damage

6.3 Detailed Recommendations For Future Research

6.3.1 Development of Finite Element Indentation Simulation Accounting for Effects of Adhesion and Other Mechanical Effects

The finite element indentation model developed in this study examines the effect of modified geometry on the indentation response of soft asphaltic materials. However, numerous other factors can potentially affect on the indentation response. Adhesion is one such factor that can play a strong role in indentation experiments especially when small tips such as those used in atomic force microscopy. Numerous literary works have examined the effect of adhesion. However, very few have considered the effect of adhesion in the finite element analysis for viscoelastic materials. The inclusion of adhesion into the finite element model will provide with ability to predict mechanical properties with higher degrees of numerical accuracy, and will also help simulate more realistic indentation response.

In addtion to surface force effects, material properties play an important role on the deformation response. Asphalt binder is a time dependent material. Typically a linear viscoelastic material model is used to simulate the material behavior of asphalt binder. In this work a Voigt spring dasphot analog model is used to describe the creep compliance of asphalt binder. In reality however, the behavior asphalt binder is more accurately depicted using a nonlinear viscoelastic material model. By accounting for this nonlinearity within the viscoelastic material behavior and by defining a more accurate measure of large deformation will lead to significant improvement in the capability of the finite element model to predict the mechanical response.

6.3.2 The Formation of Bee Structures Analyzed Using Experimental and Numerical Methods

In this work the microstructure of asphalt binder was examined in detail using AFM imaging, and image analysis techniques. However, the formation of the bee structures and the

chemical and mechanical processes that lead to the formation of the bee structures remains a mystery. One hypothesis states that the change in temperature within asphalt binder during the cooling process leads to rearrangement of chemical groups present within the asphalt binder. These specific rearrangement leads to the formation of different zones of materials within asphalt binder with varying thermal expansion properties. Due to the variability in thermal expansion properties within asphalt binder a sinusoidal topographical pattern referred to as the bee structures form. A preliminary finite element analysis was performed assuming variable thermal expansion properties amongst the separate phases identified within asphalt binder. The results show that a sinusoidal topographical geometric feature similar to a single unit of a bee structure forms as the temperature of the model is reduced, which is shown in figure 6.1. Similarly, phase field modeling has the capability of predicting the formation of the complex microstructures due to the molecular interactions within a material. This can also be used to model the formation of bee structures due to the transport and rearrangement of different chemical groups within the asphalt binder. Furthermore, the implementation of an experimental procedure in order to observe the change in bitumen microstructure with respect to temperature could also be effective in determining the formation of these bee microstructures.

6.3.3 Improvements of Creep Indentation Experiments Using the Atomic Force Microscope

The creep indentation experiments performed as part of this study used an Agilent 5400 AFM. A major potential source of uncertainty within creep indentation measurements obtained using an AFM is from drift in the measurements. Drift can occur due to inherent time-dependency and heating of sensors used in the data acquisition system [16]. In order to account for the drift within the data, a zero force indentation experiment was performed. The deformation recorded was used to adjust for the drift within the creep indentation data. This led to the indentation data resulting strictly from the deformation of the sample and not the drift within the data. Furthermore, in another version of the experiment two sepa-

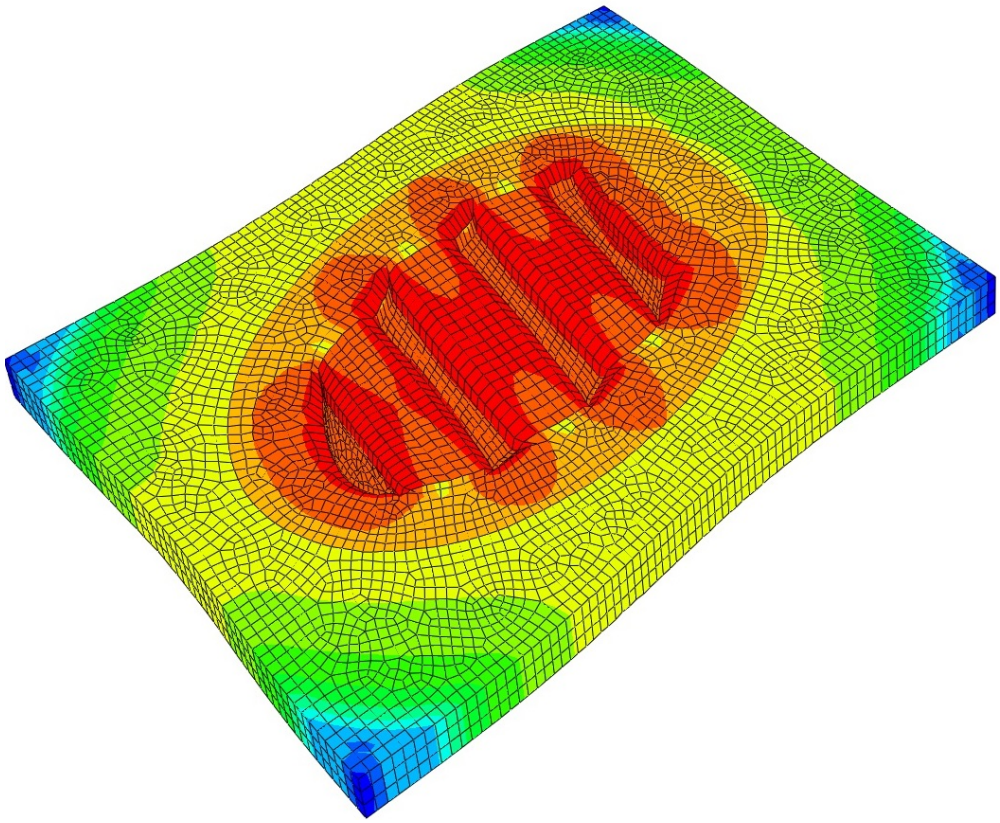

Figure 6.1: The formation of a single unit of bee structure due to thermal deformation

rate protocols were used subsequently. First, a zero force creep protocol was used. Second, this was followed by the actual creep protocol and the specific load that the material was to be subjected to. This also proved to reduce drift within the data significantly. For further validation of material properties determined using the creep indentation method, AFM creep experiments must be performed on different AFM machines to test for consistency in data measurement. Modern AFM machines such as the Brucker Icon AFM are less prone to drift and noise within the experimental data. Furthermore, a specific type of AFM uses a nanoindenter in conjunction with an imaging tip to carry out indentation measurements. This type of AFM can be used to simultaneously image and indent the surface of a sample without having to use the sharp imaging tip as the indentation device. By using this procedure the use of a sharp AFM imaging tip to perform indentation experiments can be avoided, and perhaps will lead to an improvement in the numerical accuracy of the back-calculation of material properties due to already well established solutions for the bigger nanoindenter tips such as the cube corner or spherical tips.

6.3.4 Improvement in Sample Preparation and Loading Frame Apparatus

The preparation of asphalt binder samples in this study used a hot melt casting approach as opposed to the more common solvent casting method typically used for testing thin samples. The use of this hot melt casting method proved to be troublesome due to the lack of a hot melt spin coater. The spin coating process is effective in removing any surface irregularities and provides with an even surface useful for AFM imaging and indentation experiments. Scanning the surface of an uneven sample with large scan areas such as the ones used in this study (50 μm by 50 μm) can be challenging if irregularities within the surface topography is present. Specifically, the surface of the sample must be smooth at the scale the image is obtained. Overcoming these issues will result in higher number of successful experimental trials leading a bigger size of sample data resulting in improved statistical accuracy.

Furthermore, asphalt is a very strong adhesive. In order to prepare the asphalt binder

specimen a thin film of plastic or Aluminum was placed on top of the mold to separate the asphalt binder from the mold. The transport of the specimen from the mold to the loading frame proved to be quite troubling due to possible disturbances during the removal of the sample from the mold. Numerous experimental trials were required just to obtain one set of experimental data due to these issues. Improvement in these areas will also result in a more robust experimental technique resulting in larger number of experimental trials within a given time, and a higher amount of statistical information regarding the microstructure being examined.

One approach to improve the testing apparatus would be to design a loading frame which is capable of withstanding high temperature so when the asphalt binder is placed on top and melted it no longer needs to be transported after the cool-down process. In addition, the attachment of a measurement caliper to the loading frame will also provide with a more robust measuring technique for the sample dimensions before and after a certain level of strain is applied.

The aforementioned techniques are all aspects that will provide with significance improvement in the ability to perform experimental procedures used in this work in a timely manner and with lower experimental uncertainty.

6.3.5 Statistical Analysis of Data Obtained through Afm Imaging and Indentation Techniques

The statistical analysis presented in appendix A establishes differences within data obtained regarding the microstructure for different binders. The relative frequency histogram provides with a distribution of bee areas. Through image analysis other geometric measures such as the orientation, perimeter, aspect ratio can also be obtained. Statistical analysis of other geometric parameters may provide with additional insight into the microstructure change occurring due to tensile strains and aging. One aspect of particular interest could be the orientation of the individual bee structures and how they are affected by loading. In

addition, the aspect ratios of the bee structures are most likely also affected by external mechanical loads. Statistical analysis of these geometric features could provide further evidence of microstructural changes in asphalt binder due to aging, mechanical loading, and other factors that have not been considered in this study.

6.3.6 Development of Testing Protocol for Examining Brittleness of Asphalt Using the AFM

In this study bitumen samples were subjected to tensile strains using a micro-loading frame and the resulting changes in microstructure were examined using an AFM. Aging has been known to increase asphalt binder brittleness leading to a higher susceptibility to damage and cracking. In this work finite amount of tensile strain was applied to different bitumen samples under various aging conditions. The microstructure of the asphalt binder was imaged before and after the application of strain and the the resulting differences were analyzed. The results indicated that an increase in aging resulted in lower extent of cracking or damage. These findings could easily be misinterpreted to assume that aging results in a decrease in the brittleness of asphalt binder. Although the experimental procedure in this study examines the effect of tensile strains on the microstructure of asphalt binder, it is not an effective measure of brittleness. In order to test the brittleness, an alternate testing procedure can be used which subjects the asphalt binder to impact. As mentioned in a previous section, an AFM technique which combines a nanoindenter with an AFM imaging tip can be used to apply an impact load to the specimen. A typical type of indenter used for nanoindentation experiments is the cube corner indenter. The use of a this indenter would result in crack initiation in locations where the sharp edges of the cube corner would make contact with the material. By applying the same indentation force on different asphalt binder samples under unaged, and aged conditions the difference between the crack sizes can be measured using AFM imaging techniques, which could then be used as an experimental measure for the quantification of brittleness of asphalt binder.

6.3.7 Examination of Chemically Modified Asphalt Using Tensile Testing and AFM Techniques

One of the main contributions of this study is to establish a methodology to examine the microstructure and how its affected by external factors such as mechanical loading and aging at a small scale. In this study this methodology was applied towards unaged and aged non-modified asphalt binders. Modification of asphalt in order to enhance its mechanical properties and make it more resistant to damage has become a popular engineering practice. Some modifiers of particular interest would be polymers such as elastomers and plastomers, rejuvinating and recycling agents. However, fundamental understanding of how asphalt modification can potentially lead to change in mechanical, and damage related properties is still a topic of major research. The methodology established in this work can easily be applied to modified asphalt binders. The AFM has already proven to be extremely effective at analyzing microstructural changes along with determining microscale mechanical properties within asphalt binder. In addition, micro-tensile testing apparatus developed in this work can be used to study the effect of mechanical stimuli on the microstructure of modified asphalt binders. In addition, through finite element analysis the modified asphalt binder can also be modeled as by considering the nonlinear elasticity, and plasticity exhibited by elastomers and plastomers. The numerical analysis will also provide with an effective validation tool for experimental observations.

6.3.8 Development of a Multi-Scale Finite Element Model to Establish a Link between Micro-Scale and Macro-Scale Mechanical Properties, and the Propagation of Damage

In recent years multiscale modeling has become an effective tool for determining the macroscale response of materials that exhibit heterogeneity at the microscale [1]. Teixira et al. [55] used the multiscale modeling approach to describe asphalt as a multiphase composite

material. They implemented a two-way model where the local material behavior affected the global material behavior and vice versa. This has proved to be a very effective method for linking the behavior of asphalt between different scales (see figure 6.2).

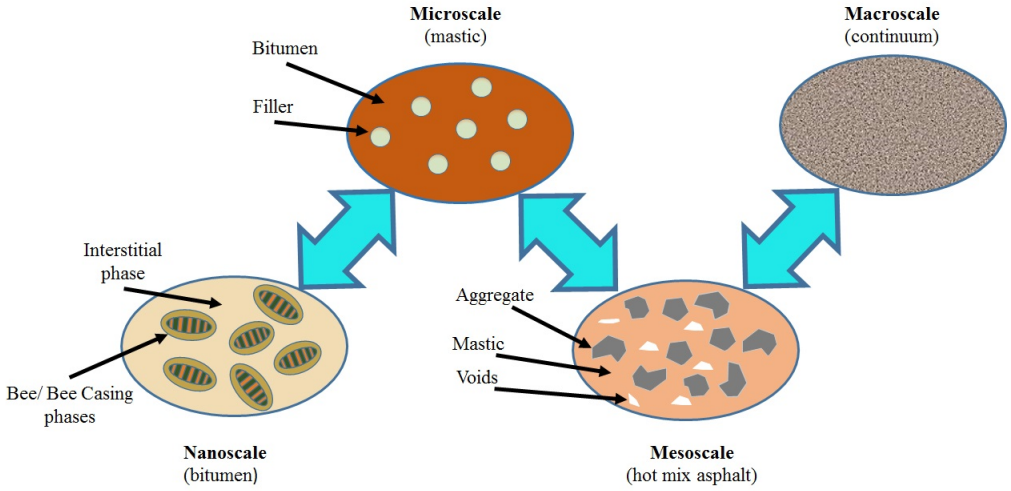

Figure 6.2: Multiscale model for asphalt

However, the multiscale modeling approach has not been used to to establish the link between the microstructural properties established in this work and the macro-scale hot mix asphalt behavior. This could potentially become a very interesting topic to explore. Experimental observations in this study clearly suggest that the development of the load induced phase separation zones are related to the microstructural arrangement within the asphalt binder. Microcracks nucleating in the asphalt binder at the nanometer/micrometer length scale will lead to the eventual coalescence and formation of larger macrocracks. The multiscale modeling can be used to examine this behavior and establish how the microcracks can develop into larger macrocracks in the hot mix asphalt. In addition, the multiscale modeling approach can be used to not only account for the damage initiation at the binder level, but also study the contribution of damage from different components present within the hot mix asphalt,

specifically the aggregate, and the binder.

REFERENCES

[1] D. H. Allen and R. F. Soares. Multiscale modeling of the evolution of damage in heterogeneous viscoelastic solids. In Young W. Kwon, David H. Allen, and Ramesh Talreja, editors, *Multiscale Modeling and Simulation of Composite Materials and Structures*, pages 495–527. Springer US, 2008.

[2] R. Allen. *Microstructural Characterization Of The Chemomechanical Behavior Of Asphalt In Terms Of Aging And Fatigue Performance Properties*. PhD dissertation, Texas A&M University, College Station, 2013.

[3] R. Allen, D. N. Little, A. Bhasin, and C. J. Glover. The effects of chemical composition on asphalt microstructure and their association to pavement performance. *International Journal of Pavement Engineering*, 15:9–22, 2014.

[4] R. Allen, D.N. Little, and A. Bhasin. Structural characterization of micromechanical properties in asphalt using atomic force microscopy. *Journal of Materials in Civil Engineering*, 24:1317–1327, 2012.

[5] N. A. Burnham and R. J. Colton. Measuring the nanomechanical properties and surface forces of materials using an atomic force microscope. *Journal of Vacuum Science and Technology*, 7:2906–2913, 1989.

[6] N. A. Burnham, D. D. Dominguez, R. L. Mowery, and R. J. Colton. Probing the surface forces of monolayer films with an atomic-force microscope. *Physical Review Letters*, 64:1931–1934, 1989.

[7] S. Cho and S. Park. Finite element modeling of adhesive contact using molecular potential. *Tribology International*, 37(9):763–769, 2004.

[8] Q. Dai. Two- and three-dimensional micromechanical viscoelastic finite element modeling of stone-based materials with x-ray computed tomography images. *Construction and Building Materials*, 2010.

[9] P. K. Das, N. Kringos, V. Wallqvist, and B. Birgisson. Micromechanical investigation of phase separation in bitumen by combining atomic force microscopy with differential scanning calorimetry results. *Road Materials and Pavement Design*, 14:25–37, 2013.

[10] E. R. Dourado, R. A. Simao, and L. F. M. Leite. Mechanical properties of asphalt binders evaluated by atomic force microscopy. *Journal of Microscopy*, 245:119–128, 2011.

[11] B. Du, O.K.C. Tsui, and T. He. Study of elastic modulus and yield strength of polymer thin films using atomic force microscopy. *Langmuir*, 17:3286–3291, 2001.

[12] C. Eberl, R. Spolenak, E. Arzt, F. Kubat, A. Leidl, W. Rulie, and O. Kraft. Ultra high-cycle fatigue in pure al films and line structures. *Materials Science and Engineering*, 421:68–76, 2006.

[13] A. C. Fischer-Cripps. A simple phenomenological approach to nanoindentation creep. *CSIRO Division of telecommunications and Industrial Physics*, 385:74–82, 2004.

[14] L. A. Galin. *Contact Problems in Theory of Elasticity*. Moscow, Gostekhizdat, 1953.

[15] J. E. Gentle. *Random number generation and Monte Carlo Methods*. Springer-Veriag New York, 2003.

[16] Z. C. Grasley, C. A. Jones, and M. Benhalima. Extracting viscoelastic properties of nanometric phases using atomic force microscopy. In *4th International Symposium on Nanotechnology in Construction*, 2012.

[17] H. Hertz. Translated and reprinted in english in "hertz's miscellaneous papers". *Verhandlungen des Vereins zur Beforderung des Gewerbe Fleisses*, 61:410, 1882.

[18] H. Hertz. Translated and reprinted in english "hertz's miscellaneous papers". *J. Reine Angew. Math*, 92:156, 1896.

[19] Y. H. Huang. *Pavement Analysis and Design*. Prentice Hall, 2004.

[20] A. Jager, R. Lackner, C. Eisenmenger-Sittner, and R. Blab. Identification of microstructural components of bitumen by mean of atomic force microscopy (afm). volume 4,

pages 400–401, 2004.

[21] R. Jahangir, D. Little, and A. Bhasin. Evolution of asphalt binder microstructure due to tensile loading determined using afm and image analysis techniques. *International Journal of Pavement Engineering*, 16(4):337–349, 2015.

[22] C. A. Jones and Z. C. Grasley. Short-term creep of cement paste during nanoindentation. *Cement and Concrete Composites*, 33(1):12–18, January 2011.

[23] D. R. Jones and T. W. Kennedy. The asphalt model: Results of the shrp asphalt research program. Technical report, Center for Transportation Research, The University of Texas at Austin, Austin TX, 1992.

[24] N. Kringos, A. Schmets, T. Pauli, and T. Scarpas. A finite element based chemo-mechanical model to simulate healing of bitumen. In *Group of Mechanics of Infrastructure Materials*, 2009.

[25] K. P. Larsen, A. A. Rasmussen, J. T. Ravnkilde, M. Ginnerup, and O. Hansen. Mems device for bending test: measurements of fatigue and creep of electroplated nickel. *Sensors and Actuators A*, 103:156–164, 2003.

[26] E. H. Lee and J. R. M. Radok. The contact problem for viscoelastic bodies. *Journal of Applied Mechanics- Transactions of the ASME 1960*, 27:438–44, 1960.

[27] L. Loeber, G. Muller, J. Morel, and O. Sutton. Bitumen in colloid science: a chemical, structural and rheological approach. *Fuel*, 77(13):1443–1450, 1998.

[28] L. Loeber, O. Sutton, J. Morel, J.-M. Valleton, and G. Muller. New direct observations of asphalts and asphalt binders by scanning electron microscopy and atomic force microscopy. *Journal of Microscopy*, 182:32–39, 1996.

[29] A. Maher and T. Bennert. Evaluation of poisson's ratio for use in the mechanistic empirical pavement design guide (mepdg). Technical report, Rutgers, 2008.

[30] C. M. Marek and M. Herrin. Tensile behavior and failure characteristics of asphalt cements in thin films. *Proceedings Of The Association Of Asphalt Paving Technologists*,

37:386–421, 1958.

[31] E. Masad, N. Somadevan, H.U. Bahia, and S. Kose. Modeling and experimental measurements of strain distribution in asphalt mixes. *Journal of Transportation Engineering*, 127(6):477–485, 2001.

[32] E.A. Masad and N. Somadevan. Microstructural finite-element analysis of influence of localized strain distribution on asphalt mix properties. *Journal of Engineering Mechanics*, 127(6):1105–14, 2002.

[33] J. F. Masson, V. leblond, and J. Margeson. Bitumen morphologies by phase-detection atomic force microscopy. *Journal of Microscopy*, 221(1):17–29, 2005.

[34] J.F. Masson, V. Leblond, and J. Margeson. Low-temperature bitumen stiffness and viscous paraffinic nano- and micro-domains by cryogenic afm and pdm. *Journal of Microscopy*, 227(3):191–202, 2007.

[35] L. T. Mo, M. Huurman, S. P. Wu, and A. A. A. Molenaar. 2d and 3d meso-scale finite element models for ravelling analysis of porous asphalt concrete. *Finite Elements in Analysis and Design*, 44:186–196, 2008.

[36] R. Modlinski, A. Witvrouw, P. Ratchev, A. Jourdain, V. Simons, H. A. C. Tilmans, J. M. J. Toonder, R. Puers, and I. De Wolf. Creep as reliability problem in mems. *Microelectronics Reliability*, 44:1733–1738, 2004.

[37] M. Mortavazi and J.S. Moulthrop. The shrp materials reference library. Technical report, The Strategic High Research Program, 1993.

[38] W.C. Oliver and G. M. Pharr. Measurement of hardness and elastic modulus by instrumented indentation : Advances in understanding and refinements to methodology. *Journal of Materials Research*, 19:3–20, 2004.

[39] W.C. Oliver and G.M. Pharr. An improved technique for determining hardness and elastic modulus using load and displacement sensing indentation experiments. *Journal of Materials Research*, 7(06):1564–1583, January 2011.

[40] J. H. Park, Y. J. Kim, and S. H. Choa. Mechanical properties of al-3of rf mems switch. *Key Engineering Materials*, 306-308:1319–1324, 2006.

[41] N. Paryab, H. Jahed, and A. Khajepour. Failure mechanisms of mems thermal actuators. In *Proceedings of the AME IMECE*, 2006.

[42] A. T. Pauli, J. F. Brandthaver, R. E. Robertson, and W. Grimes. Atomic force microscopy investigation of shrp asphalts. *Symposium on Heavy Oil and Resid Compatiblity and Stability*, pages 110–114, 2001.

[43] A. T. Pauli and R. W. Grimes. Surface morphological stability modeling of shrp asphalts. *ACS Division of Fuel Chemistry Preprints*, 1:19–23, 2003.

[44] A. T. Pauli, R. W. Grimes, A. G. Beemer, T. F. Turner, and J. F. Branthaver. Morphology of asphalts, asphalt fractions and model wax-doped asphalts studied by atomic force microscopy. *International Journal of Pavement Engineering*, 12:4:291–309, 2011.

[45] J. P. H. Pfeiffer and R. N. J. Saal. Asphaltic bitumen as a colloid system. *Journal of Physical Chemistry*, 44:139–149, 1940.

[46] B. Poon, D. Rittel, and G. Ravichandran. An analysis of nanoindentation in linearly elastic solids. *International Journal of Solids and Structures*, 45(24):6018–6033, 2008.

[47] L. D. Poulikakos and M. N. Partl. Micro scale tensile behaviour of thin bitumen films. *Experimental Mechanics*, 51:1171–1183, 2011.

[48] L.M. Rebelo, J.S. de Sousa, A.S. Abreu, M.P.M.A. Baroni, A.E.V. Alencar, S.A. Soares, J. M. Filho, and J.B. Soares. Aging of asphaltic binders investigated with atomic force microscopy. *Fuel*, 117, Part A(0):15 – 25, 2014.

[49] C. Reynaud, F. Sommer, C. quet, N. El Bounia, and T. Minh Duc. Quantitative determination of young's modulus on a biphase polymer ystem using atomic force microscopy. *Surface and Interface Analysis*, 30:185–189, 2000.

[50] F. L. Roberts, P. S. Kandhal, E.R. Brown, D.-Y. Lee, and T. W. Kennedy. Hot mix asphalt materails, mixture design and construction. Technical report, National Asphalt

Pavement Association Research and Education Foundation, Lanham, MD, 1996.

[51] I. Sneddon. The relation between load and penetration in the axisymmetric boussinesq problem for a punch of arbitrary profile. *International Journal of Engineering Science*, 3(638):47–57, 1965.

[52] A. B. Sontheimer. Digital micromirror device (dmd) hinge memory lifetime reliability modeling. In *Proceedings of IEEE international Reliability Physics Symposium*, 2002.

[53] S. Sultana, A. Bhasin, and K. M. Liechti. Rate and confinement effects on the tensile strength of asphalt binder. *Construction and Building Materials*, 53:604–611, 2014.

[54] R. A. Tarefder, A. M. Zaman, and W. Uddin. Determining hardness and elastic modulus of asphalt nanoindentation. *International Journal of Geometchanics*, 10:106–116, 2010.

[55] J. Teixeira, Y.-R. Kim, F. Souza, D. Allen, and D. Little. Multiscale model for asphalt mixtures subjected to cracking and viscoelastic deformation. *Transportation Research Record: Journal of the Transportation Research Board*, 2447:136–145, 2014.

[56] K. Tuck, A. Jugen, A. geisberger, M. Ellis, and G. Skidmore. A study of creep in polysilicon mems devices. *Journal of Engineering Materials and Technology*, 127:90–96, 2005.

[57] M. Vandamme and F. Ulm. Viscoelastic solutions for conical indentation. *International Journal of Solids and Structures*, 43(10):3142–3165, 2006.

[58] A. S. Wineman and K. R. Rajagopal. *Mechanical Response of Polymers An Introduction*. Cambridge University Press, 2000.

[59] T. You, R. K. Abu Al-Rub, M. K. Darabi, E. A. Masad, and D. N. Little. Three-dimensional microstructural modeling of asphalt concrete using a unified viscoelastic-viscoplastic-viscodamage model. *Construction and Building Materials*, 28:531–548, 2011.

[60] X. Zhang, X. Zhang, and S. Wen. Finite Element Modeling of the Nano-scale Adhesive Contact and the Geometry-based Pull-off Force. *Tribology Letters*, 41(1):65–72, 2010.

APPENDIX A

STATISTICAL ANALYSIS

The data used to support the findings of this study describes the distribution of microstructural phases within asphalt binder, and also its mechanical properties. In order obtain the microstructural distribution AFM images of the surface of the asphalt binder for asphalt binders AAD and BI0002 under various aging conditions are analyzed using image analysis software ImageJ. The mechanical properties for each phase of the different samples were obtained through AFM creep indentation experiments where a constant load is applied thorugh the AFM tip, and the resulting deformation is recorded. Evidence from the various studies presented in Section 3 and Section 4 suggest that microstructural changes occur due to the application of tensile strains. In addition, when a sample is aged using specified aging protocols and subjected to tensile strains microstructural changes are also observed specifically in the phase referred to as the "bee" phases. An individual component of the "bee" phase is referred to as the "bee" structure. Here statistical analysis will be performed for the changes in the area of bee structures before, and after loading which are subjected to unaged, RTFOT aged, and RTFOT+PAV aged asphalt binder samples. All statistical calculations presented in this appendix were performed using JMP 11.2 Pro statistical software. The following statistical methods were used in the analysis:

- Relative frequency histograms and normal probability (q-q) plots to test for distribution and normality of both microstructural analysis and creep measurements.
- Distribution that ideally describes the data and distribution fit parameters.
- Design of experiment one sample mean analysis is performed to determine the power of the sample mean to detect a significant difference in area of bee structure based on

microstructural analysis.

- Wilcoxon/Kruskal Wallis rank tests to compare means of individual bee structure area for different asphalt binders under various aging and load conditions.
- Coefficient of variation calculation for creep indentation measurements of different phases.

A.1 Stastistical Analysis of Asphalt Binder Microstructure Obtained through Afm Imaging

In Section 3 asphalt binder BI0002 and AAD which were referred to as binder A and B were subjected to tensile strains of one percent, and five percent. AFM phase images of the different samples were obtained which enabled the analysis of the bee phase. Here individual bee structure distributions are analyzed. For each sample four AFM scans of 50 μm by 50 μm were taken. The sample population analyzed here was a combination of all data obtained within the four images.

A.1.1 Relative Frequency and Distribution of Bee Phases

Figure A.1 display distribution of bee structures before and application of tensile strains for asphalt binder AAD under unaged conditions. The data was observed to be positively skewed and the highest frequency of bee structures were observed to be have between 0 and 2.5 μm^2 area. The mean and the standard deviation with increased level of tensile strains was clearly observed to decrease from 5.30 to 5.12 for the mean, and 7.04 to 4.21 for the standard deviation. This suggested the variance within the data reduced with the application of strain. In Section 3 it was discussed that the tensile strains led to not only the formation of the LIPS zones but also flattening and dissipation of bee structures. The data seen in figure A.1 also shows a reduction in the interquartile range from 7.44 to 3.59, which suggests a reduction in the spread of the areas of the bee structures. The data shown also suggests non-normality with the lower bound being zero and high level of positive skewness. This will be further

Distributions TYPE=AAD UNAGED BEFORE

AREA

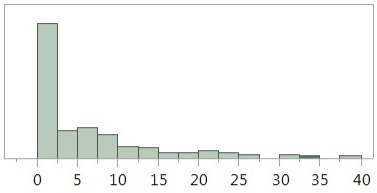

Quantiles		
100.0%	maximum	37.575
99.5%		34.9808
97.5%		26.15
90.0%		14.572
75.0%	quartile	7.782
50.0%	median	2.136
25.0%	quartile	0.343
10.0%		0.076
2.5%		0.038
0.5%		0.038
0.0%	minimum	0.038

Summary Statistics	
Mean	5.3051816
Std Dev	7.0393367
Std Err Mean	0.3664532
Upper 95% Mea	6.0257867
Lower 95% Mean	4.5845765
N	369

Distributions TYPE=AAD UNAGED ONE PERCENT STRAIN

AREA

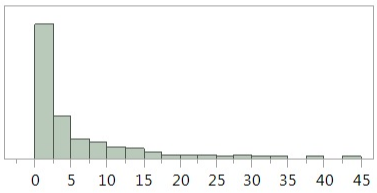

Quantiles		
100.0%	maximum	42.648
99.5%		40.6225
97.5%		27.5497
90.0%		13.9848
75.0%	quartile	7.191
50.0%	median	2.098
25.0%	quartile	0.61
10.0%		0.2214
2.5%		0.038
0.5%		0.038
0.0%	minimum	0.038

Summary Statistics	
Mean	5.1282808
Std Dev	7.0885313
Std Err Mean	0.3981316
Upper 95% Mea	5.9116045
Lower 95% Mean	4.3449571
N	317

Distributions TYPE=AAD UNAGED FIVE PERCENT STRAIN

AREA

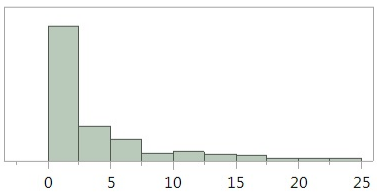

Quantiles		
100.0%	maximum	24.109
99.5%		23.1483
97.5%		16.289
90.0%		9.5481
75.0%	quartile	4.082
50.0%	median	1.4495
25.0%	quartile	0.496
10.0%		0.153
2.5%		0.038
0.5%		0.038
0.0%	minimum	0.038

Summary Statistics	
Mean	3.1940919
Std Dev	4.2182415
Std Err Mean	0.2557685
Upper 95% Mea	3.6976377
Lower 95% Mean	2.6905461
N	272

Figure A.1: Distribution of bee structures before and after application of tensile strains for asphalt binder AAD under unaged condition

examined using q-q plots.

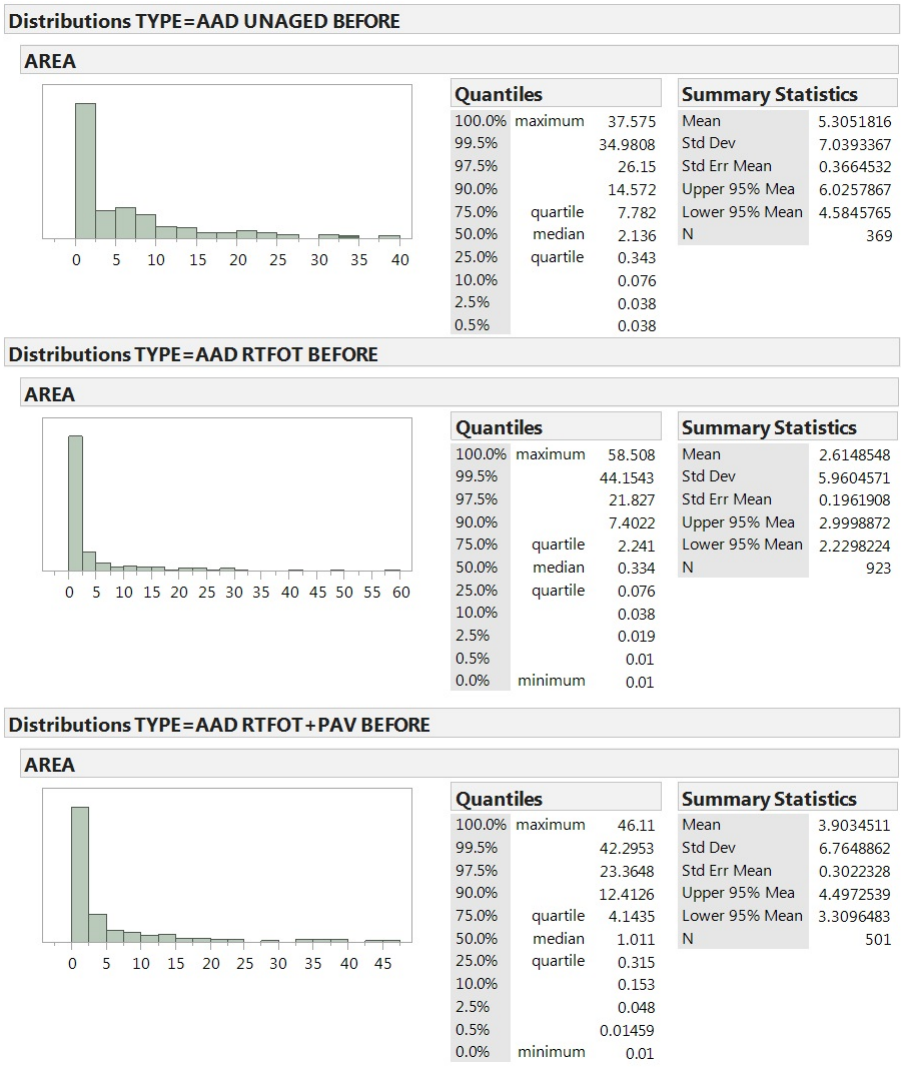

Figure A.2: Distribution of bee structures for asphalt binder AAD under different aging conditions

Figure A.2 show the distribution of bee structures under different aging conditions before the application of tensile strains. Here, a reduction in the mean value is observed for the for asphalt binder AAD between the unaged and RTFOT aged condition. However, a slight increase in the mean value of the bee structures is observed when the apshalt binder is further

aged using the PAV aging protocol. Although this does not show clear trend between the RTFOT and the RTFOT+PAV aging condition, there is clearly a reduction in the mean area for both the RTFOT and the RTFOT+PAV aged samples when compared to the unaged sample population.

Figure A.3: Distribution of bee structures before and after application of tensile strains for asphalt binder AAD under RTFOT aging condition

Distributions TYPE=AAD RTFOT+PAV BEFORE

AREA

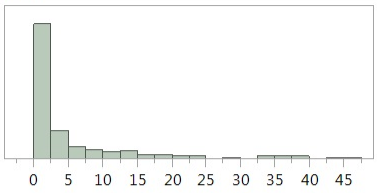

Quantiles		
100.0%	maximum	46.11
99.5%		42.2953
97.5%		23.3648
90.0%		12.4126
75.0%	quartile	4.1435
50.0%	median	1.011
25.0%	quartile	0.315
10.0%		0.153
2.5%		0.048
0.5%		0.01459
0.0%	minimum	0.01

Summary Statistics	
Mean	3.9034511
Std Dev	6.7648862
Std Err Mean	0.3022328
Upper 95% Mea	4.4972539
Lower 95% Mean	3.3096483
N	501

Distributions TYPE=AAD RTFOT+PAV ONE PERCENT

AREA

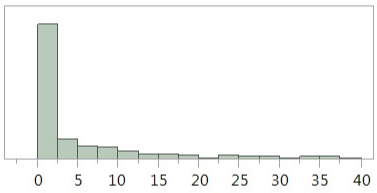

Quantiles		
100.0%	maximum	39.778
99.5%		35.944
97.5%		24.9438
90.0%		11.6255
75.0%	quartile	4.442
50.0%	median	0.82
25.0%	quartile	0.286
10.0%		0.114
2.5%		0.02775
0.5%		0.01
0.0%	minimum	0.01

Summary Statistics	
Mean	3.8365401
Std Dev	6.4957097
Std Err Mean	0.2983578
Upper 95% Mea	4.4228108
Lower 95% Mean	3.2502693
N	474

Distributions TYPE=AAD RTFOT+PAV FIVE PERCENT

AREA

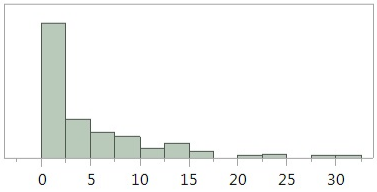

Quantiles		
100.0%	maximum	31.166
99.5%		30.4775
97.5%		19.9255
90.0%		12.3132
75.0%	quartile	6.55625
50.0%	median	2.1505
25.0%	quartile	0.45075
10.0%		0.1397
2.5%		0.038
0.5%		0.019
0.0%	minimum	0.019

Summary Statistics	
Mean	4.3154362
Std Dev	5.3688503
Std Err Mean	0.3197104
Upper 95% Mea	4.9447675
Lower 95% Mean	3.6861048
N	282

Figure A.4: Distribution of bee structures before and after application of tensile strains for asphalt binder AAD under RTFOT+PAV aging condition

Figure A.3 show the distribution of bee structures under RTFOT aging conditions for different levels of applied tensile strains. Here, very similar mean area for the bee structures are observed between the undisturbed sample data and the sample data for the one percent tensile strain. However, when comparing the sample mean of binder AAD under RTFOT aging condition subjected to five percent tensile strain a clear reduction in the mean area is observed. Similarly although there was a slight increase in the standard deviation between the undisturbed and the one percent strain sample populations, there seems to be a clear reduction in the sample standard distribution between the undisturbed and the sample population for the binder subjected to five percent tensile strains. A reduction in the interquartile range between the undisturbed and the sample population for the binder subjected to five percent from 2.17 to 1.31 suggests a reduction in the spread of the majority of the population of interest. Figure A.4 also exhibits a reduction in the standard deviation of the sample population between the undisturbed and the samples subjected to tensile strains. However, although the mean areas for all three loading conditions were found to be very similar a slight increase in the mean area was observed between the undisturbed, one percent strain, and the five percent strain. This suggests that the sample the tensile strains leading to positive shift in the mean population possibly through a higher dissipation of the small bee structures compared to the large bee structures. This observation is reinforced by the change in the quantile values of the bee structure areas between the undisturbed and the sample population subjected to five percent strains. The first quartile value for the undisturbed sample data was found to be 0.32, which showed an increase to a value of 0.45 for the sample data subjected to five percent tensile strains.

Figure A.5 display distribution of bee structures before and application of tensile strains for asphalt binder BI0002 under unaged conditions. The mean bee structure size shows slight variation between the different strain levels. The standard deviation within the sample populations also show less variation compared to the statistical change in the mean areas of asphalt

Distributions GROUP=BI0002 UNAGED BEFORE

AREA

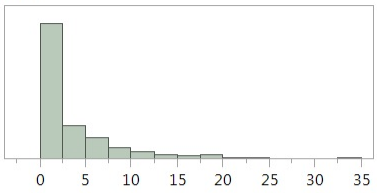

Quantiles		
100.0%	maximum	34.447
99.5%		19.8178
97.5%		15.1902
90.0%		8.0012
75.0%	quartile	3.996
50.0%	median	1.307
25.0%	quartile	0.191
10.0%		0.057
2.5%		0.019
0.5%		0.01
0.0%	minimum	0.01

Summary Statistics	
Mean	2.8788156
Std Dev	4.0059423
Std Err Mean	0.1469638
Upper 95% Mea	3.1673299
Lower 95% Mean	2.5903013
N	743

Distributions GROUP=BI0002 UNAGED ONE PERCENT

AREA

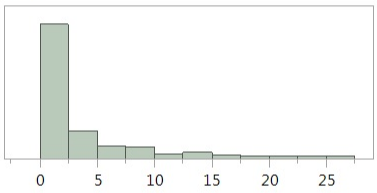

Quantiles		
100.0%	maximum	27.132
99.5%		26.413
97.5%		16.0395
90.0%		8.5995
75.0%	quartile	3.65525
50.0%	median	0.9345
25.0%	quartile	0.2075
10.0%		0.067
2.5%		0.02575
0.5%		0.01
0.0%	minimum	0.01

Summary Statistics	
Mean	2.9131672
Std Dev	4.4290897
Std Err Mean	0.182964
Upper 95% Mea	3.2725136
Lower 95% Mean	2.5538209
N	586

Distributions GROUP=BI0002 UNAGED FIVE PERCENT

AREA

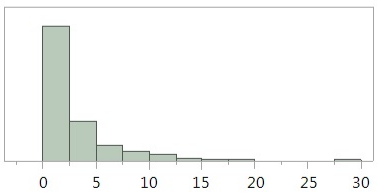

Quantiles		
100.0%	maximum	28.448
99.5%		17.2026
97.5%		11.7243
90.0%		6.3881
75.0%	quartile	3.40975
50.0%	median	1.392
25.0%	quartile	0.439
10.0%		0.172
2.5%		0.067
0.5%		0.0331
0.0%	minimum	0.019

Summary Statistics	
Mean	2.5211122
Std Dev	3.1493342
Std Err Mean	0.1422724
Upper 95% Mea	2.8006529
Lower 95% Mean	2.2415715
N	490

Figure A.5: Distribution of bee structures before and after application of tensile strains for asphalt binder BI0002 under unaged condition

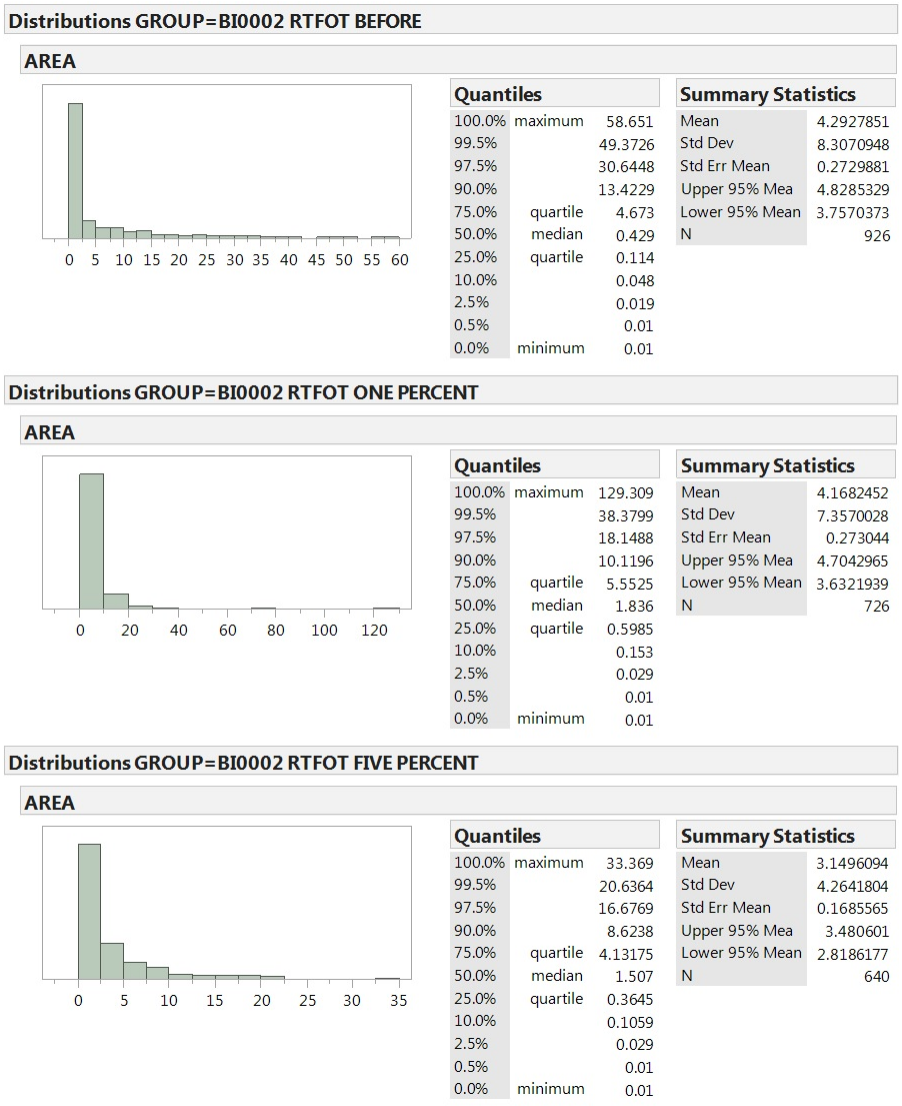

Figure A.6: Distribution of bee structures before and after application of tensile strains for asphalt binder BI0002 under RTFOT aging condition

binder AAD. Overall, only a slight decrease in the mean area was observed from a value of 2.87 for the unaged sample population, to a value of 2.52 for the sample poplution for the binder subjected to five percent tensile strains. Figure A.6 also exhibit slight reduction in the mean area an increase in the level of applied tensile strains. The standard deviation also exhibits a reduction with an increase in the tensile strains. This means that an increase in loading led to a decrease in the variability of the bee structure areas for the sample populations. A similar trend was observed for asphalt binder AAD. Again, it is important to note the reduction in the standard deviation is low compared between the undisturbed and the one percent tensile strain sample population comapred the the reduction in the standard deviation between the undisturbed and the five percent tensile strain sample population. Hence, It can be concluded that increasing levels of tensile strains leads to a lower variability of the mean area of the bee structures, which possibly occurs due to dissipation of smaller bee structures and flattening of the larger bee structures as discussed in Section 3. Figure A.7 displays similar trends in the mean and standard deviation of the areas of bee structures.

Figure A.8 show the distribution of bee structures under different aging conditions before the application of tensile strains. Here, we observe a clear trend in the change of the mean bee structure size. With an increase in the aging level the mean bee structure size of the sample population increases. The standard deviation for both the RTFOT aged, and the RTFOT+PAV aged sample populations also are higher than the standard deviation of the unaged sample population. This suggests that aging leads to an increase in the spread or the variability within the areas of the bee structures. The interquartile range also demonstrates a similar trend.

A.1.2 Non-Normality Analysis of Bee Structure Distribution

Figures A.9 and A.10 show q-q plots for both asphalt binder AAD, and BI0002 respectively under different aging conditions. The data clearly suggests the distribution of the bee structure areas show significant non-normality exhibited by the deviation of the data from the

Distributions GROUP=BI0002 RTFOT+PAV BEFORE

AREA

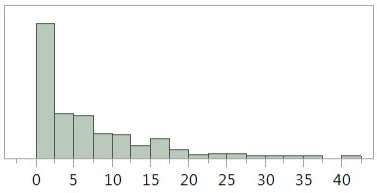

Quantiles		
100.0%	maximum	41.485
99.5%		34.7472
97.5%		25.6932
90.0%		16.5126
75.0%	quartile	9.489
50.0%	median	3.977
25.0%	quartile	0.6555
10.0%		0.1367
2.5%		0.048
0.5%		0.01374
0.0%	minimum	0.01

Summary Statistics	
Mean	6.3151867
Std Dev	7.0404449
Std Err Mean	0.3206835
Upper 95% Mea	6.9453003
Lower 95% Mean	5.6850731
N	482

Distributions GROUP=BI0002 RTFOT+PAV ONE PERCENT

AREA

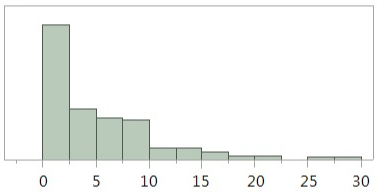

Quantiles		
100.0%	maximum	28.267
99.5%		26.4313
97.5%		17.0673
90.0%		11.4825
75.0%	quartile	7.372
50.0%	median	3.166
25.0%	quartile	0.75825
10.0%		0.1
2.5%		0.02275
0.5%		0.01
0.0%	minimum	0.01

Summary Statistics	
Mean	4.7009465
Std Dev	4.8755475
Std Err Mean	0.2521086
Upper 95% Mea	5.1966787
Lower 95% Mean	4.2052143
N	374

Distributions GROUP=BI0002 RTFOT+PAV FIVE PERCENT

AREA

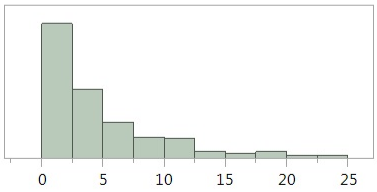

Quantiles		
100.0%	maximum	24.49
99.5%		21.3611
97.5%		16.6463
90.0%		10.405
75.0%	quartile	6.0415
50.0%	median	2.89
25.0%	quartile	0.7675
10.0%		0.21
2.5%		0.0405
0.5%		0.01
0.0%	minimum	0.01

Summary Statistics	
Mean	4.2134065
Std Dev	4.3893273
Std Err Mean	0.2284993
Upper 95% Mea	4.6627346
Lower 95% Mean	3.7640784
N	369

Figure A.7: Distribution of bee structures before and after application of tensile strains for asphalt binder BI0002 under RTFOT+PAV aging condition

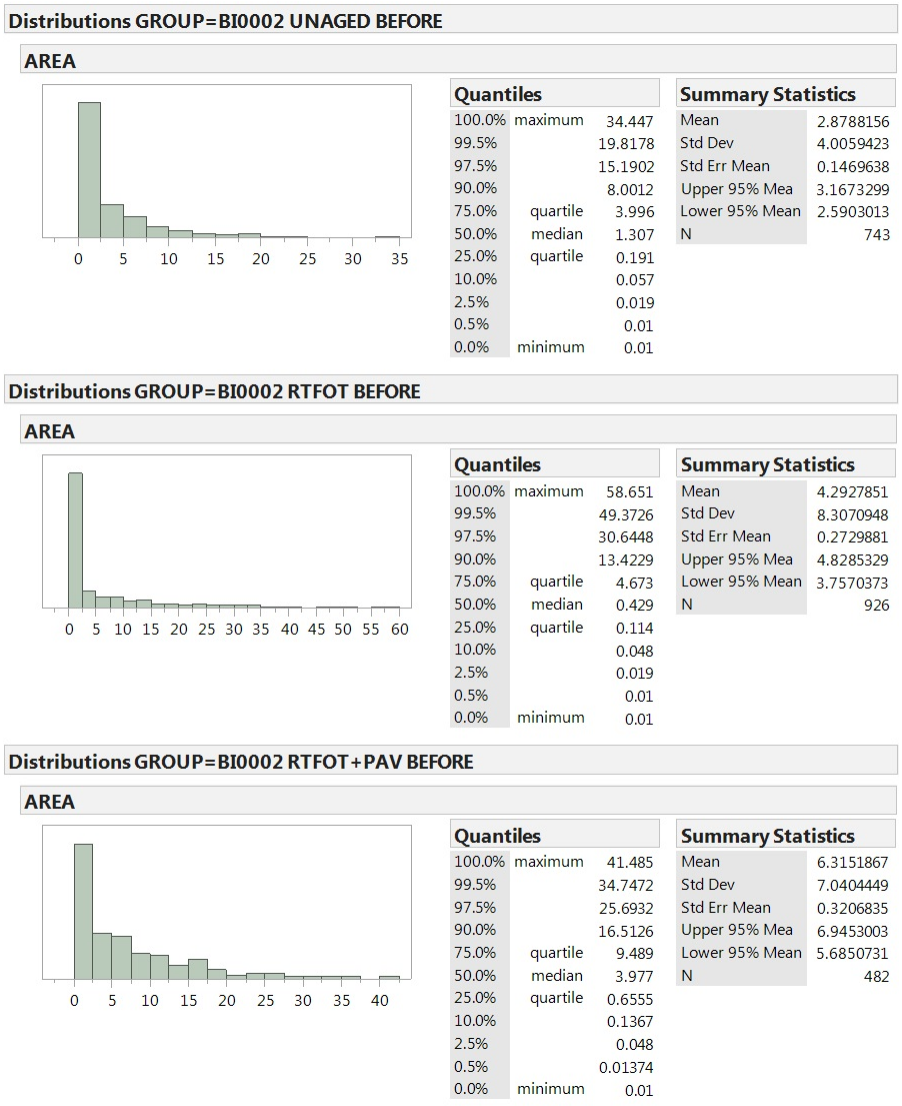

Figure A.8: Distribution of bee structures for asphalt binder BI0002 under different aging conditions

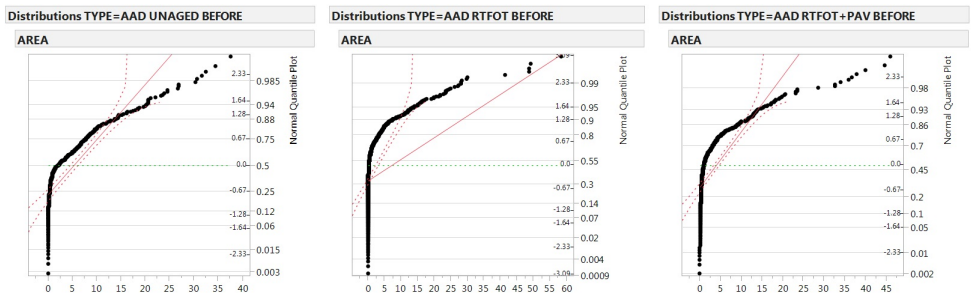

Figure A.9: q-q plots of asphalt binder AAD under different aging conditions

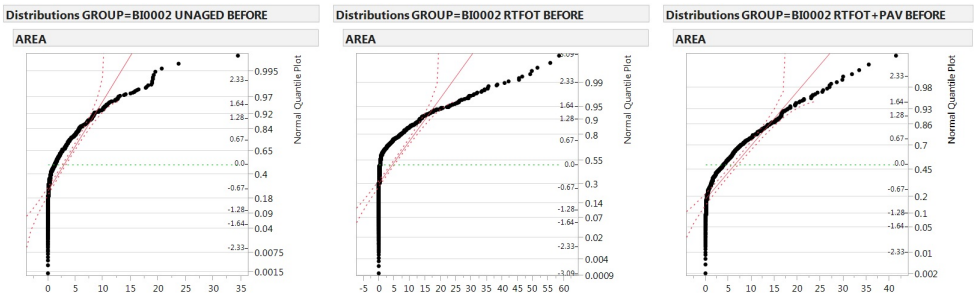

Figure A.10: q-q plots of asphalt binder BI0002 under different aging conditions

straight diagonal line. The data also lies outside of the normality confidence bands for α= 0.05 (95% confidence). Therefore, in order to describe this data an alternative statistical distribution must be assumed. We therefore propose the use of a Gamma distribution to describe this data. The Gamma distribution is particularly useful for describing engineering data that are bound by a certain value. In this case the lower bound for the data is zero since no bee structure can have an area smaller than zero. However, the bee structure area is not bound by a maximum value which also is well described by a Gamma distribution.

Figure A.11 show relative frequency histograms along with the gamma distribution fit parameters for asphalt binder AAD and BI0002. Both plots exhibit a good fit for the Gamma distribution to the sample data. Therefore, this validates the non-normality exhibited by the q-q plots and provides with statistical method for describing the distribution of the data obtained. More detailed information regarding the Gamma distribution can be found in the text by Gentle [15].

A.1.3 Reliability of the Microstructural Analysis

In order to determine the reliability of the microstructural analysis a design of experiment analysis is performed on the mean value of each sample obtained under every aging condition and loading condition. The JMP 11.2 Pro sample size and power calculation can determine the power of the experiment to determine a significant difference in the mean area of the bee

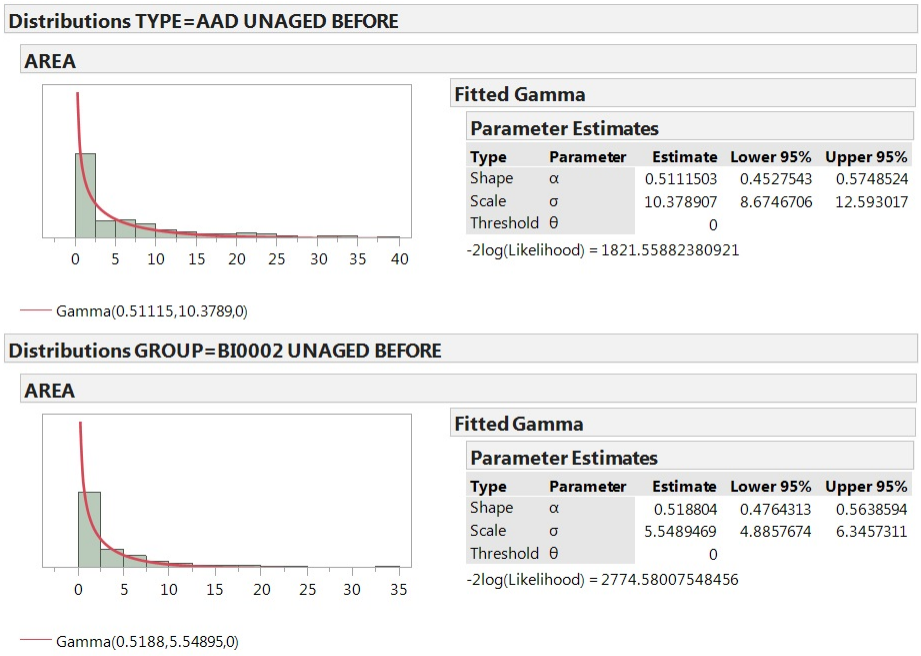

Figure A.11: Gamma distribution fit to relative frequency data of asphalt binder AAD and BI0002

structures.

Table A.1 provides with power values for different sample populations of experiments performed under different aging and loading conditions. The data suggests majority of the experimental trials examining the microstructural distribution has a higher than 80% change of detecting a significance difference in the area of the bee structure, given that the significance level is of 0.05, and a difference to detect is one μm^2. The difference detect based on the smallest value within the order of magnitude of the interquartile range. The interquartile range is of significant interest since majority of the data lies within this range. The sample data for AAD under unaged condition before and after the application of one percent strain showed exhibited a power of 0.78 and 0.71 which was below 0.8. This suggests that higher number of trials are required to detect a significant difference in the area of the bee structures with a power of 0.80 will be part of future recommendations of this work.

Table A.1: Sample Power Calculation

Binder	**AGING CONDITION**	**STRAIN**	**SAMPLE SIZE**	$\bar{x}$	σ	**POWER**
AAD	UNAGED	ZERO	369	5.31	7.04	0.78
		ONE	317	5.13	7.09	0.71
		FIVE	272	3.19	4.22	0.97
AAD	RTFOT AGED	ZERO	923	2.62	5.96	0.99
		ONE	872	2.65	6.79	0.99
		FIVE	729	1.69	3.47	1.00
AAD	RTFOT + PAV AGED	ZERO	501	3.90	6.77	0.91
		ONE	474	3.84	6.50	0.92
		FIVE	282	4.32	5.37	0.88
BI0002	UNAGED	ZERO	743	2.88	4.01	0.99
		ONE	586	2.91	4.43	0.99
		FIVE	490	2.52	3.15	0.99
BI0002	RTFOT AGED	ZERO	926	4.30	8.31	0.96
		ONE	726	4.17	7.36	0.96
		FIVE	640	3.15	4.26	0.99
BI0002	RTFOT + PAV AGED	ZERO	482	6.32	7.04	0.88
		ONE	374	4.70	4.88	0.98
		FIVE	369	4.21	4.39	0.99

A.1.4 Comaparison of Means of Multiple Data Sets Corresponding to Different Loading and Aging Conditions

Wilcoxon / Kruskal-Wallis Tests (Rank Sums)

Level	Count	Score Sum	Expected Score	Score Mean	(Mean-Mean0)/Std0
AAD RTFOT BEFORE	923	1882067	2187510	2039.08	-8.189
AAD RTFOT FIVE PERCENT	729	1482531	1727730	2033.65	-7.216
AAD RTFOT ONE PERCENT	872	1533159	2066640	1758.21	-14.618
AAD RTFOT+PAV BEFORE	501	1380333	1187370	2755.16	6.663
AAD RTFOT+PAV FIVE PERCENT	282	842179	668340	2986.45	7.802
AAD RTFOT+PAV ONE PERCENT	474	1264271	1123380	2667.24	4.986
AAD UNAGED BEFORE	369	1085979	874530	2943.03	8.379
AAD UNAGED FIVE PERCENT STRAIN	272	780720	644640	2870.29	6.212
AAD UNAGED ONE PERCENT STRAIN	317	980194	751290	3092.09	9.728

1-way Test, ChiSquare Approximation

ChiSquare	DF	Prob>ChiSq
581.2068	8	<.0001*

Figure A.12: Wilcoxon/Kruskal-Wallis Rank Sum test for asphalt binder AAD

Wilcoxon / Kruskal-Wallis Tests (Rank Sums)

Level	Count	Score Sum	Expected Score	Score Mean	(Mean-Mean0)/Std0
BI0002 RTFOT BEFORE	926	2054687	2471031	2218.88	-9.770
BI0002 RTFOT FIVE PERCENT	640	1689110	1707840	2639.23	-0.512
BI0002 RTFOT ONE PERCENT	726	2098274	1937331	2890.18	4.172
BI0002 RTFOT+PAV BEFORE	482	1591600	1286217	3302.07	9.467
BI0002 RTFOT+PAV FIVE PERCENT	369	1149863	984677	3116.16	5.786
BI0002 RTFOT+PAV ONE PERCENT	374	1173922	998019	3138.83	6.123
BI0002 UNAGED BEFORE	743	1809595	1982696	2435.52	-4.443
BI0002 UNAGED FIVE PERCENT	490	1269527	1307565	2590.87	-1.170
BI0002 UNAGED ONE PERCENT	586	1402540	1563741	2393.41	-4.582

1-way Test, ChiSquare Approximation

ChiSquare	DF	Prob>ChiSq
278.6249	8	<.0001*

Figure A.13: Wilcoxon/Kruskal-Wallis Rank Sum test for asphalt binder BI0002

The Wilcoxon/Kruskal-Wallis Rank test can be used to test the null hypothesis that the mean areas for asphalt binder BI0002 under different loading and aging conditions are the same. Here the calculated p-value should be interested as given: a p-value ≤ 0.05 indicates a statistically significant different amongst the populations with 95% confidence. The results for the Wilcoxon Rank test is given in figures A.12 and A.13 for asphalt binders AAD and BI0002 respectively. Given that the distribution of data obtained is non-normal shown by

figures A.9 and A.10 a nonparametric comparison for different pairs of data can also be made using the Wilcoxon Method. Here the null hypothesis being test is also that each pair of data exhibits equal mean areas. The results of nonparametric comparisons for each pair using the Wilcoxon Method is given in figure A.14 andA.15 for asphalt binder AAD and BI0002 respectively.

Nonparametric Comparisons For Each Pair Using Wilcoxon Method

q*	Alpha
1.95996	0.05

Level	- Level	Score Mean Difference	Std Err Dif	Z	p-Value	Hodges-Lehmann	Lower CL	Upper CL
AAD UNAGED ONE PERCENT STRAIN	AAD RTFOT ONE PERCENT	311.582	22.51684	13.8377	<.0001*	1.10600	0.848000	1.47800
AAD RTFOT+PAV BEFORE	AAD RTFOT ONE PERCENT	299.197	22.22507	13.4622	<.0001*	0.45700	0.363000	0.57200
AAD UNAGED BEFORE	AAD RTFOT ONE PERCENT	281.355	22.25310	12.6434	<.0001*	0.89700	0.639000	1.33500
AAD RTFOT+PAV FIVE PERCENT	AAD RTFOT ONE PERCENT	277.223	22.82679	12.1446	<.0001*	1.16400	0.811000	1.60300
AAD UNAGED ONE PERCENT STRAIN	AAD RTFOT BEFORE	267.168	23.30960	11.4617	<.0001*	0.96300	0.725000	1.30600
AAD UNAGED FIVE PERCENT STRAIN	AAD RTFOT ONE PERCENT	265.844	22.94125	11.5880	<.0001*	0.70600	0.534000	0.93500
AAD RTFOT+PAV ONE PERCENT	AAD RTFOT ONE PERCENT	264.463	22.17837	11.9244	<.0001*	0.38100	0.296000	0.46800
AAD UNAGED ONE PERCENT STRAIN	AAD RTFOT FIVE PERCENT	246.861	20.32343	12.1466	<.0001*	1.12500	0.829000	1.54500
AAD UNAGED BEFORE	AAD RTFOT BEFORE	235.953	22.97672	10.2692	<.0001*	0.80100	0.524000	1.17300
AAD RTFOT+PAV FIVE PERCENT	AAD RTFOT BEFORE	233.789	23.67509	9.8749	<.0001*	0.96400	0.630000	1.39300
AAD RTFOT+PAV BEFORE	AAD RTFOT BEFORE	218.958	22.81766	9.5960	<.0001*	0.35300	0.257000	0.45800
AAD RTFOT+PAV FIVE PERCENT	AAD RTFOT FIVE PERCENT	214.742	20.47563	10.4877	<.0001*	1.18300	0.811000	1.61200
AAD UNAGED BEFORE	AAD RTFOT FIVE PERCENT	213.887	20.25822	10.5580	<.0001*	0.96300	0.649000	1.51600
AAD UNAGED FIVE PERCENT STRAIN	AAD RTFOT BEFORE	211.423	23.80673	8.8808	<.0001*	0.55300	0.420000	0.76300
AAD RTFOT+PAV BEFORE	AAD RTFOT FIVE PERCENT	201.233	20.61299	9.7624	<.0001*	0.39100	0.286000	0.51500
AAD UNAGED FIVE PERCENT STRAIN	AAD RTFOT FIVE PERCENT	196.143	20.54005	9.5493	<.0001*	0.63900	0.467000	0.87800
AAD RTFOT+PAV ONE PERCENT	AAD RTFOT BEFORE	187.344	22.79438	8.2189	<.0001*	0.28600	0.201000	0.38200
AAD RTFOT+PAV ONE PERCENT	AAD RTFOT FIVE PERCENT	170.521	20.49798	8.3189	<.0001*	0.31400	0.220000	0.42000
AAD UNAGED ONE PERCENT STRAIN	AAD RTFOT+PAV ONE PERCENT	80.188	16.57753	4.8372	<.0001*	0.51500	0.277000	0.79200
AAD UNAGED ONE PERCENT STRAIN	AAD RTFOT+PAV BEFORE	72.384	16.95694	4.2687	<.0001*	0.45800	0.229000	0.74400
AAD UNAGED BEFORE	AAD RTFOT+PAV ONE PERCENT	56.545	16.90387	3.3451	0.0008*	0.31400	0.096000	0.63900
AAD RTFOT+PAV FIVE PERCENT	AAD RTFOT+PAV BEFORE	50.187	16.83758	2.9806	0.0029*	0.34300	0.095000	0.71500
AAD UNAGED BEFORE	AAD RTFOT+PAV BEFORE	46.620	17.23799	2.7045	0.0068*	0.26700	0.057000	0.60000
AAD UNAGED ONE PERCENT STRAIN	AAD UNAGED FIVE PERCENT STRAIN	38.449	14.06375	2.7339	0.0063*	0.38100	0.077000	0.72500
AAD UNAGED FIVE PERCENT STRAIN	AAD RTFOT+PAV ONE PERCENT	36.861	16.39165	2.2488	0.0245*	0.19000	0.019000	0.36300
AAD UNAGED FIVE PERCENT STRAIN	AAD RTFOT+PAV BEFORE	25.356	16.81685	1.5078	0.1316	0.13300	-0.038000	0.31400
AAD UNAGED ONE PERCENT STRAIN	AAD UNAGED BEFORE	12.673	15.17473	0.8352	0.4036	0.11400	-0.152000	0.34400
AAD UNAGED ONE PERCENT STRAIN	AAD RTFOT+PAV FIVE PERCENT	12.105	14.16598	0.8545	0.3928	0.11400	-0.153000	0.42000
AAD RTFOT FIVE PERCENT	AAD RTFOT BEFORE	9.513	23.63370	0.4025	0.6873	0.00900	-0.019000	0.03800
AAD UNAGED BEFORE	AAD RTFOT+PAV FIVE PERCENT	2.574	14.87465	0.1731	0.8626	0.01900	-0.200000	0.28600
AAD RTFOT+PAV ONE PERCENT	AAD RTFOT+PAV BEFORE	-18.028	18.04358	-0.9991	0.3177	-0.05700	-0.162000	0.04800
AAD UNAGED FIVE PERCENT STRAIN	AAD RTFOT+PAV FIVE PERCENT	-25.395	13.60323	-1.8668	0.0619	-0.26700	-0.696000	0.01000
AAD UNAGED FIVE PERCENT STRAIN	AAD UNAGED BEFORE	-25.584	14.79704	-1.7290	0.0838	-0.22900	-0.649000	0.03800
AAD RTFOT+PAV ONE PERCENT	AAD RTFOT+PAV FIVE PERCENT	-57.941	16.42321	-3.5280	0.0004*	-0.39100	-0.772000	-0.14300
AAD RTFOT ONE PERCENT	AAD RTFOT BEFORE	-107.868	24.47155	-4.4079	<.0001*	-0.04700	-0.076000	-0.01900
AAD RTFOT ONE PERCENT	AAD RTFOT FIVE PERCENT	-123.713	23.19661	-5.3332	<.0001*	-0.07600	-0.105000	-0.04700

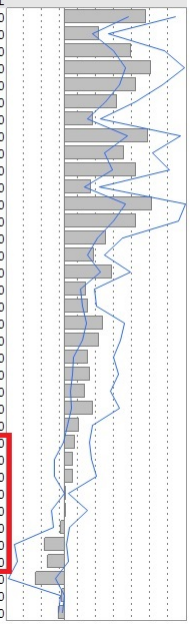

Figure A.14: Nonparametric comparisons for pairs of data using the Wilcoxon Method for asphalt binder AAD

The p value for the Wilcoxon/Kruskal-Wallis Rank Sum tests were calculated for both binder types to be less than 0.0001 which shows that with a significance of 99.99% the mean areas are different for all data populations for both binders. The nonparametric comparison using the Wilcoxon method shows that the null hypothesis of equal means cannot be rejected for all pairs of sample populations. For asphalt binder AAD the null hypothesis could not

Nonparametric Comparisons For Each Pair Using Wilcoxon Method

q*	Alpha
1.95996	0.05

Level	- Level	Score Mean Difference	Std Err Dif	Z	p-Value	Hodges-Lehmann	Lower CL	Upper CL
BI0002 RTFOT+PAV BEFORE	BI0002 RTFOT BEFORE	240.990	22.83593	10.5531	<.0001*	1.52500	1.16400	2.08900
BI0002 RTFOT ONE PERCENT	BI0002 RTFOT BEFORE	208.274	23.64654	8.8078	<.0001*	0.58200	0.42000	0.76300
BI0002 RTFOT+PAV FIVE PERCENT	BI0002 RTFOT BEFORE	202.546	23.02203	8.7979	<.0001*	1.04900	0.68700	1.38300
BI0002 RTFOT+PAV ONE PERCENT	BI0002 RTFOT BEFORE	190.645	22.99999	8.2889	<.0001*	1.14500	0.75300	1.58300
BI0002 RTFOT+PAV BEFORE	BI0002 RTFOT FIVE PERCENT	148.223	19.54226	7.5847	<.0001*	1.47800	1.00200	2.07900
BI0002 RTFOT FIVE PERCENT	BI0002 RTFOT BEFORE	140.998	23.24452	6.0659	<.0001*	0.29600	0.18100	0.45800
BI0002 UNAGED FIVE PERCENT	BI0002 RTFOT BEFORE	136.841	22.84210	5.9907	<.0001*	0.28600	0.18100	0.41000
BI0002 RTFOT+PAV BEFORE	BI0002 RTFOT ONE PERCENT	107.062	20.49723	5.2232	<.0001*	1.01100	0.51500	1.50600
BI0002 RTFOT+PAV ONE PERCENT	BI0002 RTFOT FIVE PERCENT	106.145	19.06114	5.5686	<.0001*	0.91500	0.52500	1.40200
BI0002 RTFOT+PAV FIVE PERCENT	BI0002 RTFOT FIVE PERCENT	100.571	19.04821	5.2798	<.0001*	0.72500	0.41900	1.12500
BI0002 UNAGED BEFORE	BI0002 RTFOT BEFORE	70.238	23.73555	2.9592	0.0031*	0.08600	0.02800	0.17200
BI0002 RTFOT ONE PERCENT	BI0002 RTFOT FIVE PERCENT	69.167	21.38860	3.2338	0.0012*	0.27600	0.09600	0.48600
BI0002 UNAGED ONE PERCENT	BI0002 RTFOT BEFORE	69.093	23.04630	2.9980	0.0027*	0.08600	0.02800	0.18100
BI0002 RTFOT+PAV ONE PERCENT	BI0002 RTFOT ONE PERCENT	61.935	20.22034	3.0630	0.0022*	0.48600	0.14400	0.88600
BI0002 RTFOT+PAV FIVE PERCENT	BI0002 RTFOT ONE PERCENT	50.000	20.21831	2.4730	0.0134*	0.32500	0.05800	0.65800
BI0002 UNAGED FIVE PERCENT	BI0002 UNAGED BEFORE	38.578	20.72185	1.8617	0.0626	0.10500	-0.00900	0.22900
BI0002 RTFOT+PAV ONE PERCENT	BI0002 RTFOT+PAV FIVE PERCENT	12.009	15.74828	0.7625	0.4457	0.13400	-0.19100	0.58200
BI0002 UNAGED ONE PERCENT	BI0002 UNAGED BEFORE	-10.369	21.20327	-0.4890	0.6248	-0.01900	-0.11400	0.05700
BI0002 UNAGED FIVE PERCENT	BI0002 RTFOT FIVE PERCENT	-12.028	19.58962	-0.6140	0.5392	-0.04700	-0.21000	0.09500
BI0002 RTFOT+PAV ONE PERCENT	BI0002 RTFOT+PAV BEFORE	-36.556	17.03772	-2.1456	0.0319*	-0.37200	-0.98300	-0.01900
BI0002 RTFOT+PAV FIVE PERCENT	BI0002 RTFOT+PAV BEFORE	-47.266	17.00278	-2.7799	0.0054*	-0.62900	-1.24900	-0.12400
BI0002 UNAGED ONE PERCENT	BI0002 UNAGED FIVE PERCENT	-51.460	19.02285	-2.7052	0.0068*	-0.16200	-0.29600	-0.03900
BI0002 UNAGED BEFORE	BI0002 RTFOT FIVE PERCENT	-52.697	21.53800	-2.4467	0.0144*	-0.13400	-0.26700	-0.01900
BI0002 UNAGED ONE PERCENT	BI0002 RTFOT FIVE PERCENT	-63.180	20.24300	-3.1211	0.0018*	-0.19100	-0.35300	-0.06600
BI0002 UNAGED FIVE PERCENT	BI0002 RTFOT ONE PERCENT	-80.320	20.53141	-3.9120	<.0001*	-0.38200	-0.62900	-0.17200
BI0002 UNAGED FIVE PERCENT	BI0002 RTFOT+PAV FIVE PERCENT	-104.167	17.10160	-6.0911	<.0001*	-0.94400	-1.34500	-0.57200
BI0002 UNAGED FIVE PERCENT	BI0002 RTFOT+PAV ONE PERCENT	-108.396	17.13536	-6.3259	<.0001*	-1.20200	-1.67800	-0.73400
BI0002 UNAGED BEFORE	BI0002 RTFOT ONE PERCENT	-125.472	22.13707	-5.6680	<.0001*	-0.43800	-0.63900	-0.25700
BI0002 UNAGED ONE PERCENT	BI0002 RTFOT ONE PERCENT	-128.355	21.04037	-6.1004	<.0001*	-0.50500	-0.71500	-0.30600
BI0002 UNAGED ONE PERCENT	BI0002 RTFOT+PAV ONE PERCENT	-134.330	18.35052	-7.3202	<.0001*	-1.20200	-1.65000	-0.76300
BI0002 UNAGED ONE PERCENT	BI0002 RTFOT+PAV FIVE PERCENT	-134.969	18.33047	-7.3631	<.0001*	-1.01100	-1.39200	-0.65800
BI0002 UNAGED BEFORE	BI0002 RTFOT+PAV FIVE PERCENT	-144.362	20.45245	-7.0584	<.0001*	-0.88700	-1.26900	-0.57200
BI0002 UNAGED FIVE PERCENT	BI0002 RTFOT+PAV BEFORE	-145.098	18.00974	-8.0567	<.0001*	-1.80300	-2.47000	-1.24900
BI0002 UNAGED BEFORE	BI0002 RTFOT+PAV ONE PERCENT	-147.028	20.45230	-7.1888	<.0001*	-1.10600	-1.56400	-0.70600
BI0002 UNAGED ONE PERCENT	BI0002 RTFOT+PAV BEFORE	-176.543	18.96667	-9.3081	<.0001*	-1.72600	-2.35500	-1.24000
BI0002 UNAGED BEFORE	BI0002 RTFOT+PAV BEFORE	-197.357	20.69019	-9.5387	<.0001*	-1.64900	-2.23200	-1.21100

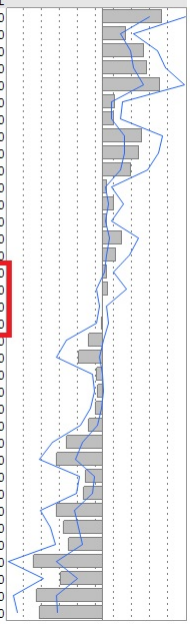

Figure A.15: Nonparametric comparisons for pairs of data using the Wilcoxon Method for asphalt binder BI0002

be rejected in particular for comparisons between unaged before and after one percent, and after five percent applied strain. The null hypothesis of equal means also was not rejected for comparisons between before and after the application of five percent strain for RTFOT aged samples, and also between RTFOT+PAV aged samples before and after the application of one percent strain. This analysis suggests for multiple aging conditions the application of strain did not lead to significant enough change in the mean area for the null hypothesis of equal means to be rejected. This phenomenon is possible and can be explained due to the redistribution of the mean areas of the bee structures. The application of tensile strains will lead to the dissipation of some bee structures. However, simultaneously the flattening and possibly reduction in the areas of the larger bee structures will also occur which can lead to an overall minor change in the mean area of the bee structures.

A.2 Stastistical Analysis of Creep Indentation Measurements of Asphalt Binder

In Section 3 and Section 4 creep indentation experiments were utilized to obtain elastic and viscoelastic properties of different phases identified within asphalt binder samples AAD (binder B), and BI0002 (binder A). For each phase seven separate indentation tests were performed and the average measurements of all seven data sets were reported in Section 3 and Section 4 and the data was used to obtain creep compliance properties of the different phases. In this section the statistical distribution of the measurements are examined in more detail. The authors would like to note that due to experimental limitations (AFM tip wear, sample degradation) a high number of sample size was difficult to obtain. Due to this low sample size any meaningful information regarding the total population of the creep properties is difficult to obtain. However, by comparing the coefficient of variation between the different data sets for each phase under different aging condition meaningful comparisons can still be made. Table A.2, and A.3 provides with statistical information regarding instantaneous depth of indentation, and final depth of indentation measurements (H_0) obtained through creep indentation experiments for each phase and under different aging conditions.

The minimum coefficient of variation obtained for the initial depth of indentation was for binder BI0002 (binder A) bee phase under RTFOT aged condition. The maximum coefficient of variation for the initial depth of indentation was obtained for binder B interstitial phase under PAV aged condition. The minimum coefficient of variation for the final depth of indentation was obtained for binder BI0002 (binder A) casing phase under RTFOT aging condition. The maximum coefficient of variation for the final depth of indentation was obtained for binder BI0002 (binder A) interstitial phase under unaged condition. In comparison the coefficient of variation for the final depth of indentation data was generally higher than the initial depth of indentation. This suggests that the creep indentation data for the final depth of indentation exhibited a higher variation than the creep indentation data for the initial depth of indentation. This reflects upon the necessity of performing a higher number of trials

Table A.2: Statistical analysis of initial depth of indentation

BINDER	SAMPLE	MEAN	STDEV	COEFFICIENT OF VAR (%)
A UNAGED	BEE	0.034	0.005	15.990
	CASING	0.027	0.006	23.136
	INTERSTITIAL	0.021	0.002	10.411
A RTFOT	BEE	0.024	0.002	6.293
	CASING	0.025	0.003	12.835
	INTERSTITIAL	0.026	0.003	10.358
A PAV	BEE	0.020	0.002	9.268
	CASING	0.018	0.002	9.792
	INTERSTITIAL	0.019	0.002	10.913
B UNAGED	BEE	0.042	0.010	23.549
	CASING	0.035	0.009	24.952
	INTERSTITIAL	0.027	0.002	9.185
B RTFOT	BEE	0.036	0.007	18.297
	CASING	0.030	0.006	19.390
	INTERSTITIAL	0.025	0.003	12.970
B PAV	BEE	0.033	0.006	18.052
	CASING	0.033	0.004	12.017
	INTERSTITIAL	0.030	0.008	25.973

to possibly obtain a lower coefficient of variation for the final depth of indentation values. In addition, a higher number of trials will also lead to a better estimation of the true population and also increase the statistical power of the experiment. Suggestions regarding experimental improvements to obtain a higher number of trials along with reducing experimental error are mentioned in the recommendations for future work sections.

Table A.3: Statistical analysis of final depth of indentation

BINDER	SAMPLE	MEAN	STDEV	COEFFICIENT OF VAR (%)
A UNAGED	BEE	0.267	0.057	21.254
	CASING	0.189	0.071	37.452
	INTERSTITIAL	0.134	0.055	40.568
A RTFOT	BEE	0.170	0.030	17.729
	CASING	0.188	0.018	9.592
	INTERSTITIAL	0.163	0.037	22.645
A PAV	BEE	0.053	0.018	33.413
	CASING	0.044	0.013	30.263
	INTERSTITIAL	0.052	0.014	26.029
B UNAGED	BEE	0.709	0.249	35.092
	CASING	0.324	0.127	39.182
	INTERSTITIAL	0.304	0.064	21.104
B RTFOT	BEE	0.280	0.084	30.117
	CASING	0.214	0.066	30.642
	INTERSTITIAL	0.165	0.035	20.951
B PAV	BEE	0.263	0.068	25.751
	CASING	0.243	0.056	23.211
	INTERSTITIAL	0.209	0.083	40.016